Article

Immunity

Tumor-associated macrophages enhance peripheral nerve tumor infiltration and spinal cord repair

Graphical abstract

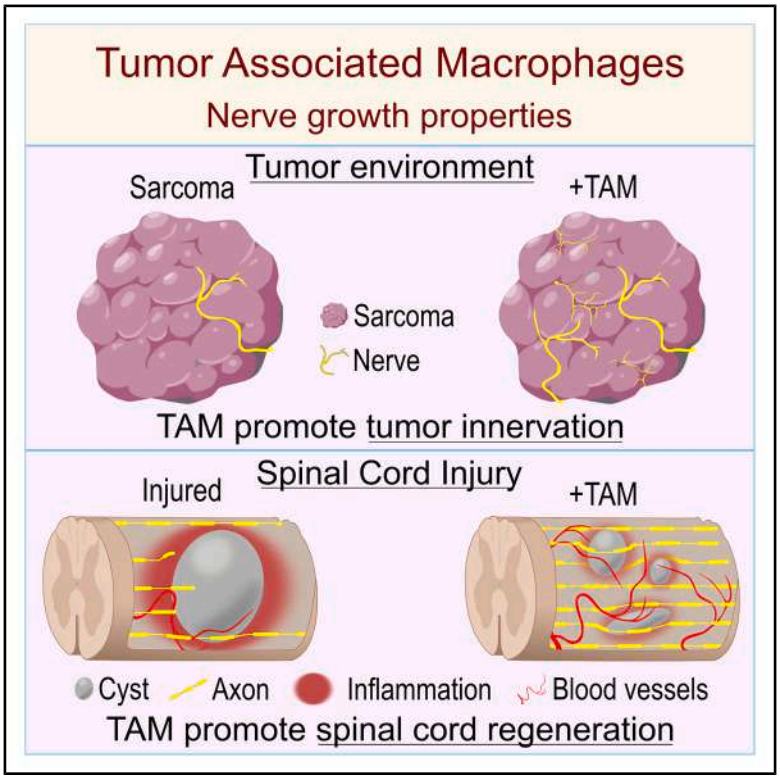

Highlights

- Human and mouse TAMs exhibit a unique functional neural growth gene signature
- TAMs enhance tumor innervation
- TAMs promote neural tissue regeneration and motor recovery after severe scSCI
- SPP1 is required for TAM-induced neuronal growth

Authors

Sissi Dolci, Loris Mannino, Eros Rossi, ..., Massimo Locati, Francesco Bifari, Ilaria Decimo

Correspondence

guido.fumagalli@univr.it (G.F.F.), massimo.locati@unimi.it (M.L.), francesco.bifari@unimi.it (F.B.), ilaria.decimo@univr.it (I.D.)

In brief

Tumor-associated macrophages (TAMs) enhance cancer progression by driving angiogenesis, extracellular matrix remodeling, and immune suppression, yet their impact on nerve growth is unclear. Dolci and colleagues show that TAMs directly stimulate neurite outgrowth, revealing a dual role in enhancing intratumoral nerve growth and promoting neural repair after severe spinal cord injury.

Dolci et al., 2026, Immunity *59*, 438–457
February 10, 2026
https://doi.org/10.1016/j.immuni.2025.12.016

CellPress

CellPress
OPEN ACCESS

Immunity

Article

Tumor-associated macrophages enhance peripheral nerve tumor infiltration and spinal cord repair

Sissi Dolci,[1] Loris Mannino,[1] Eros Rossi,[1] Emanuela Bottani,[1] Francesca Ciarpella,[1] Nicola Piazza,[1] Isabel Karkossa,[2] Marzia Di Chio,[1] Benedetta Savino,[3,4] Benedetta Lucidi,[1] Giulia Pruonto,[3] Ilaria Barone,[3] Alessandra Campanelli,[1] Francesca Cersosimo,[4] Elisa Setten,[3] Stefano Gianoli,[3] Zulkifal Malik,[3] Giuseppe Busetto,[5] Alex Pezzotta,[3] Alessandra Castagna,[4] Nicolò Martinelli,[1] Silvia Ferretti,[1] Federico Boschi,[6] Adam Doherty,[7,8] Maria Teresa Scupoli,[6,9] Chiara Cavallini,[9] Giorgio Malpeli,[10,15] Alessia Amenta,[3] Ludovica Sagripanti,[3] Vincenzo Silani,[11,12] Patrizia Cristofori,[1] Eugenio Scanziani,[13] Marco Sandri,[1] Anna Pistocchi,[3] Patrizia Bossolasco,[11] Marco Endrizzi,[7,8] Kristin Schubert,[2] Guido Francesco Fumagalli,[1,*] Massimo Locati,[3,4,*] Francesco Bifari,[3,14,*] and Ilaria Decimo[1,14,16,*]

[1]Department of Diagnostic and Public Health, University of Verona, Verona, Italy
[2]Department of Molecular Toxicology, Helmholtz-Centre for Environmental Research - UFZ, Leipzig, Germany
[3]Department of Medical Biotechnology and Translational Medicine, University of Milan, Milan, Italy
[4]IRCCS Humanitas Research Hospital, Rozzano, Milan, Italy
[5]Department of Neuroscience, Biomedicine and Movement Science, University of Verona, Verona, Italy
[6]Department of Engineering for Innovation Medicine, University of Verona, Verona, Italy
[7]Department of Medical Physics and Biomedical Engineering, University College London, London, UK
[8]X-ray Microscopy and Tomography Lab, The Francis Crick Institute, London, UK
[9]LURM, University of Verona, Verona, Italy
[10]Department of Surgery, Dentistry, Pediatric and Gynecology, University of Verona, Verona, Italy
[11]Department of Neurology, IRCCS Istituto Auxologico Italiano, Milan, Italy
[12]Department of Pathophysiology and Transplantation, University of Milan, Milan, Italy
[13]Department of Veterinary Medicine and Animal Sciences, University of Milan, Milan, Italy
[14]These authors contributed equally
[15]Present address: Department of Life Sciences, Health and Health Professions, Link Campus University, Rome, Italy
[16]Lead contact
*Correspondence: guido.fumagalli@univr.it (G.F.F.), massimo.locati@unimi.it (M.L.), francesco.bifari@unimi.it (F.B.), ilaria.decimo@univr.it (I.D.)
https://doi.org/10.1016/j.immuni.2025.12.016

SUMMARY

Tumor-associated macrophages (TAMs) enhance cancer progression by promoting angiogenesis, extracellular matrix remodeling, and immune suppression. Nerve infiltration also contributes to tumor growth. However, the role of TAMs in promoting intratumoral nerve growth remains unclear. In this study, we have shown that TAMs express a distinct neural growth gene signature. TAMs actively enhanced neural growth within tumors and directly promoted *in vitro* neurite outgrowth. We identified secreted phosphoprotein 1 (SPP1) as a required mediator of TAM-driven neural growth and mTORC2 activation. Leveraging this TAM-neural growth function, we explored TAM neuroregenerative potential. Adoptive transfer of TAMs in severe complete-compressive-contusive spinal cord injury (scSCI) increased neuronal survival, axonal regrowth, and motor function recovery. Moreover, TAMs healed scSCI microenvironment and remodeled the cyst. Functional and proteomic analyses confirmed SPP1 and neural Rictor as necessary molecular mediators for TAM-induced regeneration. Our data unveil a role for TAMs in tumor innervation and neural tissue repair.

INTRODUCTION

Intratumoral nerve infiltration supports cancer growth in several tumors. Notably, many tumors promote nerve growth and infiltration, generating a positive feedback loop between the cancer-dependent nerve growth and tumor progression.[1] Several mediators produced by cancer cells have been proposed to regulate nerve-cancer interaction.[2] However, the contribution of different cells composing the tumor microenvironment to cancer-dependent nerve growth has been poorly investigated. Tumor-associated macrophages (TAMs) play a crucial role in tumor growth stimulation, supporting angiogenesis, extracellular matrix (ECM) remodeling, cell proliferation, and immunosuppression.[3] Macrophages and other cells of the tumor microenvironment, including Schwann cells, have been shown to migrate through nerves, functioning as chemoattractants for cancer cells.[4] Nonetheless, the specific role of TAMs in directly stimulating nerve growth remains unclear. Beyond their roles in organogenesis, tissue regeneration, and wound healing,[5] macrophages also contribute to peripheral nerve maintenance and

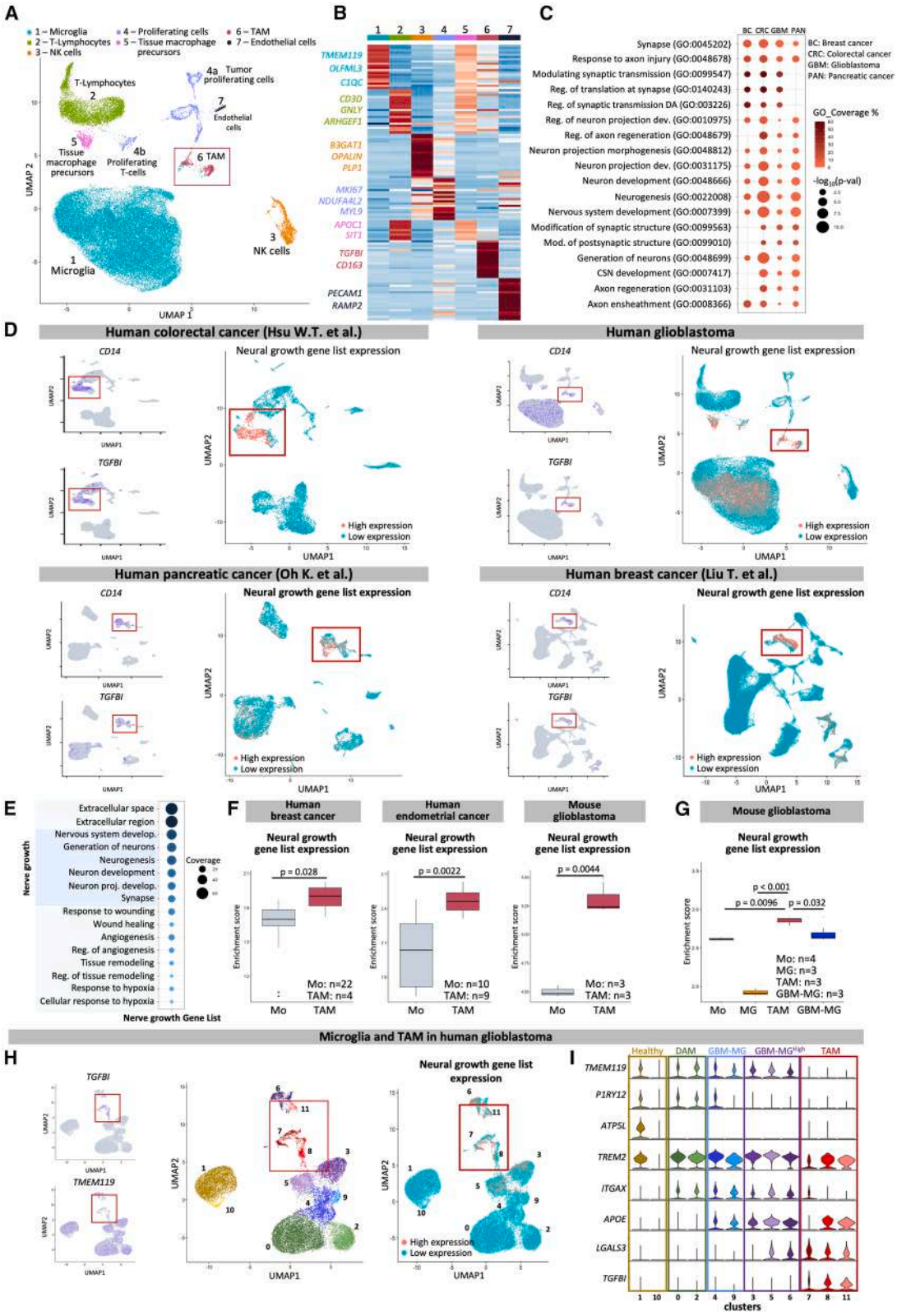

Figure 1. TAMs show the neural growth gene signature

(A) Uniform approximation and projection (UMAP) plot of human GBM, astrocytoma, and healthy tissue scRNA-seq data.

(B) Heatmap of the gene identifying the clusters in (A).

(legend continued on next page)

regeneration.[6,7] Resident enteric microglia-like nerve-associated macrophages play a role in developmental synaptic pruning and maintenance of mature neuronal circuitry.[8,9] Recruitment of macrophages into the peripheral nerves of obese prediabetic mice has been shown to be neuroprotective, delaying terminal sensory axon degeneration.[10] In contrast, macrophage-mediated healing and regenerative functions have been reported to be defective in the injured adult central nervous system (CNS) regeneration, characterized by a maladaptive wound repair process supported by tissue hypoxia, chronic inflammation, and fibrotic cysts formation, leading to neural tissue loss and axonal degeneration.[11–14] In this work, we investigated the neural growth properties of TAMs and their relevance in mediating intratumoral innervation and promoting neural repair after spinal cord injury (SCI).

RESULTS

TAMs express a neural growth gene signature

To assess whether TAMs are endowed with properties related to neural growth potential, we first investigated the gene signature of TAMs infiltrating human tumors in our single-cell RNA sequencing (scRNA-seq) data (Zenodo: https://zenodo.org/record/6046299#.YgZ6bpbSKN4) obtained from human glioblastoma (GBM), astrocytoma, and adjacent healthy tissue (Figures 1A and 1B; Figures S1A and S1B). We further extended the analysis of the TAM signature to publicly available scRNA-seq datasets of human pancreatic,[15] breast,[16] and colorectal cancers[17] (Figures 1C and 1D; Figure S1C). Following TAM cluster identification (CD45$^+$, CD14$^+$, CD163$^+$, *TGFBI*$^+$; Figure 1D), we first extracted the differentially expressed genes (DEGs) of the TAM cluster compared with all other non-myeloid CD14$^-$ cell clusters,[18,19] including tumor, stromal, and infiltrating immune cells. As expected, Gene Ontology (GO) analysis on the identified DEGs showed that TAM clusters upregulated GOs related to response to hypoxia, angiogenesis, ECM remodeling, and wound healing (Figure S1C).[3,20] Of note, in addition to these expected TAM-related GOs, we consistently found in TAM clusters all scRNA-seq datasets of human GBM, pancreatic, breast, and colorectal cancer, with the upregulation of GOs related to neural development, synapse formation, response to axon injury, and neuron-axon regeneration (Figure 1C).[21] We first extracted 152 DEGs upregulated in the 27 neural-related GOs expressed by the TAM cluster in the human GBM dataset (Figure S1D). We refined this initial list by including only genes related to the cell secretome and itemized in the Secreted Protein Database (SEPDB),[22] with well-established roles in neural growth-related functions, and identified a TAM-specific 23-gene neural growth signature (Table S1).[10,23–31] GO coverage analysis confirmed that the neural growth gene list was primarily associated with nerve growth, and its enrichment was consistently observed in TAM clusters across multiple human cancer scRNA-seq datasets (Figures 1D and 1E).

Consistently, TAMs were significantly enriched in the neural growth list compared with circulating monocytes (Mo) in bulk RNA-seq datasets from human breast and endometrial cancer, and mouse GBM (Figures 1F and 1G).[32–34] Collectively, these findings confirm that the neural growth gene signature was a consistent feature of TAMs across various human and murine tumors (Figures 1D, 1F, and 1G).

We next performed a subset analysis on TAM and microglia clusters, the latter representing another major GBM myeloid population with reported neurogenic properties[8,9,27,35–37] within our GBM scRNA-seq dataset (Figures 1H and 1I). We identified 3 different microglia populations: (1) sub-clusters 1 and 10 were entirely composed of cells derived from healthy brain tissue (Figure S1E), both expressing homeostatic microglia markers (Figure 1I), (2) sub-clusters 0 and 2 were disease-associated microglia (DAM) expressing *Itgax*[38] (Figure 1I), and (3) sub-clusters 3–6 and 9 were GBM-associated microglia (GBM-MG)[36] expressing *APOE* (Figure 1I). TAM clusters (sub-clusters 7, 8, and 11) expressed the *Trem2*, *Apoe* genes, and the neurogenic gene *Lgals3*[10] (Figure 1I). The neural growth gene list was strongly upregulated in TAMs (Figure 1H) and in a subset of GBM-MG (GBM-MG^{high}, Figure 1H) with selective enrichment of GOs related to synapses, neuron projection, and wound healing (Figure S1F). We further confirmed the TAM-specific overexpression of the neural growth signature in a publicly available bulk RNA-seq database of mouse GBM.[32] Consistently, in this dataset, the expression of the neural growth signature was higher in TAMs compared with Mo, healthy microglia, and GBM-MG (Figure 1G).[32]

Overall, we find that within the tumor, macrophages acquire a neural growth signature, which is consistently expressed by TAMs extracted from 8 different tumor datasets, both from human and mouse samples.

TAMs enhance tumor innervation through SPP1

To functionally assess TAM's neural growth potential, we studied TAM's impact on tumor innervation using an *in vivo* model of a sarcoma tumor.[39–41] Notably, scRNA-seq analysis of a mouse sarcoma dataset[41] confirmed the presence of a TAM cluster exhibiting upregulation of the neural growth gene signature (Figure 2A). We therefore performed adoptive transfer experiments to enhance the TAM population within the tumor microenvironment and assessed their functional impact

(C) Bubble plot of gene ontologies representing TAM-neural growth signature in GBM, breast, colorectal, and pancreatic human scRNA-seq datasets.
(D) Neural growth gene list expression in TAM clusters of human colorectal, GBM, pancreatic, and breast cancer scRNA-seq datasets.
(E) Bubble plot showing the coverage of the "neural growth" genes to the GOs related to TAM properties.
(F) Expression of the neural growth gene list in TAM and Mo from human breast and endometrial cancer and from mouse GBM.
(G) Neural growth gene list expression in TAM, Mo, healthy microglia, and DAM from mouse GBM.
(H) TAM (7, 8, 11) TGFBI$^+$/TMEM119$^-$ sub-clusters of human GBM enrich the expression of the neural growth gene list compared with TGFBI$^-$/TMEM119$^+$ microglia.
(I) Violin plot of marker genes defining microglial and macrophage subpopulations within GBM, including healthy microglia, DAM, GBM-MG, GBM-MG^{high}, and TAM.
Data are presented as mean ± SEM. Dots represent biological replicates.
See also Figure S1 and Table S1.

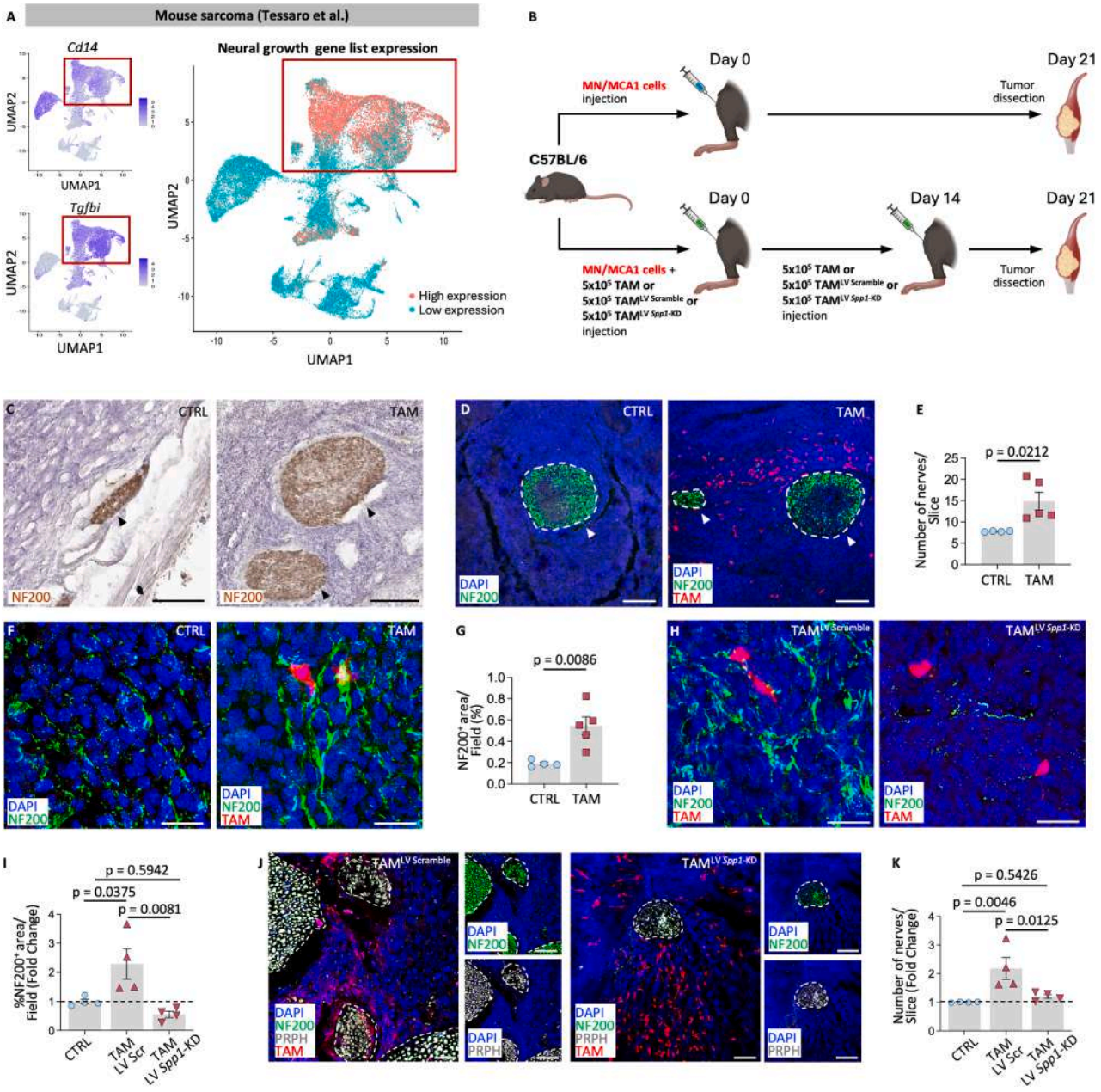

Figure 2. TAMs promote tumor innervation in mouse sarcoma through SPP1

(A) Neural growth gene list expression (pink cells indicate higher expression) is increased in the CD14$^+$/TGFBI$^+$ TAM cluster in the mouse sarcoma scRNA-seq dataset (red square).

(B) Scheme of the experimental workflow.

(C) NF200 immunohistochemistry in control (CTRL) and TAM sarcoma sections. Arrows indicate nerves. Scale bar, 150 μm.

(D and E) Images and quantification of NF200$^+$ nerves from CTRL and TAM sarcoma sections. Arrows indicate nerves. Scale bar, 200 μm.

(F and G) Images and quantification of NF200$^+$ axons from CTRL and TAM sarcoma sections. Scale bar, 20 μm.

(H and I) Images and quantification of NF200$^+$ axons from TAM$^{LV\ Scramble}$- and TAM$^{LV\ Spp1\text{-}KD}$ sarcoma sections. Scale bar, 20 μm.

(J and K) Images and quantification of NF200$^+$ and PRPH$^+$ nerves from TAM$^{LV\ Scramble}$ and TAM$^{LV\ Spp1\text{-}KD}$ sarcoma sections. Scale bar, 200 μm.

Data are presented as mean ± SEM. Dots represent biological replicates.

See also Figure S2.

on tumor innervation. TAMs were generated *in vitro* by exposing macrophages to a sarcoma-conditioned microenvironment (see STAR Methods), thereby inducing a phenotype that closely mimicked that of *in vivo* TAMs. *In vitro*-generated mouse TAMs acquired specific markers and properties distinct from M2-like macrophages (Figures S1G–S1R), expressed the *in vivo* defined TAM gene signature[19] (Figure S1G), and exhibited key TAM functional features, including metabolic

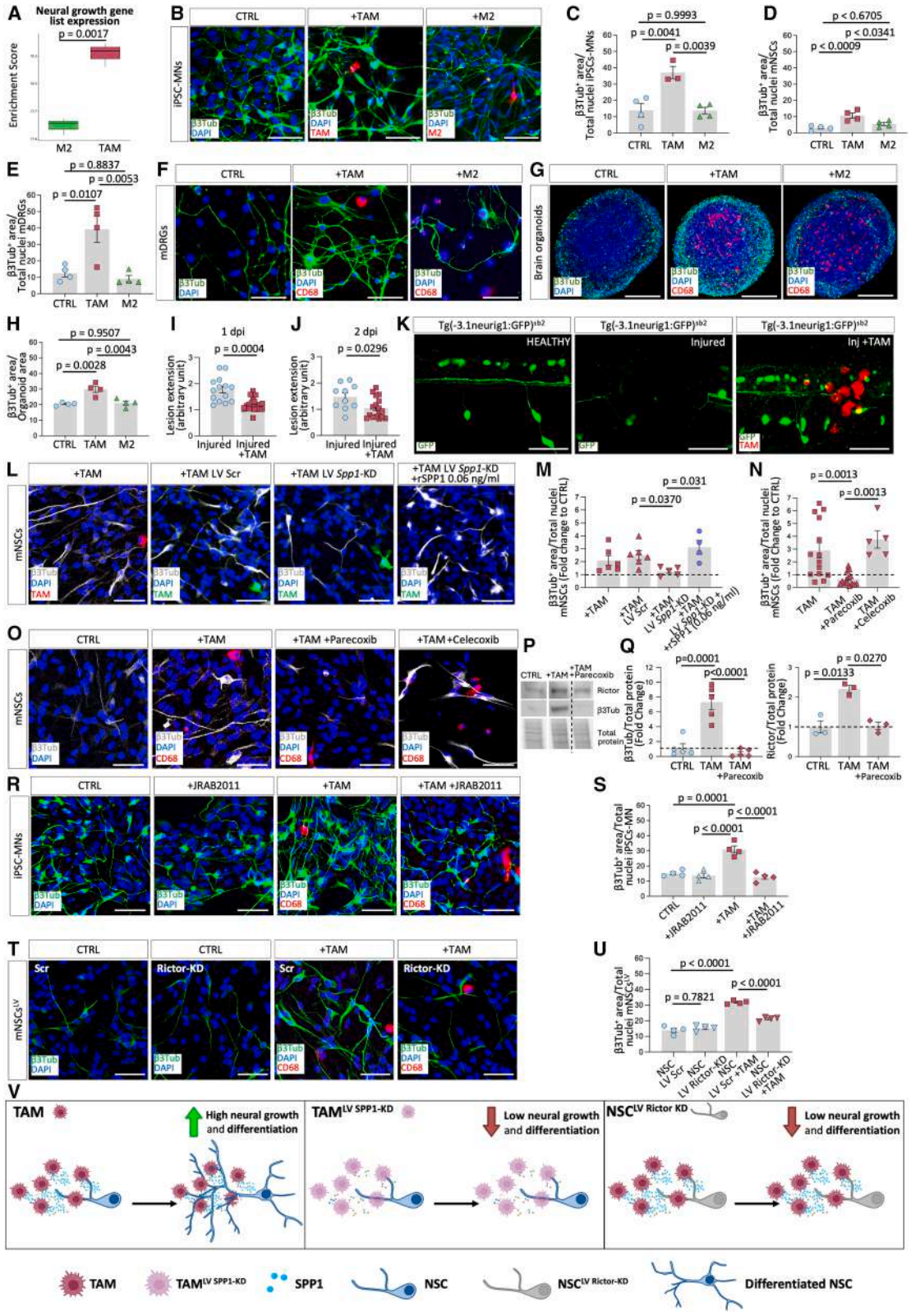

Figure 3. TAMs directly enhance neuronal growth and axonal regeneration via SPP1

(A) RNA bulk expression of neural growth gene list in *in vitro*-generated mouse M2-like macrophages (M2) and TAMs (TAM).

(B and C) Images and quantification of β3Tub expression in human iPSC-MNs alone (CTRL) or co-cultured with $TAM^{tdTomato}$, or $M2^{tdTomato}$. Scale bar, 50 μm.

(legend continued on next page)

plasticity, angiogenesis, ECM remodeling, and immunomodulation (Figures S1H–S1Z).

To induce sarcoma, we transplanted MN-MCA1 cells into the skeletal muscles of recipient mice,[42] either alone or coinjected with 5×10^5 TAMs obtained from tdTomato-expressing mice ($TAM^{tdTomato}$), on days 0 and 14 (Figure 2B). $TAM^{tdTomato}$ transplanted into the sarcoma were continuously exposed *in vivo* to tumor-derived stimuli, enabling their integration into the tumor microenvironment and sustaining their pro-tumoral functionality. 3 weeks after the tumor graft (day 21), the increased TAM population within the sarcoma did not change primary tumor weight and volume (Figure S2A). However, adoptive transfer of TAMs led to enhanced lung metastases and tumor progression (Figures S2B–S2D). $TAM^{tdTomato}$ transplantation determined a 2-fold increase in nerve number (Figures 2C–2E) and $NF200^+$ axons (Figures 2F and 2G), suggesting a role for TAMs in promoting tumor innervation and progression. Consistent with the common pattern shared by nerve and blood vessel wiring,[43] we observed $NF200^+$ axons lining $CD31^+$ vessels (Figure S2E).

Bioinformatic analysis of human and mouse TAM RNA-seq datasets highlighted secreted phosphoprotein-1 (*SPP1*), a known neurotrophic factor,[24,26,27] as one of the most consistently upregulated genes (Figures S2F and S2G). We confirmed the expression and high concentration of secreted SPP1 by *in vitro*-generated TAMs (Figures S2H and S2I). To assess whether SPP1 was a required factor for TAM-induced intratumoral nerve growth effect, we transplanted short hairpin RNA (shRNA)-silenced *Spp1* TAMs ($TAM^{LV\ Spp1\text{-}KD}$) in the sarcoma model. $TAM^{LV\ Spp1\text{-}KD}$ resulted in a marked inhibition of *Spp1* expression in transduced cells (Figures S2J and S2K) and a consistent reduction in secreted SPP1 (Figures S2L and S2M), without affecting their survival (Figures S2N and S2O). $TAM^{LV\ Spp1\text{-}KD}$ or scramble transduced TAMs ($TAM^{LV\ Scramble}$) were administered on days 0 and 14 after tumor cell grafting (Figure 2B). Despite a comparable number of $TAM^{LV\ Scramble}$ and $TAM^{LV\ Spp1\text{-}KD}$ in the tumor mass (Figure S2P), we found that $TAM^{LV\ Scramble}$ increased $NF200^+$ axons and $Peripherin^+$ nerve fibers within the tumor (Figures 2H–2K; Figure S2Q), whereas $TAM^{LV\ Spp1\text{-}KD}$ failed to promote axonal and nerve fiber growth (Figures 2H–2K; Figure S2Q), suggesting the role of SPP1 in TAM tumor innervation effect.

Collectively, these data show that TAMs enhance tumor progression and peripheral nerve infiltration and identify SPP1 as one required TAM-neural growth effector.

TAMs play a direct role in neurite outgrowth and axonal regrowth

Our results displayed above show that TAMs express a neural growth signature and hence enhance neural growth in tumors. We further confirmed the upregulation of the neural growth gene signature in TAMs compared with M2-like macrophages (Figure 3A), suggesting a specific role for TAMs in promoting neuronal outgrowth.

To assess whether TAMs have a direct role in neuronal outgrowth, we tested the capability of *in vitro*-generated mouse TAMs and M2-like macrophages (Figures S1G–S1R) to promote neural sprouting in different neuronal cell types, including human motor neurons (MNs) derived from human induced pluripotent stem cells (iPSC-MNs),[44] mouse neurons derived from neural stem cells (mNSCs),[45] and dorsal root ganglia (mDRGs), and a well-standardized 3D brain organoid model[46,47] (Figures 3B–3H; Figure S3A). In line with the data observed *in vivo* in the tumor model, after co-culturing with $TAM^{tdTomato}$, all these different neuronal cultures approximately doubled their neurite outgrowth assessed by the expression of the neurite-specific marker β3-tubulin (β3Tub) (Figures 3B–3F; Figure S3A), and increased their neurite length (Figure S3B), while maintaining a comparable number of neuronal cells (Figure S3C). This effect was not observed when these different neuronal types were co-cultured with M2-like macrophages obtained from tdTomato-expressing mice ($M2^{tdTomato}$) (Figures 3B–3F; Figure S3A). Similarly, brain organoids co-cultured with TAMs exhibited increased expression of β3Tub (Figures 3G and 3H) and, despite a comparable number of active cells (Figures S3D and S3E), showed a higher frequency of Ca^{2+} spontaneous oscillations compared with both M2-like macrophages co-cultured and control organoids (Figures S3F and S3G). These *in vitro* findings indicate that TAMs specifically support neuronal outgrowth, a property not observed in M2-like macrophages.

To test whether TAMs may promote axonal regrowth, we transplanted $TAM^{tdTomato}$ into a zebrafish model of axonal regeneration. We injected $TAM^{tdTomato}$ in Tg(-3.1*neurog1*:GFP)^{sb2} zebrafish[48] embryos expressing the reporter protein GFP in neuronal cells, allowing spinal axonal fiber visualization (Figures 3I–3K). Following damage to the spinal neural tissue, we quantified GFP expression at the lesion site. At both 1 and 2 days post injury (dpi), $TAM^{tdTomato}$ transplantation significantly reduced the extension of the neural damaged area compared with vehicle (dPBS)

(D) Quantification of β3Tub expression in mNSCs CTRL or co-cultured with TAM or M2.
(E and F) Images and quantification of β3Tub expression in DRGs (CTRL) or co-cultured with TAM, or M2. Scale bar, 50 μm.(G and H) Images and quantification of β3Tub expression in brain organoids at 14 days *in vitro* (DIV) (CTRL) or co-cultured with TAM, or M2. Scale bar, 200 μm.
(I and J) Lesion extension in injured (CTRL) and TAM-treated Tg(-3.1*neurog1*:GFP)^{sb2} zebrafish embryos at 1 (I) and 2 dpi (J).
(K) GFP expression in healthy, injured (CTRL) and TAM-treated Tg(-3.1*neurog1*:GFP)^{sb2} zebrafish embryos. Scale bar, 100 μm.
(L and M) Images and quantification of β3Tub expression in mNSCs co-cultured with TAM, $TAM^{LV\ Scramble}$, $TAM^{LV\ Spp1\text{-}KD}$, or $TAM^{LV\ Spp1\text{-}KD}$+rSPP1. Scale bar, 50 μm.
(N and O) Quantification and images of β3Tub expression in mNSCs co-cultured with TAM, TAM + parecoxib, and TAM + celecoxib. Scale bar, 50 μm.
(P and Q) Immunoblot and quantification of β3Tub and Rictor expression in mNSCs alone (CTRL), co-cultured with TAM, or TAM + parecoxib. Blots were cropped to remove irrelevant lanes for clarity.
(R and S) Images and quantification of β3Tub expression in iPSC-MNs alone (CTRL), +JRAB2011, co-cultured with TAM, or TAM + JRAB2011. Scale bar, 50 μm.
(T and U) Images and quantification of β3Tub expression in $mNSC^{LV\ Scramble}$ and $mNSC^{LV\ Rictor\text{-}KD}$ alone (CTRL), or co-cultured with TAM. Scale bar, 50 μm.
(V) Graphical abstract of TAM-neuron interaction.
Data are presented as mean ± SEM. Dots represent biological replicates.
See also Figure S3.

treated zebrafish, suggesting a role of TAMs in promoting axonal regeneration (Figures 3I–3K).

These data indicate that TAMs have a direct role in neuronal outgrowth and axonal regeneration, both *in vitro* and *in vivo*.

We then assessed whether SPP1 was a required mediator of TAM's direct effect on neural outgrowth *in vitro*. Contrary to $TAM^{LV\ Scramble}$, $TAM^{LV\ Spp1\text{-}KD}$ failed to increase β3Tub expression in neurons derived from mNSCs (Figures 3L and 3M). Accordingly, pharmacological inhibition of *Spp1* by parecoxib, an inverse agonist of the NR4A2 transcription factor[49] required for *Spp1* expression,[50] significantly reduced TAM *Spp1* expression (Figure S3H) and inhibited TAM-induced neurite outgrowth and β3Tub protein upregulation (Figures 3N–3Q, left). In contrast, TAM's effect on neurite outgrowth was not inhibited when using celecoxib, a control COX-2 inhibitor not affecting SPP1 expression (Figures 3N and 3O). Collectively, these data confirm the role of SPP1 as a required mediator of TAM-induced neural growth.

To assess whether SPP1 was sufficient to mediate the increase in neurite outgrowth, we supplemented the neuronal cultures with recombinant SPP1 (rSPP1) at concentrations comparable to those secreted by TAM (range 0.06 ng/mL–1 μg/mL) (Figures S3I and S3K). We found that rSPP1 supplementation, TAM-conditioned medium, and M2-like macrophages stimulated by hypoxia, a condition known to increase SPP1 expression,[51] did not affect neurite outgrowth in neurons derived from mNSCs and iPSC-MNs (Figures S3L and S3M). Conversely, supplementation of rSPP1 to shRNA-silenced *Spp1* TAMs restored their ability to promote neurite extension (Figures 3L and 3M).

In neurons, SPP1 signaling has been shown to promote neural maturation, which includes activation of the Rictor signaling pathway.[52] In line with this, TAMs increased Rictor expression in NSC-derived neurons (Figures 3P and 3Q, right). Notably, pharmacological inhibition of *Spp1* gene expression in TAMs prevented Rictor upregulation (Figures 3P and 3Q, right). While rSPP1 alone was insufficient to induce Rictor expression in neuronal cells (Figure S3K), supplementation of rSPP1 to shRNA-silenced *Spp1* TAMs rescued the increase in Rictor, confirming that SPP1 is a necessary yet not sufficient mediator of TAM-induced Rictor activation (Figures S3N and S3O).

These results indicate that SPP1 is required but not sufficient for TAM-mediated neural growth and Rictor activation, suggesting that a combination of multiple secreted factors and cell-cell interactions is necessary for TAM-neural growth activity.

To assess the role of Rictor in mediating the TAM-induced neural growth effect, we treated human iPSC-MNs with the Rictor inhibitor JRAB2011[53] and observed an impaired increase in TAM-induced β3Tub expression (Figures 3R and 3S). JRAB2011 alone did not alter β3Tub expression (Figures 3R and 3S). Similarly, lentiviral shRNA downregulation of Rictor expression in neurons derived from mNSCs ($mNSCs^{LV\ Rictor\text{-}KD}$, Figure S3P) reduced the TAM-induced β3Tub increased expression (Figures 3T and 3U), without affecting β3Tub expression in control $mNSCs^{LV\ Rictor\text{-}KD}$ and $mNSCs^{LV\ Scramble}$ (Figures 3T and 3U). Our results suggested that Rictor expression in neurons is required for the TAM-neural growth effect.

Altogether, these data indicate a direct role of TAMs in promoting neural growth, confirm SPP1 as a required but not sufficient mediator of TAM-induced Rictor activation and nerve growth, and identify Rictor as an essential signaling pathway for TAM-driven nerve growth (Figure 3V).

Adoptive transfer of TAMs promotes motor recovery in a scSCI mouse model

The adult mammalian CNS is characterized by maladaptive wound repair.[14] Unlike other tissues, CNS injury triggers the appearance of M2-like macrophages only in the early phase after injury.[12,13,54–58] Following SCI, M2-like macrophages migrate from the choroid plexus to the lesion site, and their inhibition exacerbates tissue damage and hinders functional recovery.[12] Although adoptive transfer of M2-like macrophages enhanced functional recovery in a preclinical mild SCI model,[59] they failed in a clinical trial.[60] M2-like macrophages are endowed with some tissue-healing properties. However, transcriptomic analysis highlighted that TAMs exhibit enhanced neuroregenerative and wound-healing potential compared with M2-like macrophages (Figure S1I), characterized by the expression of a neural growth gene signature and direct functional nerve growth-promoting properties (Figures 3A–3F). Leveraging this neural growth function, which added to the TAM wound-healing properties, we explored TAM's potential to repair a CNS lesion, such as SCI.

Most human SCI involve contusive and compressive injuries.[61–63] We established a validated preclinical severe complete-compressive-contusive spinal cord injury (scSCI) mouse model[64,65] to obtain a clinically relevant model, which develops a permanent complete loss of motor functions and mirrors the injury response observed in humans with complete SCI[66] (Figures 4A–4E; Videos S1A and S2A). In severe complete SCI, the primary insult causes extensive neural damage followed by progressive cell loss, inflammation, ischemia, and ECM disruption, leading to a large cyst that separates the rostral and caudal spinal cord.[67] The injured parenchyma is isolated from the intact neural tissue by a fibroglial scar, which inhibits regeneration and repair[68,69] (Figure 4B).

To assess the effect of TAM-neural growth property in scSCI, we performed intraparenchymal transplantation of 2×10^6 $TAM^{tdTomato}$ or $M2^{tdTomato}$ macrophages, or vehicle (0.9% NaCl solution), at the lesion site 3 days after the scSCI, corresponding to the subacute phase (2–4 dpi, Figure 4A).[66,68] $TAM^{tdTomato}$ and $M2^{tdTomato}$ transcriptomic analysis after 7 days from transplantation (t7) in the injured spinal cord showed that both cell phenotypes were transient, with a reduction of the neural growth and wound-healing gene lists expression, suggesting that repeated administrations of cells could improve their regenerative efficacy (Figures S4A–S4E). Accordingly, we increased the dose from 1 (Figures S4F–S4K) to 3 or 4 administrations, administered once a week (3, 10, 17, and 24 dpi), and ended the experiment at 37 or 57 dpi (Figure 4A). Motor function was assessed using two behavioral scales: the Basso, Beattie, Bresnahan (BBB) locomotor rating scale adapted for mice,[70,71] which is more sensitive for detecting improvements in stepping and coordination (see STAR Methods; Figures 4C–4E; Table S2), and the Basso Mouse Scale (BMS) (n = 97 total animals tested; Figures S4J and S4K; Table S2).[72] Unlike the commonly used SCI contusive mouse model (70 kdyn),[70–72] following scSCI,[64] mice experienced

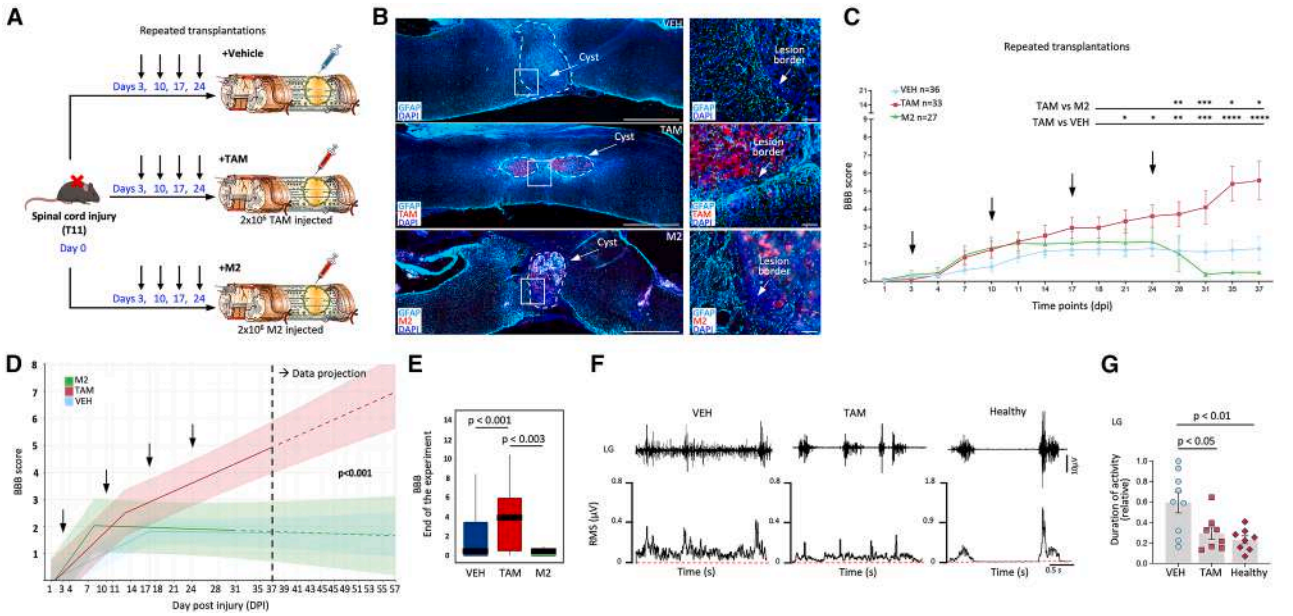

Figure 4. TAM transplantation promotes partial motor functional recovery after scSCI

(A) Vehicle (VEH), mouse TAMs (TAM), and M2-like macrophages (M2) administration workflow in scSCI.

(B) Images and magnification of GFAP expression from VEH-, TAM-, and M2-. Scale bar, 200 and 10 μm, respectively.

(C) BBB score of VEH-, TAM-, and M2-treated scSCI mice. Arrows mark the injection day.

(D) Mixed-effect regression model of BBB score. Arrows mark the injection day. Dashed lines indicate predicted post-experiment response.

(E) Mean BBB score of VEH- and TAM-treated scSCI mice (31–37 dpi).

(F) LG electromyography traces in VEH-, TAM-treated scSCI, and healthy mice.

(G) LG duration of activity in VEH-, TAM-treated scSCI, and healthy mice.

Data are presented as mean ± SEM. Dots represent biological replicates.

See also Figure S4, Table S2, and Videos S1 and S2.

complete paralysis of the hind limb paws (Figures 4C–4E; Videos S1A and S2A). After scSCI, TAM-treated mice exhibited a progressive improvement of the hindlimb functionality compared with both vehicle and M2-like macrophages, reaching a significant partial motor recovery from day 21, with a mean BBB score at the end of the study (37 dpi) of 5.6 ± 1.09 (Figures 4C and 4E) corresponded to an extensive movement of at least one ankle (Video S2A). Similar to the vehicle, adoptive transfer of M2-like macrophages was not effective, showing no improvement of motor disability and never reaching the ability of a slight ankle movement (Figures 4C and 4E). The use of the linear mixed-effects regression model[73] with a single change point highlighted significant differences between the slopes of the vehicle- and M2-treated groups compared with the TAM-treated group (Figure 4D). By using this single change point regression model, the BBB score before the change point (13 dpi for TAMs; Table S2) grew linearly in all groups, and thereafter only the TAM group maintained a linear improvement with a slope of 0.102 ($p < 0.001$). The effect size (ratio of means) of TAM treatment was 2.7 (95% confidence interval [CI] 0.49–4.9; $p = 0.017$) and 11.64 (95% CI = 2.5–20.77; $p = 0.013$) compared with vehicle- and M2-treated groups, respectively (Table S2). Additionally, the model predicted that the TAM treatment would increase the BBB score from 4.94 at 37 dpi to 6.98 at 57 dpi, 10 days after the experimental endpoint (dashed lines in Figure 4D). In addition, TAM treatment resulted in significantly reduced ankle joint spasticity, a hallmark of upper MN impairment that develops after scSCI (Figures S4L–S4N; Table S2). This pathological spasticity is commonly associated with enhanced spinal reflex excitability, which arises due to the loss of inhibitory supraspinal inputs following SCI. A key contributor to this hyperexcitability is the increased density of excitatory (VGLUT1$^+$) synapses on spinal motor circuits.[74–78] Consistently, TAM treatment decreased excitatory VGLUT1$^+$ synapses in both rostral and caudal perilesional parenchyma (Figures S4O and S4P), indicating synaptic remodeling underlying motor recovery.

We observed comparable improvements in motor recovery when the first TAM treatment was started at 10 dpi, when cyst formation initiates and peak inflammation declines (Figure S4Q), therefore extending the therapeutic window for initial treatment.

In vivo electromyography (EMG) analysis of the foot extensor and flexor muscles during voluntary contractions in awake mice confirmed the long-lasting effect of TAM^{tdTomato} administration, which was in line with the stably maintained BBB score up to 57 dpi (Figure S4R) and the restored activity in extensor muscles (Figures 4F and 4G; Figures S4S and S4T). Notably, following TAM administrations, neural regeneration at 57 dpi, as assessed by NEUN and NF200 staining, was maintained to a similar extent as observed at 31dpi, further confirming the persistence of the TAM-mediated neuroprotective and pro-regenerative effects (Figure S4U).

The overall assessments of the motor function of TAM-treated mice show a significant long-lasting (57 dpi) partial recovery compared with vehicle- and M2-treated mice.

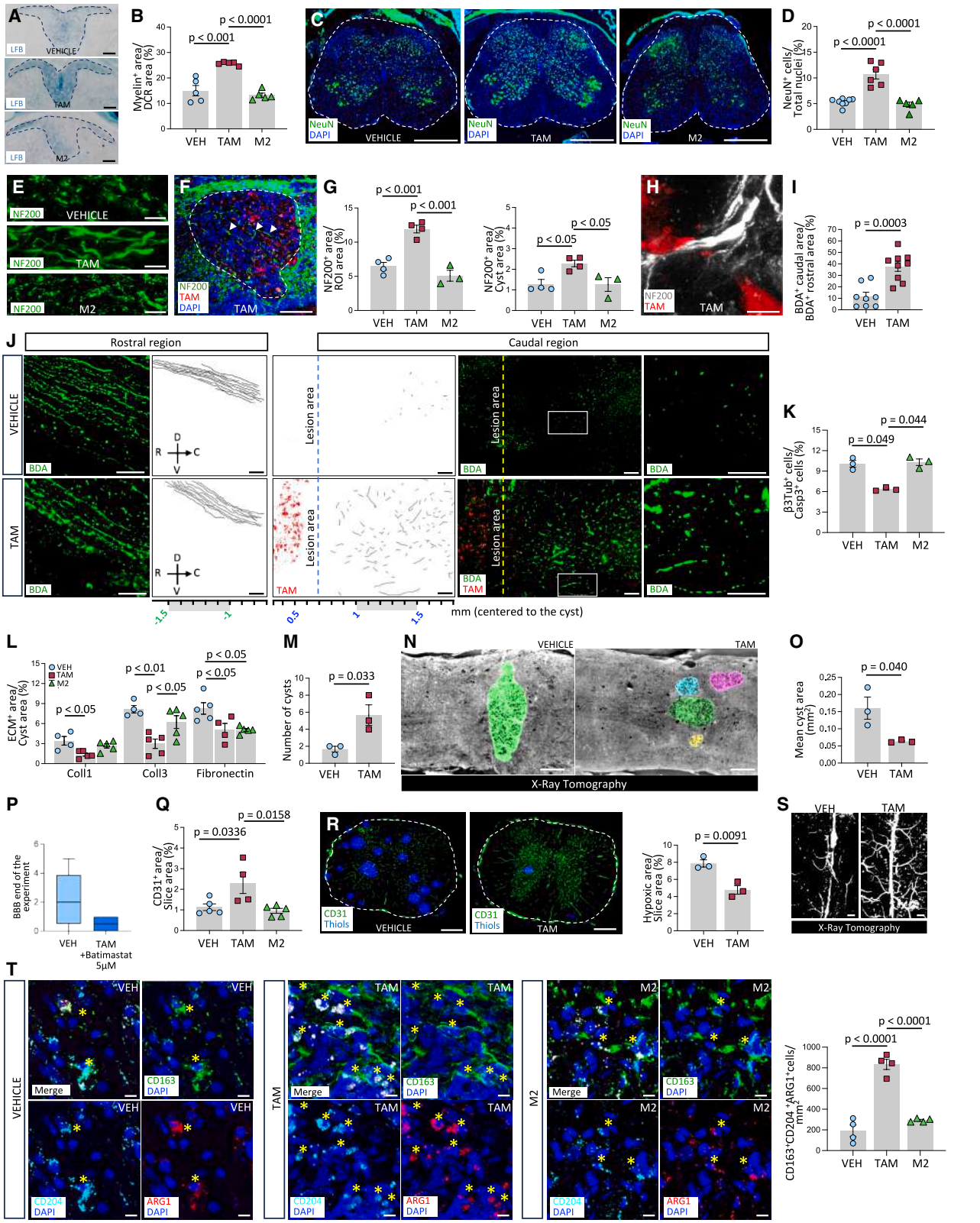

(legend on next page)

Adoptive transfer of TAMs promotes neural regeneration in scSCI

Bioluminescence imaging and immunohistochemistry confirmed a similar distribution of TAM^{tdTomato} and M2^{tdTomato} transplanted cells in the lesioned and peri-lesioned spinal cord parenchyma (Figures S4V–S4X). No tdTomato cells were found in other visceral organs, indicating that transplanted cells do not disseminate throughout the body (Figures S4Y and S4Z).

Adoptive transfer of TAM^{tdTomato}, but not M2^{tdTomato} macrophages, increased spinal cord neural parenchyma repair, promoted myelination (Figures 5A and 5B), doubled the number of NEUN and CHAT-expressing spinal neurons (Figures 5C and 5D; Figures S5A and S5B), and of the NF200^{+} axons in the injured spinal cord parenchyma and in those passing through the cyst (Figures 5E–5G), where the majority of TAM^{tdTomato} (>60%) were in close contact with axonal fibers (Figure 5H). In-depth analysis of axonal regrowth by tracing descending corticospinal tract fibers (CST) axons using biotinylated dextran amine (BDA)[79] showed a 3.4-fold increase in BDA-positive fibers reaching the region caudal to the lesion in TAM-treated mice (Figures 5I and 5J), indicating a higher number of axonal fibers crossing and extending through the cyst. We *in vitro* validated the direct trophic and pro-survival effects of TAMs on iPSC-MNs cultured under conditions of oxygen and glucose deprivation (OGD) (>50% cell survival; Figures 5K; Figure S5C).

Altogether, these data show that TAMs improve motor function in scSCI, which is supported by a direct effect on neuronal cell survival and axonal regrowth.

Adoptive transfer of TAMs heals the scSCI microenvironment through ECM remodeling

Efficient CNS repair requires not only neural regeneration but also restoration of the spinal cord parenchyma, including vascular perfusion, ECM reorganization, and mitigating chronic inflammation. Beyond their identified neural growth activity, TAMs exhibit wound-healing functions, such as ECM remodeling, angiogenesis, hypoxia response, immune modulation, and metabolic adaptation (Figures S1G–S1Z), which likely support tissue regeneration. We therefore evaluated the TAM pro-regenerative effects on ECM remodeling, angiogenesis, and immune modulation within the injured spinal cord parenchyma.

In the injured spinal cord parenchyma, cyst size and composition are the main aspects inhibiting spinal cord regeneration.[66] The cyst of TAM-treated mice decreased the expression of relevant ECM components,[66–69] such as collagen type-1 (Coll1), collagen type-3 (Coll3), and Fibronectin (Figure 5L; Figures S5D–S5F). Analysis of the cyst volume assessed using glial fibrillary acidic protein (GFAP)-stained tissues showed no differences in volumes between the different experimental groups (Figure S5G). In addition to GFAP-stained tissues, we assessed cyst morphology employing X-ray phase-contrast microcomputed tomography, which allows objective tissue analysis at micrometer resolution[80–83] (Figures 5M–5O; Figures S5H–S5J). The cysts in vehicle-treated samples appeared as a single compact structure, completely separating the rostral and caudal spinal cord parenchyma (Figures 5M and 5N; Figure S5I; Video S1B). In contrast, cysts in TAM-treated spinal cords appeared fragmented into small and multiple lobes (Figures 5M and 5N; Figure S5J; Video S2B), with a mean of 2.5-fold smaller area that did not disrupt the spinal tracts (Figures 5N and 5O). These data suggested that TAMs induce cyst remodeling by MMP-dependent ECM. By using pharmacological inhibition of MMPs with Batimastat[84,85] (Figure S5K), which did not impair TAM-induced neurite outgrowth *in vitro* (Figure S5L), we confirmed that MMP activity is essential for the beneficial effects of TAM on scSCI (Figure 5P; Figures S5M and S5N).

Adoptive transfer of TAMs heals the scSCI microenvironment through angiogenesis and tissue oxygenation

TAMs are described to support angiogenesis through VEGF in tumors.[43] We confirmed that *in vitro*-generated TAMs secrete VEGFA (Figure S2H), and that adoptive transfer of TAMs was able to promote angiogenesis in a Tg(*fli1a*:GFP)^{y1} zebrafish model (Figures S1T–S1V). Accordingly, TAM-treated scSCI enhanced the expression of CD31^{+} vessels, which exhibited an increased mean

Figure 5. TAM transplantation promotes neural regeneration after scSCI

(A and B) Images and quantification of LFB expression in the dorsal column region (DCR) of scSCI mice. Dashed line delineates the DCR. Scale bar, 100 μm.
(C and D) Images and quantification of Neun^{+} cells from vehicle (VEH), mouse TAMs (TAM), and M2-like macrophages (M2) treated spinal cord sections. Scale bar, 500 μm.
(E–G) Images and quantification of NF200 expression from VEH-, TAM-, and M2-treated spinal cord sections and cysts. Dashed line delineates the cyst. White arrows show NF200 expression inside the cyst. Scale bar, 100 μm.
(H) Magnification of a TAM and NF200^{+} axon in the scSCI parenchyma. Scale bar, 5 μm.
(I and J) Quantification, images, magnification, and NeuronJ reconstruction of BDA expression rostral and caudal to the lesion in VEH and TAM spinal cord sections. Scale bar, 100 μm.
(K) Quantification of β3Tub^{+} cells among CASP3^{+} iPSC-MNs.
(L) ECM markers expression in VEH, TAM, and M2 cysts.
(M) Number of cysts in VEH- and TAM-treated scSCI mice.
(N) 3D X-ray tomography cyst reconstruction from VEH and TAM spinal cords. Scale bar, 200 μm.
(O) Cyst area in VEH- and TAM-treated scSCI mice.
(P) Mean BBB score of VEH- and TAM+Batimastat-treated scSCI mice (28 dpi).
(Q) CD31^{+} expression in VEH-, TAM-, and M2-treated spinal cord sections.
(R) Images and quantification of reduced thiol area in VEH- and TAM-treated spinal cord sections. Scale bar, 500 μm.
(S) 3D X-ray tomography images of spinal cord vessels from VEH- and TAM-treated scSCI mice. Scale bar, 150 μm.
(T) Quantification and magnification of CD163^{+}/CD204^{+}/ARG1^{+} cells in VEH, TAM, and M2 spinal cord sections. Asterisks indicate CD163^{+}/CD204^{+}/ARG1^{+} cells. Scale bar, 10 μm.
Data are presented as mean ± SEM. Dots represent biological replicates.
See also Figure S5, Table S3, and Videos S1 and S2.

branch number and mean maximum vessel length (Figures S5O–S5R). Consistently, TAMs reduced 1.7-fold the hypoxic area in scSCI (Figure 5R). Furthermore, Z-maximum projections of the entire spinal cord X-ray phase-contrast micro-computed tomography volumes showed an increased blood vasculature in TAM-treated spinal cords (Figure 5S; Videos S1C and S2C). These data show that TAM administration promoted angiogenesis and spinal cord tissue oxygenation in scSCI.

Adoptive transfer of TAMs heals the scSCI microenvironment through immune modulation

The SCI microenvironment favors a persistent inflammatory setting associated with prolonged M1-like macrophage polarization of infiltrating macrophages, which may contribute to the spinal cord's failure to regenerate and repair.[60,86] To assess the ability of TAMs to modulate scSCI chronic inflammation, we quantified the endogenous M1- and M2-like macrophage populations in lesioned spinal cords (Figure 5T; Figures S5S–S5X). TAM treatment showed a reduction of $CD68^+$, $iNOS^+$ M1-like macrophages, with a parallel increase of $CD206^+$, and $CD163^+$, $ARG1^+$, $CD204^+$ M2-like macrophages (Figure 5T; Figures S5S, S5T, S5W, and S5X), suggesting a TAM immune-modulatory effect promoting M2 polarization, which is typically associated with the wound-healing process.[57]

Collectively, these results indicate that TAM has a neuroregenerative property and can modulate the scSCI-induced microenvironment by increasing ECM-remodeling, angiogenesis, and modulating chronic inflammation.

Preclinical long-term tumorigenicity and toxicity assessment confirms the safety of adoptive transfer of TAMs in scSCI

To assess the translational safety of TAM therapy, we evaluated long-term toxicity and tumorigenicity after single or repeated intraparenchymal administration in laminectomized mice. 1 year post-transplantation, no changes in weight, behavior, or locomotion were detected, and histopathological analysis revealed no visceral abnormalities or myeloid/macrophagic tumors (Figures S5Y and S5Z; Table S3).

SPP1 and Rictor pathways are key mediators of TAM-neural regenerative activity in scSCI

We have shown that TAM-induced neural growth, both in tumor and in *in vitro* neuronal cultures, is SPP1 dependent. Therefore, we investigated the role of SPP1 in TAM-mediated neural regeneration following scSCI. $TAM^{LV\ Spp1\text{-}KD}$ transplantation in scSCI failed to promote motor recovery, neuronal survival, axonal regeneration, and myelination compared with $TAM^{LV\ Scramble}$ (Figures 6A–6F; Figures S6A and S6B). Notably, we observed that $TAM^{LV\ Spp1\text{-}KD}$ retained its effects on the stromal compartment, including angiogenesis (Figures S6C and S6D) and ECM degradation (Coll3; Figures S6G–S6I), whereas we observed a decrease in $TAM^{LV\ Spp1\text{-}KD}$ immunomodulatory effect (Figures S6E, S6F, and S6J–S6M). In line with previous findings,[30] direct rSPP1 administration alone was not sufficient to improve functional outcomes following scSCI (Figures S6N and S6O). Overall, these data indicate that TAMs promote spinal cord repair through several molecular factors, and that SPP1 is required for the TAM-mediated neural growth and immunomodulatory effects.

Whole proteomic profile revealed clear differences between the treated and untreated scSCI tissue proteomes (Figure 6G; Figures S6P–S6S). TAM-treated spinal cord tissue showed more upregulated proteins related to neurons, synapses, and myelin than M2-treated spinal cord tissue (Figure 6H). The enrichment analysis on identified differentially abundant proteins (DAPs) and the enriched ingenuity pathway analysis (IPA) terms revealed a significant enrichment of 29 core pathways and 9 upstream regulators (Figure 6I). Of note, in line with our *in vitro* data, an unbiased analysis of upstream regulators associated with the DAPs unveiled that TAM-treated spinal cords showed an upregulation of Rictor (Figures 6I and 6J). Rictor overexpression in SCI is shown to promote SCI recovery.[87] This TAM effect appeared to require SPP1 expression, since the injection of $TAM^{LV\ Spp1\text{-}KD}$ prevented the Rictor increase in spinal cord neurons (Figures 6K and 6L). We induced the adenoviral shRNA downregulation of Rictor in the lesioned spinal cord by injecting the $AAV9^{shRictor}$ vector at 3, 10, and 17 dpi. $AAV9^{shRictor}$ vector efficiently transduced the injured parenchyma (Figure 6M), reduced Rictor (Figures 6N and 6O), and decreased its downstream Rho-family mediators[88] (Figures 6P–6R). Of note, the locomotor recovery in TAM-treated $Rictor^{KD}$ mice was significantly reduced (Figure 6S). These data are consistent with the role of Rictor and the mTORC2 pathway in TAM-induced therapeutic effect for SCI.

hTAMs show neural growth functional phenotype

Single-cell transcriptomic data on multiple tumor samples showed that human and mouse TAM display a neural growth signature (Figure 1D). We first confirmed that *in vitro*-generated human TAMs (hTAMs) expressed bona fide *in vivo*-TAM molecular profile and functions (Figures 7A and 7B; Figures S7A–S7E), including the *in vivo* defined TAM gene signature,[19] key TAM protein hallmarks ($CD206^{bight}$, $CD163^{bight}$, $CXCR4^{bight}$, $VEGFA^{bight}$, $HIF1A^{bight}$), and chemotactic property (Figures S7F–S7H). Consistently, hTAMs, but not hM2-like macrophages, significantly upregulated the identified neural growth gene signature (Figure 7C) and enhanced neural growth in iPSC-MNs-differentiated human neuronal cells (Figures 7D–7F). We found hTAMs located in close contact with neurons (Figure 7D; Figure S7I). Similarly, hTAMs showed a direct trophic and pro-survival effect on SH-SY5Y-differentiated neuronal cells (>50%) in conditions of OGD (Figure S7J). SPP1 gene and protein were highly expressed by hTAMs (Figures 7G–7J; Figures S7K and S7L). Accordingly, pharmacological (parecoxib) or small interfering RNA (siRNA) genetic ($hTAM^{siRNA\ SPP1\text{-}KD}$) SPP1 inhibition in hTAMs (Figure 7K) significantly reduced neurite outgrowth in both iPSC-MNs and in SH-SY5Y-differentiated neuronal cells (Figures 7L–7O, 7R, and 7S). This effect was not observed when using celecoxib, a COX-2 inhibitor not affecting SPP1 expression (Figures 7L–7N and 7R). rSPP1 supplementation, TAM-conditioned medium, and M2-like macrophages stimulated by hypoxia, a condition known to increase SPP1 expression,[51] did not affect neurite outgrowth in SH-SY5Y-differentiated neuronal cells (Figures S7M and S7N). Pharmacological inhibition of Rictor activity (JRAB2011) inhibited hTAM effect on neurite outgrowth in both SH-SY5Y-differentiated neuronal cells (Figures 7P and 7T) and in iPSC-MNs (Figures 7Q and 7U).

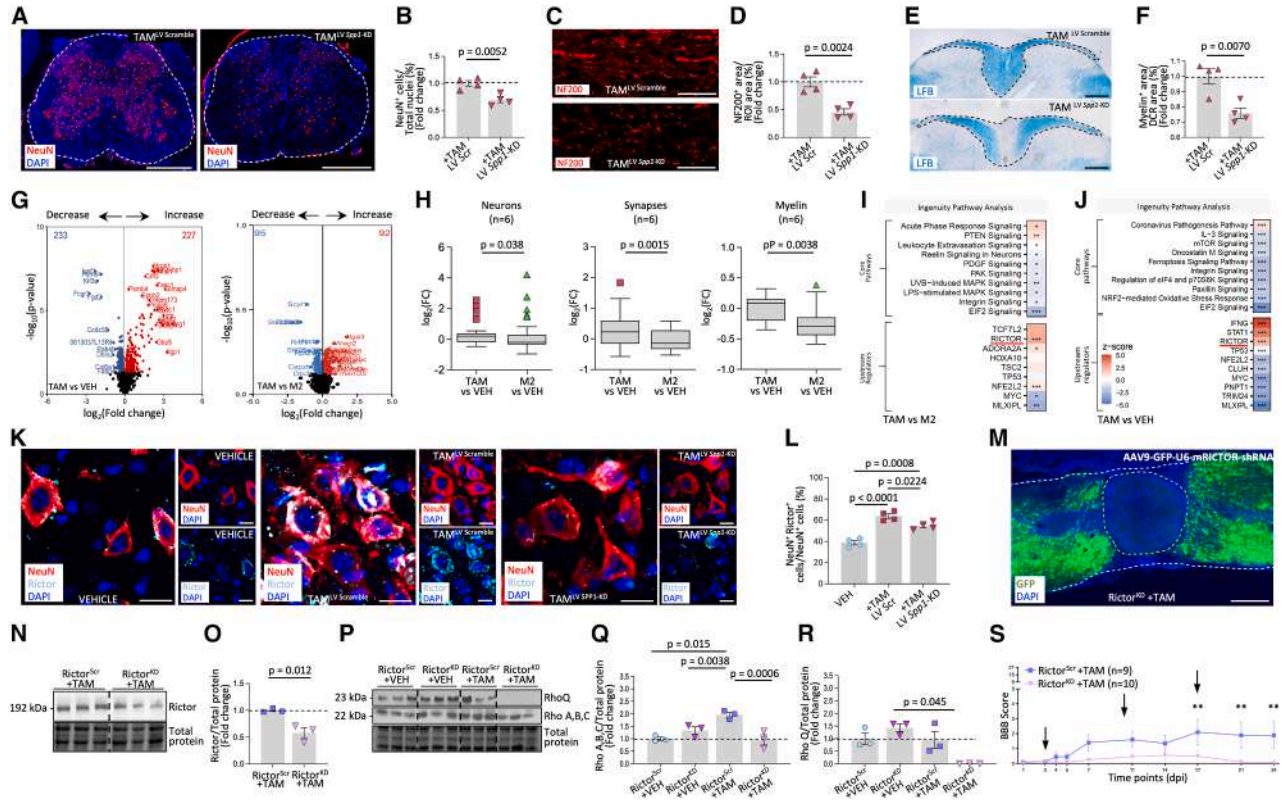

Figure 6. SPP1 and Rictor functional role in TAM therapeutic effect in scSCI

(A and B) Images and quantification of NEUN^{+} cells in TAM$^{LV\ Scramble}$ and TAM$^{LV\ Spp1\text{-}KD}$ spinal cord sections. Scale bar, 500 μm.

(C and D) Images and quantification of NF200 expression in TAM$^{LV\ Scramble}$ and TAM$^{LV\ Spp1\text{-}KD}$ spinal cord sections. Scale bar, 50 μm.

(E and F) Images and quantification of LFB expression in the dorsal column region (DCR) of TAM$^{LV\ Scramble}$ and TAM$^{LV\ Spp1\text{-}KD}$ spinal cord sections. Scale bar, 100 μm.

(G) Volcano plots of protein abundance in vehicle (VEH), mouseTAMs (TAM), and M2-like macrophages (M2) treated spinal cords (TAM: $n = 7$; M2: $n = 7$; VEH: $n = 6$).

(H) Quantifications of neuron, synapse, and myelin-related proteins in M2 and TAM-treated scSCI mice.

(I and J) IPA of significant core pathways and upstream regulators in TAM vs. M2 and in TAM vs. VEH protein extracts from scSCI spinal cord.

(K and L) Images and quantification of Rictor^{+} cells among NEUN^{+} cells in VEH-, TAM^{LVScramble}, and TAM$^{LV\ Spp1\text{-}KD}$ spinal cord sections. Scale bar, 15 μm.

(M) Distribution of AAV9 Rictor^{KD} GFP viral vector in spinal cord parenchyma. Yellow dashed line delineates the cyst. Scale bar, 200 μm.

(N and O) Immunoblot and quantification of Rictor expression in TAM-treated Rictor^{Scr} and Rictor^{KD} spinal cords. Blot was cropped to remove irrelevant lanes for clarity.

(P–R) Immunoblot and quantification of RHOQ and RHOA, B, and C expression in VEH and TAM-treated Rictor^{Scr} and Rictor^{KD} spinal cords. Blot was cropped to remove irrelevant lanes for clarity.

(S) BBB score of TAM-treated Rictor^{Scr} and TAM-treated Rictor^{KD} scSCI mice.

Data are presented as mean ± SEM. Dots represent biological replicates.

See also Figure S6.

Altogether, these findings show that, in addition to features related to wound healing, hTAMs are endowed with a neuroregenerative phenotype and enhance neural growth. We confirmed SPP1 as a necessary neural growth effector, and Rictor as a mediator of hTAM effect on neurons.

DISCUSSION

Beyond neurotransmission, nerves play essential roles in organogenesis,[89,90] tissue repair, and regeneration in adulthood.[91] They also have a role in supporting tumor growth and metastasis,[92] contributing through nerve-secreted factors to enhance tumor aggressiveness.[93] Conversely, several tumor types promote neural growth and infiltration, establishing a self-sustaining feed-forward loop between nerves and cancer cells.[1] Tumor progression is also fostered by a dynamic relationship between stromal and cancer cells, with TAMs providing a major contribution in this context.[3,20] Neurotransmitters have been shown to support the pro-tumoral functions of TAMs;[1,94–96] however, TAM's role in tumor innervation development remains unclear. In this work, we report that TAMs exhibit distinctive nerve growth properties and contribute to fostering tumor innervation. Our *in vitro* and *in vivo* data indicate a direct role of TAMs in neurite outgrowth, suggesting the establishment of a vicious circle between TAMs and neuronal growth during tumor progression. Given the intricate cellular and molecular crosstalk within the tumor microenvironment, TAMs may also initiate signaling cascades in other cellular compartments that ultimately promote neural invasion. However, in this work we provided evidence that TAMs, but not other cancer cells or tumor microenvironment cells, specifically express a neural growth gene signature (Table S1) in various cancer types, including GBM, fibrosarcoma, pancreatic, breast, endometrial, and

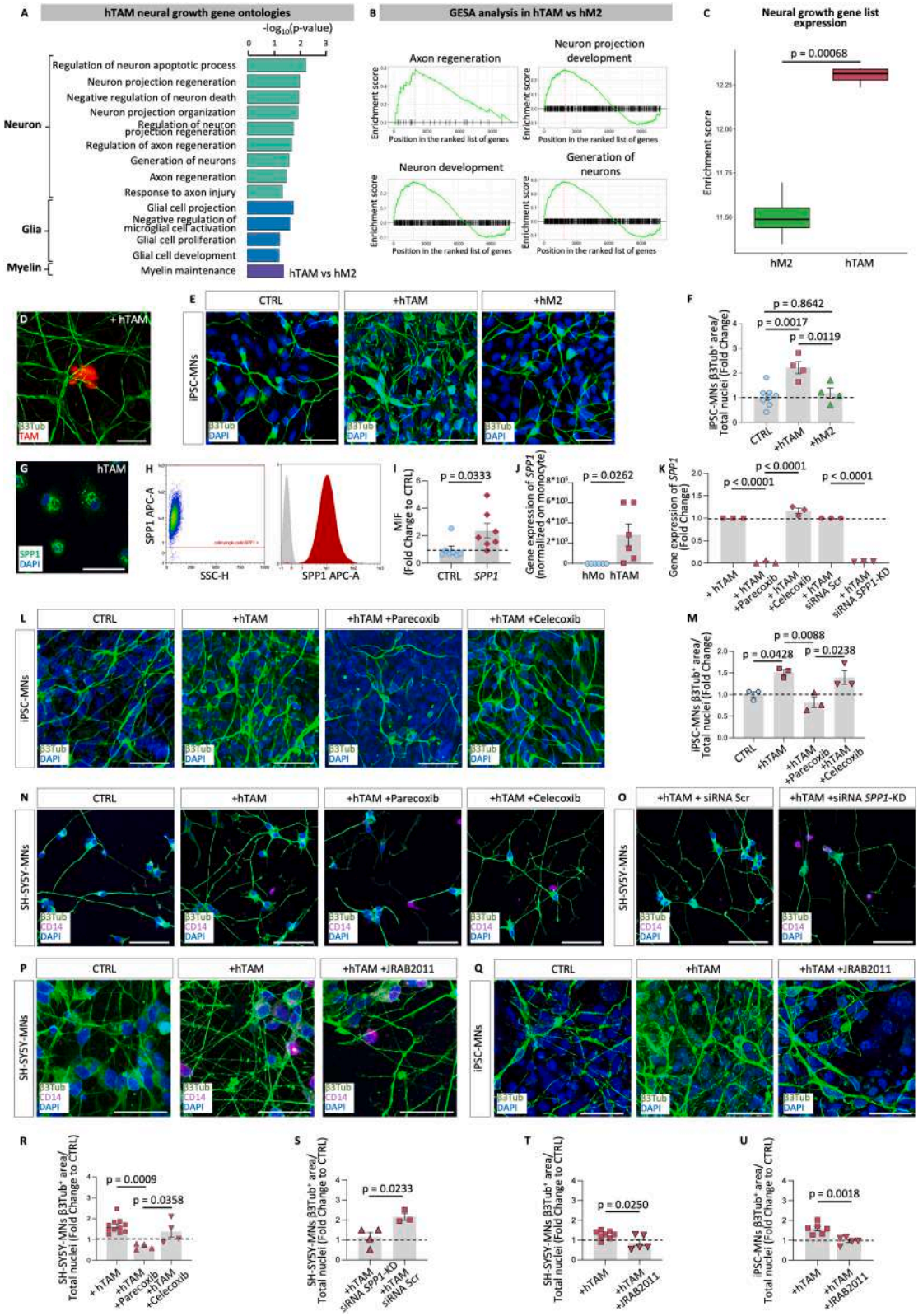

Figure 7. hTAMs display neural regenerative properties

(A) Quantification of neural growth-related enriched gene ontologies in human TAMs (hTAM) compared with human M2-like macrophages (hM2).

(B) Gene enrichment set analysis (GESA) of neuro-related gene ontologies of hTAM compared with hM2.

(legend continued on next page)

colorectal cancers, which is preserved across different species (human and mouse) and it is retained in *in vitro* settings. Notably, our data showed a direct role of TAMs in neurite and axonal outgrowth, even in the absence of other tumor microenvironment cells and factors, since TAM-neural growth-promoting function was validated in adult mammalian CNS injury.

We identified SPP1 as a relevant factor produced by TAMs and required to enhance nerve growth *in vitro*, in tumors, and in the injured CNS. SPP1 is known to contribute to bone development, wound healing,[97] and cancer progression[98] and is associated with poor prognosis in different tumor types,[99–101] although the underlying molecular mediators remain unclear. This study now reveals a direct role of SPP1 as a TAM-mediated factor involved in cancer-dependent nerve growth, potentially supporting its negative prognostic value. SPP1 exerts neurotrophic functions in the developing[27] and adult brain,[26] the peripheral nervous system,[29] and neurons.[31,52] Overall, our data indicate that SPP1 was necessary but not sufficient for TAM-induced neural growth and immunomodulation in scSCI, while angiogenesis and ECM remodeling occurred independently of SPP1. rSPP1 alone did not reproduce TAM therapeutic effects, indicating that TAM-mediated neural regeneration relies on additional secreted factors and direct cell-cell interactions.

SPP1 signaling has been shown to promote neural maturation by activating the Rictor signaling pathway in neurons.[31,52] Our data suggested that SPP1, produced by TAMs, is required for Rictor activation in neuronal cultures and following scSCI. In line with previous evidence that Rictor activation improves motor recovery in mild SCI, we found that TAM's therapeutic effect relies on Rictor induction in the spinal cord parenchyma.[87]

We leveraged this neural growth property of TAMs to promote neural regeneration. Following severe SCI tissue loss, inflammation, and ischemia, a hostile microenvironment is created that inhibits repair and leads to cyst formation and permanent deficits.[61,62] Consistent with their activity in tumors, our data indicated that TAM administration in scSCI mitigated key pathological events by reducing tissue ischemia, modulating inflammation, and promoting ECM remodeling.[5,102] These effects complement the TAM neuroregenerative potential as indicated by increased neuronal survival, axonal regrowth, myelination, and improved motor and electrophysiological recovery. Notably, while M2-like macrophages exhibit some therapeutic benefit in mild SCI models,[103–105] they failed to promote recovery in severe human SCI[11,60] and were likewise ineffective in our severe preclinical scSCI model.[65] In contrast, TAM adoptive transfer promoted functional recovery in severe SCI through multiple synergistic cellular and molecular mechanisms, driving comprehensive neural tissue regeneration and repair.

Long-term preclinical assessment of TAM adoptive transfer confirmed its safety, with no major histopathological alterations or tumor formation observed in the spinal cord or visceral organs. The neuroregenerative phenotype of TAMs was conserved in humans, as hTAMs displayed a neural growth signature in addition to ECM remodeling, angiogenesis, and immune modulation pathways. Consistent with murine data, hTAMs promoted neurite outgrowth via SPP1, which was required for neuronal Rictor activation. These findings support the translational potential of TAMs as a safe and effective disease-modifying cell therapy for CNS lesions. Moreover, the additional neural growth role of TAMs in tumors may be considered a further therapeutic target to reduce neural addiction in cancer.[106]

Limitations of the study

Although our data identify SPP1 as a necessary mediator of TAM-induced neural growth and regeneration, the complete molecular mechanisms underlying the TAM nerve growth effect remain to be elucidated. SPP1 is required to induce TAM-dependent neuronal Rictor activation, yet it is not sufficient to fully reproduce the TAM-mediated neurogenic or regenerative responses, suggesting the involvement of additional cofactors or cell-cell interactions. It is possible that TAMs provide a combination of soluble cues, including SPP1, and cell contact-dependent signals that converge on the neuronal mTORC2-Rictor pathway to promote axonal growth and repair. The identity and relative contribution of these factors remain to be fully elucidated. A comprehensive understanding of the molecular dialogue between TAMs and neurons could ultimately enable selective modulation of this interaction to either limit tumor innervation or enhance TAM-induced CNS regeneration.

RESOURCE AVAILABILITY

Lead contact

Request and further information and resources should be directed to and will be fulfilled by the lead contact, Ilaria Decimo (ilaria.decimo@univr.it).

(C) Neural growth gene list enrichment in hM2 and hTAM.
(D) Magnification of human iPSC-MNs co-cultured with hTAM stained with β3Tub. Scale bar, 10 μm.
(E and F) Immunofluorescence and quantification of β3Tub expression in human iPSC-MNs CTRL or +hTAM or +hM2. Scale bar, 50 μm.
(G) Image of hTAM stained with SPP1. Scale bar, 10 μm.
(H and I) hTAM flow cytometry graph and barplot of SPP1 expression and unstained (CTRL) sample.
(J) Gene expression of SPP1 in hTAM and Mo (hMo).
(K) Gene expression of SPP1 in hTAM, hTAM + parecoxib, hTAM + celecoxib, $hTAM^{siRNAScr}$, and $hTAM^{siRNASPP1\text{-}KD}$.
(L and M) Images and barplot of β3Tub expression in human iPSC-MNs CTRL or with hTAM w/o parecoxib or celecoxib. Scale bar, 10 μm.
(N) β3Tub immunofluorescence of SH-SY5Y-MNs co-cultured with hTAM w/o parecoxib or celecoxib. Scale bar, 50 μm.
(O) β3Tub immunofluorescence of SH-SY5Y-MNs co-cultured with $hTAM^{siRNAScr}$, and $hTAM^{siRNASPP1\text{-}KD}$. Scale bar, 50 μm.
(P and Q) β3Tub immunofluorescence of SH-SY5Y-MNs and iPSC-MNs, CTRL or co-cultured with hTAMs w/o JRAB2011. Scale bar, 50 μm.
(R) Barplot of β3Tub expression in SH-SY5Y-MNs co-cultured with hTAMs w/o parecoxib or celecoxib.
(S) Barplot of β3Tub expression in SH-SY5Y-MNs co-cultured with $hTAM^{siRNAScr}$, and $hTAM^{siRNASPP1\text{-}KD}$.
(T and U) Barplots of β3Tub expression in SH-SY5Y-MNs or iPSC-MNs co-cultured with hTAM or hTAM +JRAB2011.
Data are presented as mean ± SEM. Dots represent biological replicates.
See also Figure S7.

Materials availability

This study did not generate new unique reagents or materials.

Data and code availability

GBM scRNA-seq, Zenodo: https://zenodo.org/record/6046299#.YgZ6bpbSKN4; bulk RNA-seq of mouse and human *in vitro*-generated M2-like macrophages and TAMs, BioStudies: S-BSST1497 and S-BSST1502. The proteomics raw data are accessible at PRIDE[107]: PXD038064 (username: reviewer_pxd038064@ebi.ac.uk, password: 8LrstclV).

ACKNOWLEDGMENTS

I.D. and F. Ciarpella acknowledged the support provided by NextGenerationEU (PE0000006) project MNESYS, funded under the National Recovery and Resilience Plan (PNRR) of MIUR, and EU project FETPROACT-2018-2020 HERMES (824164). We thank patient associations GALM and La Colonna. We are grateful to E. Lorenzetto, G. Finotti of the CPT, and S. Rotondo of the CIRSAL at the University of Verona for technical assistance. K.S. and I.K. acknowledge support from the UFZ-funded platform ProMetheus. F. Bifari acknowledges support from PRIN 2022 (2022LB4X3N). M.E. acknowledges support from the Cancer Research UK; UK Medical Research Council (CC0103); the Wellcome Trust (221367/Z/20/Z, CC0103); EPSRC EP/R513143/1; the National Research Facility for Lab X-ray CT (NXCT, EP/T02593X/1 and EP/V035932/1); the beamtime MG32416 on ID13-2; and the assistance of the beamline scientists. We thank Prof. A. Mantovani, Prof. G. Racagni, Dr. T. Redaelli, Prof. F. Marchesi, Prof. A. Martin-Villalba, and Prof. F. Ginhoux for useful discussions; and A. Mattè, R. Esposito, R. Zamfir, L. Binaschi, A. Lattanzi, T. Marawanyika, C. Amoroso, G. Fierabracci, S. Zorzin, G. Pedrotti, and N. Domenichini for technical assistance.

AUTHOR CONTRIBUTIONS

S.D., F. Bifari, and I.D. conceptualize the study. S.D., E.R., N.P., G.F.F., and M.L.: data curation and results interpretation. S.D., L.M., E.R., E.B., F. Ciarpella, N.P., I.K., M.D.C., B.S., B.L., G.P., I.B., A. Campanelli, F. Cersosimo, E. Setten, Z.M., G.B., A. Pezzotta, A. Castagna, N.M., S.F., F. Boschi, A.D., M.T.S., C.C., G.M., A.A., L.S., V.S., P.C., E. Scanziani, A. Pistocchi, P.B., M.E., and K.S.: formal analyses and investigations. B.S., E. Setten, S.G., and P.B. provided resources. S.D., L.M., E.R., F. Ciarpella, and N.P.: validation. S.D., E.R., G.F.F., M.L., F. Bifari, and I.D. wrote the manuscript. F. Bifari and I.D. supervised the study. I.D. (lead contact) conceived, acquired funding, and oversaw project administration and integration of the experimental activities.

DECLARATION OF INTERESTS

I.D., F. Bifari, M.L., S.D., and G.F.F. are inventors of the patent PCT/EP2022/057246. I.D., F. Bifari, M.L., and G.F.F. are co-founders of HEMERA s.r.l., a spin-off of the University of Verona and the University of Milano, Italy.

STAR★METHODS

Detailed methods are provided in the online version of this paper and include the following:

- QUANTIFICATION AND STATISTICAL ANALYSIS
- ADDITIONAL RESOURCES

SUPPLEMENTAL INFORMATION

Supplemental information can be found online at https://doi.org/10.1016/j.immuni.2025.12.016.

Received: July 31, 2024
Revised: October 22, 2025
Accepted: December 18, 2025
Published: January 26, 2026

REFERENCES

1. Boilly, B., Faulkner, S., Jobling, P., and Hondermarck, H. (2017). Nerve Dependence: From Regeneration to Cancer. Cancer Cell *31*, 342–354. https://doi.org/10.1016/j.ccell.2017.02.005.
2. Pavlov, V.A., and Tracey, K.J. (2017). Neural regulation of immunity: molecular mechanisms and clinical translation. Nat. Neurosci. *20*, 156–166. https://doi.org/10.1038/nn.4477.
3. Noy, R., and Pollard, J.W. (2014). Tumor-associated macrophages: from mechanisms to therapy. Immunity *41*, 49–61. https://doi.org/10.1016/j.immuni.2014.06.010.
4. Cavel, O., Shomron, O., Shabtay, A., Vital, J., Trejo-Leider, L., Weizman, N., Krelin, Y., Fong, Y., Wong, R.J., Amit, M., et al. (2012). Endoneurial macrophages induce perineural invasion of pancreatic cancer cells by secretion of GDNF and activation of RET tyrosine kinase receptor. Cancer Res. *72*, 5733–5743. https://doi.org/10.1158/0008-5472.Can-12-0764.
5. Mantovani, A., Biswas, S.K., Galdiero, M.R., Sica, A., and Locati, M. (2013). Macrophage plasticity and polarization in tissue repair and remodelling. J. Pathol. *229*, 176–185. https://doi.org/10.1002/path.4133.
6. Feng, R., Muraleedharan Saraswathy, V., Mokalled, M.H., and Cavalli, V. (2023). Self-renewing macrophages in dorsal root ganglia contribute to promote nerve regeneration. Proc. Natl. Acad. Sci. USA *120*, e2215906120. https://doi.org/10.1073/pnas.2215906120.
7. Kolter, J., Feuerstein, R., Zeis, P., Hagemeyer, N., Paterson, N., d'Errico, P., Baasch, S., Amann, L., Masuda, T., Lösslein, A., et al. (2019). A Subset of Skin Macrophages Contributes to the Surveillance and Regeneration of Local Nerves. Immunity *50*, 1482–1497.e7. https://doi.org/10.1016/j.immuni.2019.05.009.
8. De Schepper, S., Verheijden, S., Aguilera-Lizarraga, J., Viola, M.F., Boesmans, W., Stakenborg, N., Voytyuk, I., Schmidt, I., Boeckx, B., Dierckx de Casterlé, I., et al. (2019). Self-Maintaining Gut Macrophages Are Essential for Intestinal Homeostasis. Cell *176*, 676. https://doi.org/10.1016/j.cell.2019.01.010.
9. Viola, M.F., Chavero-Pieres, M., Modave, E., Delfini, M., Stakenborg, N., Estévez, M.C., Fabre, N., Appeltans, I., Martens, T., Vandereyken, K., et al. (2023). Dedicated macrophages organize and maintain the enteric nervous system. Nature *618*, 818–826. https://doi.org/10.1038/s41586-023-06200-7.
10. Hakim, S., Jain, A., Petrova, V., Indajang, J., Kawaguchi, R., Wang, Q., Duran, E.S., Nelson, D., Adamson, S.S., Greene, C., et al. (2024). Macrophages protect against sensory axon degeneration in diabetic neuropathy. Preprint at bioRxiv. https://doi.org/10.1101/2024.01.30.577801.
11. Popovich, P.G., and Longbrake, E.E. (2008). Can the immune system be harnessed to repair the CNS? Nat. Rev. Neurosci. *9*, 481–493. https://doi.org/10.1038/nrn2398.
12. Shechter, R., Miller, O., Yovel, G., Rosenzweig, N., London, A., Ruckh, J., Kim, K.W., Klein, E., Kalchenko, V., Bendel, P., et al. (2013). Recruitment of beneficial M2 macrophages to injured spinal cord is orchestrated by remote brain choroid plexus. Immunity *38*, 555–569. https://doi.org/10.1016/j.immuni.2013.02.012.
13. Van Broeckhoven, J., Sommer, D., Dooley, D., Hendrix, S., and Franssen, A.J.P.M. (2021). Macrophage phagocytosis after spinal cord injury: when friends become foes. Brain *144*, 2933–2945. https://doi.org/10.1093/brain/awab250.
14. y Cajal, S.R. (1991). Cajal's Degeneration and Regeneration of the Nervous System. In History of Neuroscience (Oxford University Press).
15. Oh, K., Yoo, Y.J., Torre-Healy, L.A., Rao, M., Fassler, D., Wang, P., Caponegro, M., Gao, M., Kim, J., Sasson, A., et al. (2023). Coordinated single-cell tumor microenvironment dynamics reinforce pancreatic cancer subtype. Nat. Commun. *14*, 5226. https://doi.org/10.1038/s41467-023-40895-6.
16. Liu, T., Liu, C., Yan, M., Zhang, L., Zhang, J., Xiao, M., Li, Z., Wei, X., and Zhang, H. (2022). Single cell profiling of primary and paired metastatic lymph node tumors in breast cancer patients. Nat. Commun. *13*, 6823. https://doi.org/10.1038/s41467-022-34581-2.
17. Hsu, W.H., LaBella, K.A., Lin, Y., Xu, P., Lee, R., Hsieh, C.E., Yang, L., Zhou, A., Blecher, J.M., Wu, C.J., et al. (2023). Oncogenic KRAS Drives Lipofibrogenesis to Promote Angiogenesis and Colon Cancer Progression. Cancer Discov. *13*, 2652–2673. https://doi.org/10.1158/2159-8290.Cd-22-1467.
18. Ochocka, N., Segit, P., Walentynowicz, K.A., Wojnicki, K., Cyranowski, S., Swatler, J., Mieczkowski, J., and Kaminska, B. (2021). Single-cell RNA sequencing reveals functional heterogeneity of glioma-associated brain macrophages. Nat. Commun. *12*, 1151. https://doi.org/10.1038/s41467-021-21407-w.
19. Qian, J., Olbrecht, S., Boeckx, B., Vos, H., Laoui, D., Etlioglu, E., Wauters, E., Pomella, V., Verbandt, S., Busschaert, P., et al. (2020). A pan-cancer blueprint of the heterogeneous tumor microenvironment revealed by single-cell profiling. Cell Res. *30*, 745–762. https://doi.org/10.1038/s41422-020-0355-0.
20. Mantovani, A., Sozzani, S., Locati, M., Allavena, P., and Sica, A. (2002). Macrophage polarization: tumor-associated macrophages as a paradigm for polarized M2 mononuclear phagocytes. Trends Immunol. *23*, 549–555. https://doi.org/10.1016/S1471-4906(02)02302-5.
21. Pérez-Rodríguez, D.R., Blanco-Luquin, I., and Mendioroz, M. (2021). The Participation of Microglia in Neurogenesis: A Review. Brain Sci. *11*, 658. https://doi.org/10.3390/brainsci11050658.
22. Wang, R., Ren, C., Gao, T., Li, H., Bo, X., Zhu, D., Zhang, D., Chen, H., and Zhang, Y. (2024). SEPDB: a database of secreted proteins. Database (Oxford) *2024*, baae007. https://doi.org/10.1093/database/baae007.
23. Cappello, S., Attardo, A., Wu, X., Iwasato, T., Itohara, S., Wilsch-Bräuninger, M., Eilken, H.M., Rieger, M.A., Schroeder, T.T., Huttner, W.B., et al. (2006). The Rho-GTPase cdc42 regulates neural progenitor fate at the apical surface. Nat. Neurosci. *9*, 1099–1107. https://doi.org/10.1038/nn1744.
24. Hashimoto, M., Sun, D., Rittling, S.R., Denhardt, D.T., and Young, W. (2007). Osteopontin-deficient mice exhibit less inflammation, greater tissue damage, and impaired locomotor recovery from spinal cord injury compared with wild-type controls. J. Neurosci. *27*, 3603–3611. https://doi.org/10.1523/jneurosci.4805-06.2007.
25. Kavakebi, P., Hausott, B., Tomasino, A., Ingorokva, S., and Klimaschewski, L. (2005). The N-end rule ubiquitin-conjugating enzyme, HR6B, is up-regulated by nerve growth factor and required for neurite outgrowth. Mol. Cell. Neurosci. *29*, 559–568. https://doi.org/10.1016/j.mcn.2005.04.008.
26. Lan, Y., Zhang, X., Liu, S., Guo, C., Jin, Y., Li, H., Wang, L., Zhao, J., Hao, Y., Li, Z., et al. (2024). Fate mapping of Spp1 expression reveals age-dependent plasticity of disease-associated microglia-like cells after brain injury. Immunity *57*, 349–363.e9. https://doi.org/10.1016/j.immuni.2024.01.008.
27. Lawrence, A.R., Canzi, A., Bridlance, C., Olivié, N., Lansonneur, C., Catale, C., Pizzamiglio, L., Kloeckner, B., Silvin, A., Munro, D.A.D., et al. (2024). Microglia maintain structural integrity during fetal brain morphogenesis. Cell *187*, 962–980.e19. https://doi.org/10.1016/j.cell.2024.01.012.
28. Lin, E.Y.H., Xi, W., Aggarwal, N., and Shinohara, M.L. (2023). Osteopontin (OPN)/SPP1: from its biochemistry to biological functions in the innate

immune system and the central nervous system (CNS). Int. Immunol. *35*, 171–180. https://doi.org/10.1093/intimm/dxac060.

29. Liu, X., Sun, Y., Li, H., Li, Y., Li, M., Yuan, Y., Cui, S., and Yao, D. (2017). Effect of Spp1 on nerve degeneration and regeneration after rat sciatic nerve injury. BMC Neurosci. *18*, 30. https://doi.org/10.1186/s12868-017-0348-1.
30. Wang, Y., Su, H., Zhong, J., Zhan, Z., Zhao, Q., Liu, Y., Li, S., Wang, H., Yang, C., Yu, L., et al. (2023). Osteopontin enhances the effect of treadmill training and promotes functional recovery after spinal cord injury. Mol. Biomed. *4*, 44. https://doi.org/10.1186/s43556-023-00154-y.
31. Zhao, Q., Su, H., Jiang, W., Luo, H., Pan, L., Liu, Y., Yang, C., Yin, Y., Yu, L., and Tan, B. (2023). IGF-1 Combined with OPN Promotes Neuronal Axon Growth in Vitro Through the IGF-1R/Akt/mTOR Signaling Pathway in Lipid Rafts. Neurochem. Res. *48*, 3190–3201. https://doi.org/10.1007/s11064-023-03971-3.
32. Bowman, R.L., Klemm, F., Akkari, L., Pyonteck, S.M., Sevenich, L., Quail, D.F., Dhara, S., Simpson, K., Gardner, E.E., Iacobuzio-Donahue, C.A., et al. (2016). Macrophage Ontogeny Underlies Differences in Tumor-Specific Education in Brain Malignancies. Cell Rep. *17*, 2445–2459. https://doi.org/10.1016/j.celrep.2016.10.052.
33. Cassetta, L., Fragkogianni, S., Sims, A.H., Swierczak, A., Forrester, L.M., Zhang, H., Soong, D.Y.H., Cotechini, T., Anur, P., Lin, E.Y., et al. (2019). Human Tumor-Associated Macrophage and Monocyte Transcriptional Landscapes Reveal Cancer-Specific Reprogramming, Biomarkers, and Therapeutic Targets. Cancer Cell *35*, 588–602.e10. https://doi.org/10.1016/j.ccell.2019.02.009.
34. Chen, Z., Feng, X., Herting, C.J., Garcia, V.A., Nie, K., Pong, W.W., Rasmussen, R., Dwivedi, B., Seby, S., Wolf, S.A., et al. (2017). Cellular and Molecular Identity of Tumor-Associated Macrophages in Glioblastoma. Cancer Res. *77*, 2266–2278. https://doi.org/10.1158/0008-5472.Can-16-2310.
35. Gabanyi, I., Muller, P.A., Feighery, L., Oliveira, T.Y., Costa-Pinto, F.A., and Mucida, D. (2016). Neuro-immune Interactions Drive Tissue Programming in Intestinal Macrophages. Cell *164*, 378–391. https://doi.org/10.1016/j.cell.2015.12.023.
36. Khan, F., Pang, L., Dunterman, M., Lesniak, M.S., Heimberger, A.B., and Chen, P. (2023). Macrophages and microglia in glioblastoma: heterogeneity, plasticity, and therapy. J. Clin. Investig. *133*, e163446. https://doi.org/10.1172/jci163446.
37. Muller, P.A., Koscsó, B., Rajani, G.M., Stevanovic, K., Berres, M.L., Hashimoto, D., Mortha, A., Leboeuf, M., Li, X.M., Mucida, D., et al. (2014). Crosstalk between muscularis macrophages and enteric neurons regulates gastrointestinal motility. Cell *158*, 300–313. https://doi.org/10.1016/j.cell.2014.04.050.
38. Zhao, Z., Zou, S., Guan, X., Wang, M., Jiang, Z., Liu, Z., Li, C., Lin, H., Liu, X., Yang, R., et al. (2018). Apolipoprotein E Overexpression Is Associated With Tumor Progression and Poor Survival in Colorectal Cancer. Front. Genet. *9*, 650. https://doi.org/10.3389/fgene.2018.00650.
39. Germano, G., Frapolli, R., Belgiovine, C., Anselmo, A., Pesce, S., Liguori, M., Erba, E., Uboldi, S., Zucchetti, M., Pasqualini, F., et al. (2013). Role of macrophage targeting in the antitumor activity of trabectedin. Cancer Cell *23*, 249–262. https://doi.org/10.1016/j.ccr.2013.01.008.
40. Magrini, E., Di Marco, S., Mapelli, S.N., Perucchini, C., Pasqualini, F., Donato, A., Guevara Lopez, M.L., Carriero, R., Ponzetta, A., Colombo, P., et al. (2021). Complement activation promoted by the lectin pathway mediates C3aR-dependent sarcoma progression and immunosuppression. Nat. Cancer *2*, 218–232. https://doi.org/10.1038/s43018-021-00173-0.
41. Tessaro, F.H.G., Ko, E.Y., De Simone, M., Piras, R., Broz, M.T., Goodridge, H.S., Balzer, B., Shiao, S.L., and Guarnerio, J. (2022). Single-cell RNA-seq of a soft-tissue sarcoma model reveals the critical role of tumor-expressed MIF in shaping macrophage heterogeneity. Cell Rep. *39*, 110977. https://doi.org/10.1016/j.celrep.2022.110977.
42. Consonni, F.M., Bleve, A., Totaro, M.G., Storto, M., Kunderfranco, P., Termanini, A., Pasqualini, F., Alì, C., Pandolfo, C., Sgambelluri, F., et al. (2021). Heme catabolism by tumor-associated macrophages controls metastasis formation. Nat. Immunol. *22*, 595–606. https://doi.org/10.1038/s41590-021-00921-5.
43. Carmeliet, P., and Tessier-Lavigne, M. (2005). Common mechanisms of nerve and blood vessel wiring. Nature *436*, 193–200. https://doi.org/10.1038/nature03875.
44. Bossolasco, P., Sassone, F., Gumina, V., Peverelli, S., Garzo, M., and Silani, V. (2018). Motor neuron differentiation of iPSCs obtained from peripheral blood of a mutant TARDBP ALS patient. Stem Cell Res. *30*, 61–68. https://doi.org/10.1016/j.scr.2018.05.009.
45. Bifari, F., Decimo, I., Pino, A., Llorens-Bobadilla, E., Zhao, S., Lange, C., Panuccio, G., Boeckx, B., Thienpont, B., Vinckier, S., et al. (2017). Neurogenic Radial Glia-like Cells in Meninges Migrate and Differentiate into Functionally Integrated Neurons in the Neonatal Cortex. Cell Stem Cell *20*, 360–373.e7. https://doi.org/10.1016/j.stem.2016.10.020.
46. Ciarpella, F., Zamfir, R.G., Campanelli, A., Pedrotti, G., Di Chio, M., Bottani, E., and Decimo, I. (2023). Generation of mouse hippocampal brain organoids from primary embryonic neural stem cells. Star Protoc. *4*, 102413. https://doi.org/10.1016/j.xpro.2023.102413.
47. Ciarpella, F., Zamfir, R.G., Campanelli, A., Ren, E., Pedrotti, G., Bottani, E., Borioli, A., Caron, D., Di Chio, M., Dolci, S., et al. (2021). Murine cerebral organoids develop network of functional neurons and hippocampal brain region identity. iScience *24*, 103438. https://doi.org/10.1016/j.isci.2021.103438.
48. Blader, P., Plessy, C., and Strähle, U. (2003). Multiple regulatory elements with spatially and temporally distinct activities control neurogenin1 expression in primary neurons of the zebrafish embryo. Mech. Dev. *120*, 211–218. https://doi.org/10.1016/s0925-4773(02)00413-6.
49. Willems, S., Kilu, W., Ni, X., Chaikuad, A., Knapp, S., Heering, J., and Merk, D. (2020). The orphan nuclear receptor Nurr1 is responsive to non-steroidal anti-inflammatory drugs. Commun. Chem. *3*, 85. https://doi.org/10.1038/s42004-020-0331-0.
50. Zagani, R., Hamzaoui, N., Cacheux, W., de Reyniès, A., Terris, B., Chaussade, S., Romagnolo, B., Perret, C., and Lamarque, D. (2009). Cyclooxygenase-2 inhibitors down-regulate osteopontin and Nr4A2-new therapeutic targets for colorectal cancers. Gastroenterology *137*. 1358–66.e1. https://doi.org/10.1053/j.gastro.2009.06.039.
51. Raggi, F., Pelassa, S., Pierobon, D., Penco, F., Gattorno, M., Novelli, F., Eva, A., Varesio, L., Giovarelli, M., and Bosco, M.C. (2017). Regulation of Human Macrophage M1-M2 Polarization Balance by Hypoxia and the Triggering Receptor Expressed on Myeloid Cells-1. Front. Immunol. *8*, 1097. https://doi.org/10.3389/fimmu.2017.01097.
52. Roszkowska, M., Skupien, A., Wójtowicz, T., Konopka, A., Gorlewicz, A., Kisiel, M., Bekisz, M., Ruszczycki, B., Dolezyczek, H., Rejmak, E., et al. (2016). CD44: a novel synaptic cell adhesion molecule regulating structural and functional plasticity of dendritic spines. Mol. Biol. Cell *27*, 4055–4066. https://doi.org/10.1091/mbc.E16-06-0423.
53. Benavides-Serrato, A., Lee, J., Holmes, B., Landon, K.A., Bashir, T., Jung, M.E., Lichtenstein, A., and Gera, J. (2017). Specific blockade of Rictor-mTOR association inhibits mTORC2 activity and is cytotoxic in glioblastoma. PLoS One *12*, e0176599. https://doi.org/10.1371/journal.pone.0176599.
54. Beck, K.D., Nguyen, H.X., Galvan, M.D., Salazar, D.L., Woodruff, T.M., and Anderson, A.J. (2010). Quantitative analysis of cellular inflammation after traumatic spinal cord injury: evidence for a multiphasic inflammatory response in the acute to chronic environment. Brain *133*, 433–447. https://doi.org/10.1093/brain/awp322.
55. David, S., and Kroner, A. (2011). Repertoire of microglial and macrophage responses after spinal cord injury. Nat. Rev. Neurosci. *12*, 388–399. https://doi.org/10.1038/nrn3053.
56. Gensel, J.C., and Zhang, B. (2015). Macrophage activation and its role in repair and pathology after spinal cord injury. Brain Res. *1619*, 1–11. https://doi.org/10.1016/j.brainres.2014.12.045.
57. Kigerl, K.A., Gensel, J.C., Ankeny, D.P., Alexander, J.K., Donnelly, D.J., and Popovich, P.G. (2009). Identification of two distinct macrophage subsets with divergent effects causing either neurotoxicity or

regeneration in the injured mouse spinal cord. J. Neurosci. *29*, 13435–13444. https://doi.org/10.1523/jneurosci.3257-09.2009.

58. Milich, L.M., Choi, J.S., Ryan, C., Cerqueira, S.R., Benavides, S., Yahn, S.L., Tsoulfas, P., and Lee, J.K. (2021). Single-cell analysis of the cellular heterogeneity and interactions in the injured mouse spinal cord. J. Exp. Med. *218*, e20210040. https://doi.org/10.1084/jem.20210040.
59. Chen, J., Wu, Y., Duan, F.X., Wang, S.N., Guo, X.Y., Ding, S.Q., Zhou, J. H., Hu, J.G., and Lü, H.Z. (2019). Effect of M2 macrophage adoptive transfer on transcriptome profile of injured spinal cords in rats. Exp. Biol. Med. (Maywood) *244*, 880–892. https://doi.org/10.1177/1535370219854668.
60. Lammertse, D.P., Jones, L.A., Charlifue, S.B., Kirshblum, S.C., Apple, D.F., Ragnarsson, K.T., Falci, S.P., Heary, R.F., Choudhri, T.F., Jenkins, A.L., et al. (2012). Autologous incubated macrophage therapy in acute, complete spinal cord injury: results of the phase 2 randomized controlled multicenter trial. Spinal Cord *50*, 661–671. https://doi.org/10.1038/sc.2012.39.
61. Kirshblum, S.C., Waring, W., Biering-Sorensen, F., Burns, S.P., Johansen, M., Schmidt-Read, M., Donovan, W., Graves, D., Jha, A., Jones, L., et al. (2011). Reference for the 2011 revision of the International Standards for Neurological Classification of Spinal Cord Injury. J. Spinal Cord Med. *34*, 547–554. https://doi.org/10.1179/107902611X13186000420242.
62. Marino, R.J., Leff, M., Cardenas, D.D., Donovan, J., Chen, D., Kirshblum, S., and Leiby, B.E. (2020). Trends in Rates of ASIA Impairment Scale Conversion in Traumatic Complete Spinal Cord Injury. Neurotrauma Rep. *1*, 192–200. https://doi.org/10.1089/neur.2020.0038.
63. McDonald, J.W., and Sadowsky, C. (2002). Spinal-cord injury. Lancet *359*, 417–425. https://doi.org/10.1016/s0140-6736(02)07603-1.
64. Dolci, S., Mannino, L., Bottani, E., Campanelli, A., Di Chio, M., Zorzin, S., D'Arrigo, G., Amenta, A., Segala, A., Paglia, G., et al. (2022). Therapeutic induction of energy metabolism reduces neural tissue damage and increases microglia activation in severe spinal cord injury. Pharmacol. Res. *178*, 106149. https://doi.org/10.1016/j.phrs.2022.106149.
65. Dolci, S., Di Chio, M., Busetto, G., F, B., and I, D. (2025). Protocol to develop a preclinical severe contusive-compressive SCI mouse model for translational research. STAR Protoc. *7*, 104029. https://doi.org/10.1016/j.xpro.2025.104029.
66. Ahuja, C.S., Wilson, J.R., Nori, S., Kotter, M.R.N., Druschel, C., Curt, A., and Fehlings, M.G. (2017). Traumatic spinal cord injury. Nat. Rev. Dis. Primers *3*, 17018. https://doi.org/10.1038/nrdp.2017.18.
67. Mautes, A.E., Weinzierl, M.R., Donovan, F., and Noble, L.J. (2000). Vascular events after spinal cord injury: contribution to secondary pathogenesis. Phys. Ther. *80*, 673–687. https://doi.org/10.1093/ptj/80.7.673.
68. Oyinbo, C.A. (2011). Secondary injury mechanisms in traumatic spinal cord injury: a nugget of this multiply cascade. Acta Neurobiol. Exp. (Wars.) *71*, 281–299. https://doi.org/10.55782/ane-2011-1848.
69. Silver, J., and Miller, J.H. (2004). Regeneration beyond the glial scar. Nat. Rev. Neurosci. *5*, 146–156. https://doi.org/10.1038/nrn1326.
70. Basso, D.M., Fisher, L.C., Anderson, A.J., Jakeman, L.B., McTigue, D.M., and Popovich, P.G. (2006). Basso Mouse Scale for locomotion detects differences in recovery after spinal cord injury in five common mouse strains. J. Neurotrauma *23*, 635–659. https://doi.org/10.1089/neu.2006.23.635.
71. Cummings, B.J., Engesser-Cesar, C., Cadena, G., and Anderson, A.J. (2007). Adaptation of a ladder beam walking task to assess locomotor recovery in mice following spinal cord injury. Behav. Brain Res. *177*, 232–241. https://doi.org/10.1016/j.bbr.2006.11.042.
72. Basso, D.M., Beattie, M.S., and Bresnahan, J.C. (1995). A sensitive and reliable locomotor rating scale for open field testing in rats. J. Neurotrauma *12*, 1–21. https://doi.org/10.1089/neu.1995.12.1.
73. Cohen, J. (1988). Statistical Power Analysis for the Behavioral Sciences*567* (Lawrence Erlbaum Associates). https://doi.org/10.4324/9780203771587.
74. Brennan, F.H., Noble, B.T., Wang, Y., Guan, Z., Davis, H., Mo, X., Harris, C., Eroglu, C., Ferguson, A.R., and Popovich, P.G. (2021). Acute post-injury blockade of α2δ-1 calcium channel subunits prevents pathological autonomic plasticity after spinal cord injury. Cell Rep. *34*, 108667. https://doi.org/10.1016/j.celrep.2020.108667.
75. Brumovsky, P.R. (2013). VGLUTs in Peripheral Neurons and the Spinal Cord: Time for a Review. ISRN Neurol. *2013*, 829753. https://doi.org/10.1155/2013/829753.
76. Guttmann, L., and Whitteridge, D. (1947). Effects of bladder distension on autonomic mechanisms after spinal cord injuries. Brain *70*, 361–404. https://doi.org/10.1093/brain/70.4.361.
77. Weaver, L.C., Marsh, D.R., Gris, D., Brown, A., and Dekaban, G.A. (2006). Autonomic dysreflexia after spinal cord injury: central mechanisms and strategies for prevention. Prog. Brain Res. *152*, 245–263. https://doi.org/10.1016/s0079-6123(05)52016-8.
78. Zhang, Y., Guan, Z., Reader, B., Shawler, T., Mandrekar-Colucci, S., Huang, K., Weil, Z., Bratasz, A., Wells, J., Powell, N.D., et al. (2013). Autonomic dysreflexia causes chronic immune suppression after spinal cord injury. J. Neurosci. *33*, 12970–12981. https://doi.org/10.1523/jneurosci.1974-13.2013.
79. Raju, D.V., and Smith, Y. (2006). Anterograde axonal tract tracing. Curr. Protoc. Neurosci. *Chapter 1*. Unit 1.14. https://doi.org/10.1002/0471142301.ns0114s37.
80. Paganin, D., Mayo, S.C., Gureyev, T.E., Miller, P.R., and Wilkins, S.W. (2002). Simultaneous phase and amplitude extraction from a single defocused image of a homogeneous object. J. Microsc. *206*, 33–40. https://doi.org/10.1046/j.1365-2818.2002.01010.x.
81. van Aarle, W., Palenstijn, W.J., Cant, J., Janssens, E., Bleichrodt, F., Dabravolski, A., De Beenhouwer, J., Joost Batenburg, K., and Sijbers, J. (2016). Fast and flexible X-ray tomography using the ASTRA toolbox. Opt. Express *24*, 25129–25147. https://doi.org/10.1364/oe.24.025129.
82. Vo, N.T., Drakopoulos, M., Atwood, R.C., and Reinhard, C. (2014). Reliable method for calculating the center of rotation in parallel-beam tomography. Opt. Express *22*, 19078–19086. https://doi.org/10.1364/oe.22.019078.
83. Wadeson, N., and Basham, M. (2016). Savu: a Python-based, MPI framework for simultaneous processing of multiple, N-dimensional, large tomography datasets. Preprint at arXiv.
84. Escalante, T., Franceschi, A., Rucavado, A., and Gutiérrez, J.M. (2000). Effectiveness of batimastat, a synthetic inhibitor of matrix metalloproteinases, in neutralizing local tissue damage induced by BaP1, a hemorrhagic metalloproteinase from the venom of the snake bothrops asper. Biochem. Pharmacol. *60*, 269–274. https://doi.org/10.1016/s0006-2952(00)00302-6.
85. Low, J.A., Johnson, M.D., Bone, E.A., and Dickson, R.B. (1996). The matrix metalloproteinase inhibitor batimastat (BB-94) retards human breast cancer solid tumor growth but not ascites formation in nude mice. Clin. Cancer Res. *2*, 1207–1214.
86. Zhu, Y., Lyapichev, K., Lee, D.H., Motti, D., Ferraro, N.M., Zhang, Y., Yahn, S., Soderblom, C., Zha, J., Bethea, J.R., et al. (2017). Macrophage transcriptional profile identifies lipid catabolic pathways that can be therapeutically targeted after spinal cord injury. J. Neurosci. *37*, 2362–2376. https://doi.org/10.1523/JNEUROSCI.2751-16.2017.
87. Chen, N., Zhou, P., Liu, X., Li, J., Wan, Y., Liu, S., and Wei, F. (2020). Overexpression of Rictor in the injured spinal cord promotes functional recovery in a rat model of spinal cord injury. FASEB J. *34*, 6984–6998. https://doi.org/10.1096/fj.201903171R.
88. Li, X., and Gao, T. (2014). mTORC2 phosphorylates protein kinase Cζ to regulate its stability and activity. EMBO Rep. *15*, 191–198. https://doi.org/10.1002/embr.201338119.
89. Knox, S.M., Lombaert, I.M.A., Haddox, C.L., Abrams, S.R., Cotrim, A., Wilson, A.J., and Hoffman, M.P. (2013). Parasympathetic stimulation improves epithelial organ regeneration. Nat. Commun. *4*, 1494. https://doi.org/10.1038/ncomms2493.
90. Sloan, E.K., Priceman, S.J., Cox, B.F., Yu, S., Pimentel, M.A., Tangkanangnukul, V., Arevalo, J.M.G., Morizono, K., Karanikolas, B.D. W., Wu, L., et al. (2010). The sympathetic nervous system induces a metastatic switch in primary breast cancer. Cancer Res. *70*, 7042–7052. https://doi.org/10.1158/0008-5472.Can-10-0522.

91. Mahmoud, A.I., O'Meara, C.C., Gemberling, M., Zhao, L., Bryant, D.M., Zheng, R., Gannon, J.B., Cai, L., Choi, W.Y., Egnaczyk, G.F., et al. (2015). Nerves Regulate Cardiomyocyte Proliferation and Heart Regeneration. Dev. Cell *34*, 387–399. https://doi.org/10.1016/j.devcel.2015.06.017.

92. Magnon, C., and Hondermarck, H. (2023). The neural addiction of cancer. Nat. Rev. Cancer *23*, 317–334. https://doi.org/10.1038/s41568-023-00556-8.

93. Cortese, N., Rigamonti, A., Mantovani, A., and Marchesi, F. (2020). The neuro-immune axis in cancer: Relevance of the peripheral nervous system to the disease. Immunol. Lett. *227*, 60–65. https://doi.org/10.1016/j.imlet.2020.07.010.

94. Cole, S.W., Nagaraja, A.S., Lutgendorf, S.K., Green, P.A., and Sood, A.K. (2015). Sympathetic nervous system regulation of the tumour microenvironment. Nat. Rev. Cancer *15*, 563–572. https://doi.org/10.1038/nrc3978.

95. Jayachandran, P., Battaglin, F., Strelez, C., Lenz, A., Algaze, S., Soni, S., Lo, J. H., Yang, Y., Millstein, J., Zhang, W., et al. (2023). Breast cancer and neurotransmitters: emerging insights on mechanisms and therapeutic directions. Oncogene *42*, 627–637. https://doi.org/10.1038/s41388-022-02584-4.

96. Renz, B.W., Tanaka, T., Sunagawa, M., Takahashi, R., Jiang, Z., Macchini, M., Dantes, Z., Valenti, G., White, R.A., Middelhoff, M.A., et al. (2018). Cholinergic Signaling via Muscarinic Receptors Directly and Indirectly Suppresses Pancreatic Tumorigenesis and Cancer Stemness. Cancer Discov. *8*, 1458–1473. https://doi.org/10.1158/2159-8290.Cd-18-0046.

97. Martín-Márquez, B.T., Sandoval-García, F., Corona-Meraz, F.I., Martínez-García, E.A., Sánchez-Hernández, P.E., Salazar-Páramo, M., Fletes-Rayas, A.L., González-Inostroz, D., and Vazquez-Del Mercado, M. (2023). Osteopontin: A Bone-Derived Protein Involved in Rheumatoid Arthritis and Osteoarthritis Immunopathology. Biomolecules *13*, 502. https://doi.org/10.3390/biom13030502.

98. Zhao, H., Chen, Q., Alam, A., Cui, J., Suen, K.C., Soo, A.P., Eguchi, S., Gu, J., and Ma, D. (2018). The role of osteopontin in the progression of solid organ tumour. Cell Death Dis. *9*, 356. https://doi.org/10.1038/s41419-018-0391-6.

99. Bill, R., Wirapati, P., Messemaker, M., Roh, W., Zitti, B., Duval, F., Kiss, M., Park, J.C., Saal, T.M., Hoelzl, J., et al. (2023). CXCL9:SPP1 macrophage polarity identifies a network of cellular programs that control human cancers. Science *381*, 515–524. https://doi.org/10.1126/science.ade2292.

100. Cortese, N., Carriero, R., Laghi, L., Mantovani, A., and Marchesi, F. (2020). Prognostic significance of tumor-associated macrophages: past, present and future. Semin. Immunol. *48*, 101408. https://doi.org/10.1016/j.smim.2020.101408.

101. Lê, H., Deforges, J., Cutolo, P., Lamarque, A., Hua, G., Lindner, V., Jain, S., Balloul, J.M., Benkirane-Jessel, N., and Quéméneur, E. (2024). Patient-derived tumoroids and proteomic signatures: tools for early drug discovery. Front. Immunol. *15*, 1379613. https://doi.org/10.3389/fimmu.2024.1379613.

102. Harris, A.L. (2002). Hypoxia–a key regulatory factor in tumour growth. Nat. Rev. Cancer *2*, 38–47. https://doi.org/10.1038/nrc704.

103. Ma, S.F., Chen, Y.J., Zhang, J.X., Shen, L., Wang, R., Zhou, J.S., Hu, J. G., and Lü, H.Z. (2015). Adoptive transfer of M2 macrophages promotes locomotor recovery in adult rats after spinal cord injury. Brain Behav. Immun. *45*, 157–170. https://doi.org/10.1016/j.bbi.2014.11.007.

104. Rapalino, O., Lazarov-Spiegler, O., Agranov, E., Velan, G.J., Yoles, E., Fraidakis, M., Solomon, A., Gepstein, R., Katz, A., Belkin, M., et al. (1998). Implantation of stimulated homologous macrophages results in partial recovery of paraplegic rats. Nat. Med. *4*, 814–821. https://doi.org/10.1038/nm0798-814.

105. Schwartz, M., Lazarov-Spiegler, O., Rapalino, O., Agranov, I., Velan, G., and Hadani, M. (1999). Potential repair of rat spinal cord injuries using stimulated homologous macrophages. ; discussion 1045. Neurosurgery *44*, 1041–1045. https://doi.org/10.1097/00006123-199905000-00057.

106. Baleviciute, A., and Talbot, S. (2025). Macrophages promote nerve growth in both tumours and spinal cord. Nat. Rev. Immunol. *25*, 318. https://doi.org/10.1038/s41577-025-01164-3.

107. Perez-Riverol, Y., Csordas, A., Bai, J., Bernal-Llinares, M., Hewapathirana, S., Kundu, D.J., Inuganti, A., Griss, J., Mayer, G., Eisenacher, M., et al. (2019). The PRIDE database and related tools and resources in 2019: improving support for quantification data. Nucleic Acids Res. *47*, D442–D450. https://doi.org/10.1093/nar/gky1106.

108. Delov, V., Muth-Köhne, E., Schäfers, C., and Fenske, M. (2014). Transgenic fluorescent zebrafish Tg(fli1:EGFP)^{y1} for the identification of vasotoxicity within the zFET. Aquat. Toxicol. *150*, 189–200. https://doi.org/10.1016/j.aquatox.2014.03.010.

109. Gaudenzi, G., Albertelli, M., Dicitore, A., Würth, R., Gatto, F., Barbieri, F., Cotelli, F., Florio, T., Ferone, D., Persani, L., et al. (2017). Patient-derived xenograft in zebrafish embryos: a new platform for translational research in neuroendocrine tumors. Endocrine *57*, 214–219. https://doi.org/10.1007/s12020-016-1048-9.

110. Lattante, S., de Calbiac, H., Le Ber, I., Brice, A., Ciura, S., and Kabashi, E. (2015). Sqstm1 knock-down causes a locomotor phenotype ameliorated by rapamycin in a zebrafish model of ALS/FTLD. Hum. Mol. Genet. *24*, 1682–1690. https://doi.org/10.1093/hmg/ddu580.

111. Kimmel, C.B., Ballard, W.W., Kimmel, S.R., Ullmann, B., and Schilling, T. F. (1995). Stages of embryonic development of the zebrafish. Dev. Dyn. *203*, 253–310. https://doi.org/10.1002/aja.1002030302.

112. Wehner, D., Tsarouchas, T.M., Michael, A., Haase, C., Weidinger, G., Reimer, M.M., Becker, T., and Becker, C.G. (2017). Wnt signaling controls pro-regenerative Collagen XII in functional spinal cord regeneration in zebrafish. Nat. Commun. *8*, 126. https://doi.org/10.1038/s41467-017-00143-0.

113. Encinas, M., Iglesias, M., Liu, Y., Wang, H., Muhaisen, A., Ceña, V., Gallego, C., and Comella, J.X. (2000). Sequential treatment of SH-SY5Y cells with retinoic acid and brain-derived neurotrophic factor gives rise to fully differentiated, neurotrophic factor-dependent, human neuron-like cells. J. Neurochem. *75*, 991–1003. https://doi.org/10.1046/j.1471-4159.2000.0750991.x.

114. Shipley, M.M., Mangold, C.A., and Szpara, M.L. (2016). Differentiation of the SH-SY5Y Human Neuroblastoma Cell Line. J. Vis. Exp. 53193. https://doi.org/10.3791/53193.

115. Hao, Y., Stuart, T., Kowalski, M.H., Choudhary, S., Hoffman, P., Hartman, A., Srivastava, A., Molla, G., Madad, S., Fernandez-Granda, C., et al. (2024). Dictionary learning for integrative, multimodal and scalable single-cell analysis. Nat. Biotechnol. *42*, 293–304. https://doi.org/10.1038/s41587-023-01767-y.

116. Aibar, S., González-Blas, C.B., Moerman, T., Huynh-Thu, V.A., Imrichova, H., Hulselmans, G., Rambow, F., Marine, J.-C., Geurts, P., Aerts, J., et al. (2017). SCENIC: single-cell regulatory network inference and clustering. Nat. Methods *14*, 1083–1086. https://doi.org/10.1038/nmeth.4463.

117. Grote, S. (2024). Gene ontology enrichment using FUNC. https://cdimage.debian.org/mirror/bioconductor.org/packages/release/bioc/manuals/GOfuncR/man/GOfuncR.pdf.

118. Solivan-Rivera, J., Yang Loureiro, Z., DeSouza, T., Desai, A., Pallat, S., Yang, Q., Rojas-Rodriguez, R., Ziegler, R., Skritakis, P., Joyce, S., et al. (2022). A neurogenic signature involving monoamine Oxidase-A controls human thermogenic adipose tissue development. eLife *11*, e78945. https://doi.org/10.7554/eLife.78945.

119. Zhang, D., Park, D., Zhong, Y., Lu, Y., Rycaj, K., Gong, S., Chen, X., Liu, X., Chao, H.P., Whitney, P., et al. (2016). Stem cell and neurogenic gene-expression profiles link prostate basal cells to aggressive prostate cancer. Nat. Commun. *7*, 10798. https://doi.org/10.1038/ncomms10798.

120. Liao, Y., Smyth, G.K., and Shi, W. (2014). featureCounts: an efficient general purpose program for assigning sequence reads to genomic features. Bioinformatics *30*, 923–930. https://doi.org/10.1093/bioinformatics/btt656.

121. Love, M.I., Huber, W., and Anders, S. (2014). Moderated estimation of fold change and dispersion for RNA-seq data with DESeq2. Genome Biol. *15*, 550. https://doi.org/10.1186/s13059-014-0550-8.

122. Hänzelmann, S., Castelo, R., and Guinney, J. (2013). GSVA: gene set variation analysis for microarray and RNA-seq data. BMC Bioinform. *14*, 7. https://doi.org/10.1186/1471-2105-14-7.

123. Hao, C., Lane, J., and Jiang, W.G. (2023). Osteopontin and Cancer: Insights into Its Role in Drug Resistance. Biomedicines *11*, 197. https://doi.org/10.3390/biomedicines11010197.

124. Guenzle, J., Akasaka, H., Joechle, K., Reichardt, W., Venkatasamy, A., Hoeppner, J., Hellerbrand, C., Fichtner-Feigl, S., and Lang, S.A. (2020). Pharmacological Inhibition of mTORC2 Reduces Migration and Metastasis in Melanoma. Int. J. Mol. Sci. *22*, 30. https://doi.org/10.3390/ijms22010030.

125. Wheeler, K.C., Jena, M.K., Pradhan, B.S., Nayak, N., Das, S., Hsu, C.D., Wheeler, D.S., Chen, K., and Nayak, N.R. (2018). VEGF may contribute to macrophage recruitment and M2 polarization in the decidua. PLoS One *13*, e0191040. https://doi.org/10.1371/journal.pone.0191040.

126. Bifari, F., Dolci, S., Bottani, E., Pino, A., Di Chio, M., Zorzin, S., Ragni, M., Zamfir, R.G., Brunetti, D., Bardelli, D., et al. (2020). Complete neural stem cell (NSC) neuronal differentiation requires a branched chain amino acids-induced persistent metabolic shift towards energy metabolism. Pharmacol. Res. *158*, 104863. https://doi.org/10.1016/j.phrs.2020.104863.

127. Kaegi, S., Schwab, M.E., Dietz, V., and Fouad, K. (2002). Electromyographic activity associated with spontaneous functional recovery after spinal cord injury in rats. Eur. J. Neurosci. *16*, 249–258. https://doi.org/10.1046/j.1460-9568.2002.02076.x.

128. Dolci, S., Pino, A., Berton, V., Gonzalez, P., Braga, A., Fumagalli, M., Bonfanti, E., Malpeli, G., Pari, F., Zorzin, S., et al. (2017). High Yield of Adult Oligodendrocyte Lineage Cells Obtained from Meningeal Biopsy. Front. Pharmacol. *8*, 703. https://doi.org/10.3389/fphar.2017.00703.

129. Lange, C., Turrero Garcia, M., Decimo, I., Bifari, F., Eelen, G., Quaegebeur, A., Boon, R., Zhao, H., Boeckx, B., Chang, J., et al. (2016). Relief of hypoxia by angiogenesis promotes neural stem cell differentiation by targeting glycolysis. EMBO J. *35*, 924–941. https://doi.org/10.15252/embj.201592372.

130. Paganin, D. (2006). Coherent X-ray imaging. In Coherent X-Rray Optics (Oxford University Press), pp. 228–340. https://doi.org/10.1093/acprof:oso/9780198567288.003.0004.

131. Schaffert, A., Karkossa, I., Ueberham, E., Schlichting, R., Walter, K., Arnold, J., Blüher, M., Heiker, J.T., Lehmann, J., Wabitsch, M., et al. (2022). Di-(2-ethylhexyl) phthalate substitutes accelerate human adipogenesis through PPARγ activation and cause oxidative stress and impaired metabolic homeostasis in mature adipocytes. Environ. Int. *164*, 107279. https://doi.org/10.1016/j.envint.2022.107279.

132. Hughes, C.S., Sorensen, P.H., and Morin, G.B. (2019). A Standardized and Reproducible Proteomics Protocol for Bottom-Up Quantitative Analysis of Protein Samples Using SP3 and Mass Spectrometry. Methods Mol. Biol. *1959*, 65–87. https://doi.org/10.1007/978-1-4939-9164-8_5.

133. Wang, Z., Karkossa, I., Großkopf, H., Rolle-Kampczyk, U., Hackermüller, J., von Bergen, M., and Schubert, K. (2021). Comparison of quantitation methods in proteomics to define relevant toxicological information on AhR activation of HepG2 cells by BaP. Toxicology *448*, 152652. https://doi.org/10.1016/j.tox.2020.152652.

134. Schmidt, J.R., Geurtzen, K., von Bergen, M., Schubert, K., and Knopf, F. (2019). Glucocorticoid Treatment Leads to Aberrant Ion and Macromolecular Transport in Regenerating Zebrafish Fins. Front. Endocrinol. (Lausanne) *10*, 674. https://doi.org/10.3389/fendo.2019.00674.

135. Friedrich, J.O., Adhikari, N.K.J., and Beyene, J. (2011). Ratio of means for analyzing continuous outcomes in meta-analysis performed as well as mean difference methods. J. Clin. Epidemiol. *64*, 556–564. https://doi.org/10.1016/j.jclinepi.2010.09.016.

STAR★METHODS

KEY RESOURCES TABLE

REAGENT or RESOURCE	SOURCE	IDENTIFIER
Antibodies		
Neurofilament 200	Sigma	Cat: N4142; RRID: AB477272
DAPI	Thermo Fisher Scientific	Cat: D-1306; RRID: AB_2629482
Peripherin	Millipore	Cat: AB1530; RRID: AB_90725
B3 Tubulin	Promega	Cat: G7121; RRID: AB_430874
CD68	Thermo Fisher Scientific	Cat: 14-0681-82; RRID: AB_2572857
GFAP	Abcam	Cat: AB53554; RRID: AB880202
NeuN	Millipore	Cat: MAB377; RRID: AB_2298772
CD31	BD Biosciences	Cat: 557355; RRID: AB_396660
Rictor	Invitrogen	Cat: ma5-15681; RRID: AB_10987411
SPP1	R&D Systems	Cat: IC14331A; RRID: AB_10920939
CD14	Epigenetek	Cat: A72619; RRID: AB_3674842
CD163	Genetex	Cat: GTX54458; RRID: AB_2887858
Iba1	Wako	Cat: 019-19741; RRID: AB_839504
Collagen 1	Abcam	Cat: AB34710; RRID: AB_731684
Collagen 3	Genetex	Cat: GTX26310; RRID: AB_385206
Fibronectin	Dako	Cat: A0245; RRID:
CD206	R&D Systems	Cat: AF2535; RRID: AB_2063012
vGlut	Synaptic system	Cat 135303; RRID: AB_887875
ChAT	Millipore	Cat: AB144P; RRID: AB_2079751
Casp3	Cell Signaling	Cat: 9661; RRID: AB_2341188
Goat anti-mouse Alexa Fluor 488	Thermo Fisher Scientific	Cat: A-11029; RRID: AB_2534088
Donkey anti-rabbit Alexa Fluor 546	Thermo Fisher Scientific	Cat: A10040; RRID: AB_2534016
Donkey anti-rat Alexa-Cy3	Jackson	Cat: 712-166-153; RRID: AB_2340669
Donkey anti-goat Alexa Fluor 488	Jackson	Cat: 705-546-147; RRID: AB_2340430
Donkey anti-goat Alexa Fluor 647	Thermo Fisher Scientific	Cat: A21447; RRID: AB_2535864
Donkey anti-mouse Alexa Fluor 488	Thermo Fisher Scientific	Cat: A32766; RRID: AB_2762823
Donkey anti-mouse Alexa Fluor 647	Thermo Fisher Scientific	Cat: A32787; RRID: AB_2762830
Donkey anti-rabbit Alexa Fluor 488	Thermo Fisher Scientific	Cat: A21206; RRID: AB_2535792
Donkey anti-rabbit Alexa Fluor 647	Thermo Fisher Scientific	Cat: A32795; RRID: AB_2762835
Goat anti-rat Alexa Fluor 488	Thermo Fisher Scientific	Cat: A11006; RRID: AB_2534074
Rictor	Abcam	Cat: ab70374; RRID: AB_2253794
Rho	Abcam	Cat: ab40673; RRID: AB_777706
TC10	Invitrogen	Cat: MA5-37999; RRID: AB_2897917
CD14, VioBlue REAfinity	Miltenyi Biotec	Cat: 130-110-524; RRID: AB_2655055
CD68, APC REAfinity	Miltenyi Biotec	Cat: 130-114-461; RRID: AB_2726643
CD163, APC-Vio770 REAfinity	Miltenyi Biotec	Cat: 130-112-131; RRID: AB_2655487
CD184 (CXCR4), VioBright FITC REAfinity	Miltenyi Biotec	Cat: 130-117-370; RRID: AB_2734060
HIF-1A, Alexa Fluor 647	BD Biosciences	Cat: 565924; RRID: AB_2739388
VEGFA, PE	Abcam	Cat: ab214424; RRID: AB_3064726
Osteopontin, APC	R&D Systems	Cat: AF1433; RRID: AB_354791
CD14, APC	eBiosciences	Cat: 17-0141-81; RRID: AB_469351
CD206, Alexa Fluor 647	BD Biosciences	Cat: 568808; RRID: AB_3094491
HLA-DR, APC-Cy7	BD Biosciences	Cat: 335831; RRID: AB_2868692

(*Continued on next page*)

Continued

REAGENT or RESOURCE	SOURCE	IDENTIFIER
Arg1	Kindly donated from collaborator	N/A
iNOS, FITC REAfinity	Myltenyi Biotec	Cat: 130-116-421; RRID: AB_2727525
Bacterial and virus strains		
pLV[shRNA]-EGFP:T2A:Puro-U6>mSPP1-shRNA	VectorBuilder	N/A
pLV[shRNA]-EGFP:T2A:Puro-U6>scramble-shRNA	VectorBuilder	N/A
pLV[shRNA]-EGFP:T2A:Puro- U6>mRictor	VectorBuilder	N/A
pLV[shRNA]-EGFP:T2A:Puro- U6>mScramble	VectorBuilder	N/A
AAV9-GFP-U6-mRICTOR-shRNA	Biolabs	N/A
AAV9-GFP-U6-scramble-shRNA	Biolabs	N/A
Biological samples		
Embryonic (E14.5) mouse neural stem cells	This paper	N/A
Dorsal root ganglia	This paper	N/A
IPSCs-derived motor neurons	This paper	N/A
Chemicals, peptides, and recombinant proteins		
Recombinant SPP1	R&D Stystems	Cat: 441-OP-050/CF
DMEM/F-12 GlutaMAX	Gibco	Cat: 31331-028
B27	Gibco	Cat: 17504-044
N2	Gibco	Cat: 17502-048
Penicillin/Streptomycin	Gibco	Cat: 15140-122
EGF	Peprotech	Cat: AF-100-15
bFGF	Preprotech	Cat: 100-18B
IMDM	Euroclone	Cat: ECB2072L
FBS	Euroclone	Cat: ECS0186L
L-glutamine	Gibco	Cat: 25030081
M-CSF	Miltenyi Biotec	Cat: 130101704
LPS	Sigma Aldrich	Cat: L4005-100MG
IFN-y	Sigma Aldrich	Cat: IF002
IL-4	Miltenyi Biotec	Cat: 130-093-920
Neurobasal Media	Gibco	Cat: 21103-049
StemPro Accutase Cell Dissociation Reagent	Gibco	Cat: A1105-01
Poly-lysine	Sigma-Aldrich	Cat: P6407
PFA	Mondial	Cat: FM0622
HBSS 10X	Gibco	Cat: 14180-046
Collagenase	Roche	Cat: 10103578001
Trypsin	Sigma-Aldrich	Cat: T4665
Parecoxib	TargetMol	Cat: T1780
Celecoxib	LKT Laboratories	Cat: 169590-42-5
Batimastat	Selleck Chemicals	Cat: S7155
RPMI	Gibco	Cat: 21870076
Lysis Buffer 17	R&D Systems	Cat: 895943
StemPro-34 medium	Thermo Fisher Scientific	Cat: 10639011
SCF	Peprotech	Cat: 300-07-14UG
FLT-3	Peprotech	Cat: 300-19-10UG
IL-3	Peprotech	Cat: 200-03-10UG
IL-6	Peprotech	Cat: 200-06-20UG
Rho-associated kinase inhibitor	Selleck Chemicals	Cat: Y27632
SB431542	Tocris	Cat: 1614
LDN193189	Sigma Aldrich	Cat: SML0559
Retinoic acid	Sigma Aldrich	Cat: R2500-25MG

(*Continued on next page*)

Continued

REAGENT or RESOURCE	SOURCE	IDENTIFIER
BDNF	Peprotech	Cat: 450-02
Laminin	Thermo Fisher Scientific	Cat: 23017015
GDNF	Peprotech	Cat: 450-10-10UG
CNTF	Peprotech	Cat: 450-13-20UG
DMEM	Gibco	Cat: 11965-092
GlutaMAX Supplement	Gibco	Cat: 35050061
Poly-D lysin	Merck	Cat: P6407-5MG
JRAB2011	MedCheExpress	Cat: HY-122022
BSA	Sigma Aldrich	Cat: A7906-10G
CXCL12	Sigma Aldrich	Cat: SRP3276-10UG
Coomassie Brilliant Blue R250	Sigma Aldrich	Cat: 1.12553
Seahorse XF DMEM medium	Seahorse Bioscience	Cat: 103575-100
Hematoxylin	Histo-Line	Cat: 01HEMH1000
Eosin	Histo-Line	Cat: 01EOY102500
Eukitt	Sigma Aldrich	Cat: 03989
Dextran Biotin 10000 MW Lysine Fixable (BDA)	Molecular Probes	Cat: D1956
Critical commercial assays		
Alexa Fluor 488 Tyramide SuperBoost Kit	Thermo Fisher	Cat: B40932
ELLA Mouse Immunoassay (Simple Plex Cartridge Kit)	Bio-Techne	Cat: SPCKA-MP-007736
Pierce BCA protein assay kit	Thermo Fisher Scientific	Cat: 23227
Proteome Profiler Human XL Cytokine Array Kit	R&D System	Cat: ARY022B
Fluo-4 Direct Calcium Assay Kit	Invitrogen	Cat: F10472
Multi Tissue Dissociation Kit	Miltenyi Biotec	Cat: 130-110-201
Zombie Yellow™ Fixable Viability Kit	BioLegend	Cat: 423103
DirectZOL RNA Miniprep kit (ZymoResearch)	Zymo Research	Cat: 2050
CytoTune iPS 2.0 Sendai Reprogrammin Kit	Thermo Fisher Scientific	Cat: A16517
Vectastain ABC-HRP kit	Vector Laboratories	Cat: PK-4000
GeneJET PCR Purification Kit	Thermo Fisher Scientific	Cat: K0702
DC Protein Assay	Bio-Rad	Cat: 5000111
CyQUANT cell proliferation assay kit	Thermo Fisher Scientifc	Cat: C35007
Transcription Factor Staining Buffer Set	Miltenyi Biotec	Cat: 130-122-981
Deposited data		
scRNA Human Glioblastoma	This paper	https://zenodo.org/record/6046299#.YgZ6bpbSKN4
Experimental models: Cell lines		
SH-SY5Y-N	ATCC	Cat: CRL-2266
U87	ATCC	Cat: HTB-14
MN/MCA1	MN-MCA1 sarcoma cells were kindly gifted by Professor Antonio Sica, Humanitas Clinical and Research Center, IRCSS, Milan, Italy.	N/A
Experimental models: Organisms/strains		
C57BL6/J	Envigo	Cat: 057
B6.Cg-Gt(ROSA)26Sor$^{tm9(CAG-tdTomato)Hze}$/J	Jackson Laboratory	Cat: 007909
Tg(-3.1neurog1:GFP)^{sb2}	KIT - European Zebrafish Resource Center (EZRC) - Fish	Cat: 15205
Oligonucleotides		
PTPRC	Applied Biosystem	Cat: Hs04189704_m1
CD14	Applied Biosystem	Cat: Hs02621496_s1
CD206	Applied Biosystem	Cat: Hs07288635_g1

(*Continued on next page*)

Continued

REAGENT or RESOURCE	SOURCE	IDENTIFIER
CXCR4	Applied Biosystem	Cat: Hs00607978_s1
GLUT1	Applied Biosystem	Cat: Hs00892681_m1
MT3A	Applied Biosystem	Cat: Hs02379661_g1
MT1X	Applied Biosystem	Cat: Hs00745167_s1
ANGPTL4	Applied Biosystem	Cat: Hs01101123_g1
SPP1	Applied Biosystem	Cat: Hs00959010_m1
Primer SPP1 forward: 5' – GCTTGGCTTATGGACTGAGGTC – 3'	Thermo Fisher Scientifc	N/A
Primer SPP1 reverse: 5' – CCTTAGACTCACCGCTCTTCATG– 3'	Thermo Fisher Scientifc	N/A
siRNA anti human SPP1	Qiagen	Cat: 1027416
siRNA anti human Scramble	Qiagen	Cat: 1027417
Software and algorithms		
Fiji (ImageJ)		RRID: SCR_002285
NIS-Element Basic Research		RRID: SCR_002776
GraphPad Prism		RRID: SCR_002798
Image Lab		RRID: SCR_014210
FlowJo		RRID: SCR_008520
Bcl2fastq		RRID: SCR_015058
STAR		RRID: SCR_004463
R studio		RRID: SCR_000432
Bioconductor		RRID: SCR_006442
DESeq2 package		RRID: SCR_015687
featureCounts		RRID: SCR_012919
GSVA		RRID: SCR_021058
Seurat package		RRID: SCR_016341
Other		
ScRNA of human glioblastoma and astrocytoma	This paper	https://zenodo.org/record/6046299#.YgZ6bpbSKN4
ScRNA of human pancreatic cancer	Oh et al.[15]	GSE231535
ScRNA of human breast cancer	Liu et al.[16]	GSE167036
ScRNA of human colorectal cancer	Hsu et al.[17]	GSE231559
BulkRNA sequencing of monocytes and TAM from human breast and endometrial cancer	Cassetta et al.[33]	GSE117970
BulkRNA sequencing of monocytes and TAM from mouse glioblastoma	Chen et al.[59]	PRJNA349180
Bulk RNA sequencing of monocytes, TAM, healthy and diseased microglia in mouse glioblastoma	Bowman et al.[32]	GSE86573
ScRNA of mouse sarcoma	Tessaro et al.[41]	GSE201615, GSE201618

EXPERIMENTAL MODEL AND STUDY PARTICIPANT DETAILS

Zebrafish model for TAM angiogenetic potency analysis

Zebrafish embryos were raised and maintained under standard conditions according to the national guidelines (D.Lgs 26/2014) under the institutional breeding authorization 0035597/23. Zebrafish embryos at 2 dpf of the Tg(*fli1a*:GFP)^{y1} line[108] were randomly divided into two experimental groups and then transplanted in the perivitelline region with 25 x 10^4 TAM or with dPBS as a control. Analyses were performed by counting the number and length of spikes in the subintestinal vessels using ImageJ software (USA National Institutes of Health, USA), as previously described.[109]

Murine sarcoma model

All experimental procedures were approved by the National Institute of Health (protocol N.949/2018-PR). 7-week-old C57BL/6 male mice were randomly assigned to each experimental group. To induce tumor formation, we utilized the 3-MCA-derived sarcoma cell line MN/MCA1,[39] which was kindly provided by Francesca Consonni.[42] MN/MCA1 cells were plated in a T75 flask in fresh RPMI supplemented with heat-inactivated FBS (10%), penicillin-streptomycin (1%), and L-Glutamine (1%) for 24 h. At the specific experimental time-point (days 0 and 14), MN/MCA1 cells were washed with PBS, detached with trypsin, resuspended in fresh sterile PBS, and injected intramuscularly in the left hindlimb of C57BL/6 male mice. On day 0, control mice (CTRL) received 1 injection (100 μl/injection) of cell suspension (MN/MCA1 cells, 10^5 cells/mouse), TAM-treated mice received a combination of MN/MCA1 cells (10^5 cells/mouse) and TAM (5 x 10^5 cells/mouse, TAM-treated mice), or a combination of MN/MCA1 cells (10^5 cells/mouse) and $TAM^{LVScramble}$ (5 x 10^5 cells/mouse, $TAM^{LVScramble}$-treated mice), or a combination of MN/MCA1 cells (10^5 cells/mouse) and $TAM^{LV\ Spp1\text{-}KD}$ (5 x 10^5 cells/mouse, $TAM^{LV\ Spp1\text{-}KD}$-treated mice). On day 14, TAM-treated mice received a second injection (100 μl/injection) of TAM suspension (5 x 10^5 cells/mouse), $TAM^{LVScramble}$-treated mice received a second injection (100 μl/injection) of $TAM^{LVScramble}$ suspension (5 x 10^5 cells/mouse), and $TAM^{LV\ Spp1\text{-}KD}$-treated mice received a second injection (100 μl/injection) of $TAM^{LV\ Spp1\text{-}KD}$ suspension (5 x 10^5 cells/mouse). On day 21, the mice were sacrificed, and the tumor masses were freshly dissected and post-fixed overnight in 4% PFA and 4% sucrose. The samples were then stored in 30% sucrose at 4°C for further analysis.

Zebrafish transection spinal cord injury model

Zebrafish embryos were raised and maintained under standard conditions according to the national guidelines (D.Lgs 26/2014) under the institutional breeding authorization 0035597/23. Two days post fertilization (2 dpf) zebrafish embryos from the Tg(-3.1*neurog1*:GFP)^{sb2110} were collected, staged according to the reference guidelines[111] and raised at 28°C in E3 medium fish water. Before manipulations, embryos were dechorionated and anesthetized. Zebrafish embryos were randomly divided into two groups, anesthetized, and the spinal cord was transected at the 10th spinal segment level, as previously reported.[112] 25 x 10^4 ^{tdTomato}TAM (injured-+TAM) or dPBS (injured) were transplanted directly into the region of the spinal cord injury and placed in a 24-well plate, 1 embryo per well. For each embryo, the extension of the lesion at 1 and 2 days post injury (dpi) was measured using the Image-J software (USA National Institutes of Health, USA).

Severe complete contusive compressive SCI (scSCI) mouse model

All procedures on mice were approved by the National Institute of Health (protocol N.750/2019-PR) and by the Animal Ethics Committee of the University of Verona (CIRSAL, Centro Interdipartimentale di Servizio alla Ricerca Sperimentale). To maintain the colony of tdTomato mice in accordance with the 3R principle, we preferred to isolate tdTomato monocytes from male mice; therefore, we chose to injure and subsequently transplant only male mice. scSCI was performed as described previously.[64] Briefly, 7-week-old male C57BL/6 mice were anesthetized and underwent a laminectomy at the thoracic 11 (T11) vertebra. Then, by using a MASCIS Impactor, a 5g rod was dropped from a height of 6.25mm and left in compression for 11s. Subcutaneous injections of Baytril (10 mg/Kg) and Altadol (2mg/Kg) were provided. Animals were caged individually, and animal care was performed daily untill the end of the experiment. Animals showing a BBB score <= 1 at 1 day post injury were divided into groups, ensuring a comparable average BBB score across the groups.

Murine mouse model for TAM-safety assessment

All procedures on mice were approved by the National Institute of Health (protocol N.750/2019-PR) and by the Animal Ethics Committee of the University of Verona (CIRSAL, Centro Interdipartimentale di Servizio alla Ricerca Sperimentale). For the preclinical long-term assessment, healthy 7-week-old male and female C57BL/6 mice underwent laminectomy at the T11 vertebra level and received 4 injections (1 μl/injection) of TAM (0.5 x 10^6 cells/μl), or saline solution in 4 points spaced 2 mm apart (0.5 mm depth), centered on the spinal segment under the removed T11 vertebra.

Murine monocyte isolation

All procedures on mice were approved by the National Institute of Health (protocol N.750/2019-PR) and by the Animal Ethics Committee of the University of Verona (CIRSAL, Centro Interdipartimentale di Servizio alla Ricerca Sperimentale). Murine bone marrow-derived monocytes were extracted from 8–12-week-old male B6.Cg-Gt(ROSA)26Sor$^{tm9(CAG\text{-}tdTomato)Hze}$/J or C57BL/6 mice.

Generation of human induced pluripotent stem cells (iPSCs)

iPSCs were generated as previously described by Bossolasco and colleagues,[44] by reprogramming skin biopsy-derived fibroblasts or peripheral blood mononuclear cells (PBMCs) from 3 healthy donors. Briefly, fibroblasts were seeded in a well of a 6-well plate in specific fibroblast medium and PBMC isolated from peripheral blood samples were seeded on 24-well plate in StemPro-34 medium (Thermo Fisher Scientific) supplemented with SCF (100 ng/ml; Peprotech), FLT-3 (100 ng/ml; Peprotech), IL-3 (20 ng/ml; Peprotech), and IL-6 (20 ng/ml; Peprotech) cytokines with daily medium changes and fresh cytokines addition. After 4 days, transduction was performed using CytoTune-iPS 2.0 Sendai Reprogramming Kit (Thermo Fisher Scientific). 3–7 days later, reprogrammed fibroblasts and PBMCs were plated onto Matrigel-coated dishes and thereafter monitored for the emergence of iPSC colonies. Colonies passed using an EDTA solution (0.5 μM), were expanded in Essential 8 medium for at least 6 passages before being characterized and differentiated.

Motor neuron (MN) differentiation from iPSCs

iPSCs were allowed to grow in suspension in HuES medium supplemented with basic FGF (20 ng/ml; Peprotech) and Rho-associated kinase (ROCK) inhibitor Y27632 (20 μM; Selleckchem) to obtain embryoid bodies (EBs). The third day, SB431542 (10 μM, Tocris) and LDN193189 (0.2 μM, Sigma-Aldrich) were added to the cultures to induce neuralization. On day 4, neural induction of EBs was performed using DMEM/F12 supplemented with L-glutamine (2 mM), penicillin (10 U/ml), streptomycin (10 μg/ml), MEM NEAA (0.1 mM), heparin (2 μg/ml; Sigma-Aldrich), N2 supplement (1%, Thermo Fisher Scientific), ROCK inhibitor (20 μM), ascorbic acid (AA, 0.4 μg/ml, Sigma-Aldrich), retinoic acid (RA, 1 μM; Sigma-Aldrich), brain-derived neurotrophic factor (BDNF, 10 ng/ml; Peprotech). SB431542 and LDN193189 were added until day 7 when cultures were supplemented with 1 μM smoothened agonist (SAG; Merck) and 0.5 μM purmorphamine (Pur; Sigma-Aldrich). For 10 days the medium was changed every alternate day. On day 17, EBs were dissociated with 0.05% trypsin (Sigma-Aldrich) and plated on poly-lysine (Sigma-Aldrich)/laminin (Thermo Fisher Scientific)-coated coverslips on 24-well plates at a concentration of 15 x 10^3 cells/well. Cells were cultured in neural differentiation medium (Neurobasal, Thermo Fisher Scientific), L-glutamine (2mM), penicillin (10U/ml), streptomycin (10μg/ml), MEM NEAA (0.1mM), N2 supplement (1%), B27 (2%; Thermo Fisher Scientific), laminin (Lam; 1 μg/ml), glutamate (Glu; 25 μM; Sigma-Aldrich), ascorbic acid (0.4 μg/ml), glial-derived neurotrophic factor (GDNF, 10 ng/ml) and ciliary neurotrophic factor (CNTF, 10 ng/ml) (both from Peprotech). MNs were allowed to differentiate for 10 days and finally co-cultured with macrophages.

Isolation of single cell neurons from mouse dorsal root ganglia (DRG)

All procedures on mice were approved by the National Institute of Health (protocol N.750/2019-PR) and by the Animal Ethics Committee of the University of Verona (CIRSAL, Centro Interdipartimentale di Servizio alla Ricerca Sperimentale). DRG were dissected from 8–12-week-old male C57BL/6 mice, and placed on a Petri dish containing fresh HBSS, centrifuged at 1300 rcf, and cultured at 37°C, 5% CO_2, for 5 days into a 12-well plate in DRG medium composed of Neurobasal Medium-L-Glutamine (Gibco), supplemented with heat-inactivated FBS (10%, Lonza), B27 (2%, Gibco), penicillin-streptomycin-fungizone (1%; Lonza), and Glutamine 100x (0.5 mM; Gibco). DRG were then mechanically dissociated with collagenase (1%; Roche) and trypsin (0.25%; Sigma-Aldrich), filtered, and cultured into a poly-lysine-coated 12-well plate in DRG Medium supplemented with NGF (50 μg/ml, DBA). Single-cell neurons derived from DRG were seeded at a concentration of 4 × 10^4 cells/well in a 24-well plate for 72 h, and they were allowed to differentiate for 5 days.

Mouse neural stem cells (mNSCs) isolation

All procedures on mice were approved by the National Institute of Health (protocol N.750/2019-PR) and by the Animal Ethics Committee of the University of Verona (CIRSAL, Centro Interdipartimentale di Servizio alla Ricerca Sperimentale). Neural stem cells (mNSCs) were extracted from E 14.5 C57BL6/J male and female mouse brain and maintained in culture as previously described.[47] Briefly, neurospheres were dissociated with StemPro™ Accutase™ Cell Dissociation Reagent (Gibco) and plated on poly-lysine (Sigma-Aldrich)-coated coverslips on 24-well plates at a concentration of 4 x 10^4 cells/well and cultured at 37°C, 5% CO_2, with DMEM/F-12 GlutaMAX (Gibco) supplemented with B27 (2%; Gibco), N2 (1%; Gibco), penicillin/streptomycin (1%; Gibco) enriched with 20 ng/ml EGF and 20 ng/ml bFGF.

Organoid generation and processing

Brain organoids were generated as previously described.[47] Briefly, E14.5 murine brain neural stem cells (NSCs) were extracted and maintained for 14 days in agitation using the ORBi-SHAKER CO_2 (Benchmark Scientific) within a humidified 5% CO_2 in air atmosphere at 37°C. To generate control organoids (Org-CTRL) and organoids co-cultured with TAM (Org+TAM) or M2 macrophages (Org+M2), on day 0, 4 x 10^4 NSCs/well or 4 x 10^4 NSCs/well added to 1 x 10^4 TAM/M2 macrophages were seeded into each well of 24-well plates (Thermo Fisher Scientific) in 500 μl of DMEM/F-12 GlutaMAX medium supplemented with B27 (2%; GIBCO), N2 (1%; GIBCO), penicillin/streptomycin (1%; GIBCO) enriched with 20 ng/ml EGF and 20 ng/ml bFGF.

Differentiation of the SH-SY5Y Human Neuroblastoma cell line

SH-SY5Y cells (ATCC, CRL-2266) were differentiated and cultured using a combination of previously reported protocols.[113,114] Briefly, undifferentiated cells were maintained in basic growth medium, comprised of Dulbecco's Modified Eagle's Medium (DMEM) (Gibco Life Technologies), supplemented with 10% heat-inactivated fetal bovine serum (hiFBS) (Gibco Life Technologies), GlutaMAX Supplement (Gibco Life Technologies), and 1X penicillin/streptomycin (Gibco Life Technologies). To induce differentiation, cells were grown in T25 flasks at a density of 5 x 10^5/flask with Neurobasal-A media (Gibco Life Technologies) supplemented with 1X B27 (Gibco Life Technologies), GlutaMAX Supplement (Gibco Life Technologies), and 1X penicillin/streptomycin and Retinoic Acid all trans (RA) (10 μM; Med Chem) for an additional 20 days. On day 21 (DIV 21), induced cells were enzymatically detached and seeded onto poly-D-lysine (0.5 mg/ml; Merck) and Laminin-coated (1:200 dilution; Merck) glass coverslips (12 mm^2) at a density of 50,000/coverslip. The following day, the medium was changed to Neurobasal-A media (Gibco Life Technologies) supplemented with BDNF (50 ng/mL; Peprotech), potassium chloride (20 mM; Sigma), 1X B27 (Gibco Life Technologies), GlutaMAX Supplement (Gibco Life Technologies), and 1X penicillin/streptomycin and RA for an additional 4 days. Cultivated cells were maintained at passage below 12 at 37°C and 5% CO_2.

Human monocyte isolation

All human studies were approved by the Ethical Committee (Comitato Etico Indipendente, IRCCS Istituto Clinico Humanitas, protocol N.6b2b3.n.1ch). Ethical clearance for the use of human subjects were obtained from the designated health facility (Comitato Etico Indipendente, IRCCS Istituto Clinico Humanitas). Written informed consent was obtained from each person after receiving information about use of their tissue samples. Mononuclear cells were freshly isolated from a leukocyte concentrate (buffy coat) collected from healthy donor volunteers enrolled at the Hematology Unit of the Humanitas Research Hospital, Rozzano, Milan, Italy. The biological material was anonymized.

METHOD DETAILS

Single-cell RNA bioinformatic analysis

On the 32.882 single-cell transcriptomes obtained from human glioblastoma (GBM), astrocytoma IDH+/+ or mutated IDH-/- tumor regions, and the adjacent healthy area, the Seurat 5.0.1 scRNA-Seq standard pipeline[115] was used to produce uniform approximation and projection (UMAP) plots. Raw data from human pancreatic, breast, and colorectal cancers, and data from mouse sarcoma were analyzed using the standard pipeline from Seurat 5.0.1. Gene marker expression across the different scRNA datasets was analyzed using the FeaturePlot function. Differential gene expression analysis for the extraction of the TAM's DEGs was performed via the FindMarkers function. The AUCell package[116] and pipeline were used to analyze the enriched genes included in the *neural growth* list. For microglia analysis, starting from the same dataset, we isolated TGFBI$^-$/TMEM119$^+$ microglia and TGFBI$^+$/TMEM119$^-$ TAM.

Neural growth gene list definition

Differentially expressed genes (DEGs) of TAMs were identified using Seurat's FindMarkers function[115] from the comparison between the TAM cluster (CD163$^+$/TGFBI$^+$) and the CD14$^-$/TMEM119$^-$ clusters included in the GBM, astrocytoma, and adjacent healthy tissue dataset. Enrichment analysis was then performed on these genes via the go_enrich function of the GOfuncR package.[117] To describe this finding, in accordance with previous studies,[19,26,118,119] we first include all the DEGs of the TAM cluster in the GBM datasets composing the selected GOs.[117] From the selected GOs and the DEGs, we obtain a list of 152 genes. We then refined this list by including only genes related to the cell secretome and itemized in the SEcreted Protein DataBase (SEPDB),[22] which resulted in a reduction of the list to 107 genes. We further manually refined this list to include only genes with well-established roles in neural growth-related functions, resulting in a list of 23 neural growth genes.

Cell sorting from mouse spinal cord tissue

Briefly, 0.5 cm scSCI mouse spinal cords centered on the lesion site were dissected and collected in tubes. The dissected spinal cord tissues were washed in ice-cold PBS 1X, resuspended in PBS 1X containing enzyme A, enzyme R, and enzyme D (Multi Tissue Dissociation Kits, Miltenyi Biotec), and dissociated using the gentleMACS™ Dissociator (Miltenyi Biotec) for 45 min (37C_Multi_F program). After dissociation, samples were centrifuged and TAM were enriched using the Percoll-density gradient method. Then, TAM were isolated using a FACS cell sorter (BD Fusion, Becton, Dickinson) with the fluorescent dye Zombie Yellow (BioLegend) as a viability marker. Throughout all phases of the protocol, the samples were kept on ice.

Mouse macrophage RNA sequencing and analysis

The total RNA from M2 and TAM mouse samples was isolated using the DirectZOL RNA Miniprep kit (ZymoResearch) according to the manufacturer's instructions. Quantification and quality check (RNA integrity number RIN>7) were assessed by using the Qubit4 (Invitrogen) instrument. Library preparation and processing were performed using the SMARTer total stranded RNA-Seq kit. All samples were sequenced in paired-end mode with the Illumina NextSeq 550 (sequencing kit: NextSeq 500/550 High Output v2.5 Kit, 150 cycles). The bcl2fastq v2.20.0.422 tool was used to demultiplex samples and generate FASTQ files from base call (BCL) files. The quality of the fastq files was checked with fastQC version 0.11.8. Mapping and sorting were done with the STAR v.2.7.3a tool. The reference genome used was GRCm38 v.M23. BAM files were checked with the RSeQC v.3.0.1 quality control package. The count matrix was generated with feature Counts.[120] Other RNA-Seq data were collected from the SRA database described in Chen et al.[34] and Bowman et al.,[32] which were selected since they consist of monocytes and TAM samples free from any therapy or drug, induced gene expression, or gene knockdown. Both datasets were then aligned to the same reference mouse genome. The count data were then subjected to DEGs analysis using the DESeq2 package.[121] Reads with low expression values were discarded. The considered DEGs are the ones with a significant p-value (<0.05). The gene set variation analysis was performed using the GSVA package,[122] and boxplots were generated with the ggpubr package. The statistical analysis comparing the different samples was conducted using a Student's t-test. Gene ontology analysis was performed with the go_enrich analysis of the GOfuncR package.[117]

Bioinformatic analysis of proteomic mouse gene datasets

Principal Component Analysis (PCA) was performed using the DESeq2 R library with Variance-Stabilizing Transformation data. Genes were filtered by expression with the filterByExpr function. Finally, the count matrix was normalized, resulting in a cpm (counts per million) matrix. Gene ontology analyses were performed via the go_enrich function of the GOfuncR package. The glmQLFit model

was adopted, and p-values were adjusted with the Benjamini-Hochberg correction. Differentially expressed genes (FDR $\leq$ 0.05, | log2FC| $\geq$ 1) were subsequently filtered based on both Gene Ontology and IPA annotation (Qiagen Ingenuity Pathway Analysis, v01–13) to define the receptorome and secretome gene lists. In particular, genes were selected if at least they were classified in one of the following categories: GO:0005576: extracellular region; GO:0005615: extracellular space; GO:0009986: cell surface; GO:0031012: extracellular matrix; GO:0005886: plasma membrane; GO:0016020: membrane; GO:0005125: cytokine activity; GO:0008083: growth factor activity; IPA: extracellular space; IPA: plasma membrane. Gene Ontology annotations were performed in R with AnnotationDbi v.1.44.0 and org.Mm.eg.dbv.3.7.0 packages. Up (and down) "exclusive" genes were listed considering the intersections of only up (or down) regulated genes in the TAM pre vs. M2 pre and TAM pre vs. TAM post differential analyses (genes). Furthermore, "exclusive" up (and down) regulated gene lists in TAM samples were functionally analyzed (gProfiler2 v.0.1.9 and msigdbr v.7.1.1 packages), and results were shown in bar plots.

Human macrophage RNA sequencing and analysis

For the *in vitro* M2-like macrophage and TAM human samples, total RNA was isolated using DirectZOL RNA Miniprep kit (ZymoResearch) according to the manufacturer's instructions. Quantification and quality check (RNA integrity number RIN>7) were assessed by using the Qubit4 (Invitrogen) instrument. Library preparation and processing were performed using the SMARTer total stranded RNA-Seq kit. All samples were sequenced in paired-end mode with the Illumina NextSeq 550 (sequencing kit: NextSeq 500/550 High Output v2.5 Kit, 150 cycles). The FASTQ files were then aligned with the reference genome GRCh38.p13. The count matrix was generated with feature Counts.[120] Data on monocytes and TAM from breast and endometrial cancer described in Cassetta et al.[33] were already available as gene counts. Principal Component Analysis (PCA) was performed using the DESeq2 R library[121] with Variance-Stabilizing Transformation data. Genes were filtered by expression with the filterByExpr function. The count data were then subjected to DEG analysis using the DESeq2 package. Reads with low expression values were discarded. The considered DEGs are the ones with a significant p-value (<0.05). The gene set variation analysis was performed using the GSVA package,[122] and boxplots were generated with the ggpubr package. The statistical analysis comparing the different samples was conducted using a Student's t-test. Gene ontology analysis was performed with the go_enrich analysis of the GOfuncR package.[117]

Murine bone marrow-derived macrophage (BMDM) generation and polarization

BMDMs were generated from 8–12-week-old male B6.Cg-*Gt(ROSA)26Sor*$^{tm9(CAG\text{-}tdTomato)Hze}$/J or C57BL/6 mice. Briefly, after flushing femurs, cells were differentiated in Iscove's Modified Dulbecco's Medium (IMDM Euroclone) supplemented with heat-inactivated FBS (10%, Euroclone), penicillin/streptomycin (100 U/mL, Gibco), L-glutamine (2 mM, Gibco) and M-CSF (100 ng/ml, Miltenyi Biotec) for 7 days. To differentiate them in TAMs, BMDM were cultivated in tumor conditioned medium (TCM) and IMDM (1:1) and placed in hypoxia (1% O_2) for 16–18 h at 37°C, 5%CO_2. M1 macrophages were generated by conditioning BMDM with 100 ng/mL of LPS and 20 ng/mL of IFN-γ for 16–18 h at 37°C, 5%CO_2. M2-like macrophages were generated by conditioning BMDM with IL-4 (20 ng/ml; Miltenyi Biotec) for 16–18 h at 37°C, 5% CO_2.

Tumor conditioned medium (TCM) for TAM polarization

10-week-old C57BL/6 mice were injected intramuscularly in the left limb with 1 x 10^5 MN-MCA1 cells. On day 21, the animals were sacrificed, and the tumors were harvested and digested in 0.125% endotoxin-free trypsin at 37°C for 40min. Tumor-derived cells were filtered and plated in RPMI 1640 (Lonza) supplemented with 10% heat-inactivated FBS, 100 U/ml penicillin-streptomycin, and 2 mM L-glutamine. The cell-free supernatant was collected after 16h and used for the polarization of murine TAM.

For human TAM polarization, TCM was obtained from the supernatant of GBM cell line U87 (ATCC), cultured with DMEM GlutaMAX (Gibco), supplemented with 10% heat-inactivated FBS (10%), 100 U/ml penicillin-streptomycin, collected after 18 h of culture at 37°C, 5% CO_2, and 80% cell confluence.

TAM conditioned medium (TAM-CM) generation for iPSCs-derived MN and SH-SY5Y polarization

Conditioned medium from human TAMs (hTAMs) or mouse TAMs (mTAMs) was added as 50% of the final medium of differentiation for 48 h to iPSC-derived MNs or SH-SY5Y differentiated neuronal culture. On TAM polarization's day 7, media was removed and fresh Neurobasal-A media (Gibco Life Technologies) supplemented with 1X B27 (Gibco Life Technologies), GlutaMAX Supplement (Gibco Life Technologies), and 1X penicillin/streptomycin was added on both hTAMs or mTAMs for an additional 24 h (TAM-CM) at 37°C, 5% CO_2. After 24 h, the medium was aspirated and filtered through a 0.22 μm filter, and then stored until use.

Co-culture of mouse neural stem cells (mNSCs) and mouse TAMs

After 2 days in culture media, 15 $\times$ 10^3 mouse TAMs (+TAM) cells were added to each well of culture for 48 h. Cells were then fixed in 4% PFA (Mondial), 4% sucrose, and left in PBS 1X at 4°C for subsequent immunostaining analysis.

Co-culture of mouse single cell neurons isolated from murine DRG and mouse M2 and TAM

Mouse single-cell neurons isolated from DRG were co-cultured, with 15 $\times$ 10^3 mouse M2-like macrophages (+M2) or TAMs (+TAM) added in each well. After 5 days of co-culture (37°C, 5% CO_2), the cells were fixed in 4% PFA (Mondial) and 4% sucrose, and then left in PBS 1X at 4°C for subsequent immunostaining analysis.

TAM^{LVScramble} and TAM$^{LV\ SPP1\text{-}KD}$ generation and co-cultures with mNSCs

BMDM were differentiated in Iscove's Modified Dulbecco's Medium (IMDM) supplemented with heat-inactivated FBS (10%, Lonza), penicillin/streptomycin (100 U/mL; Lonza), L-glutamine (2 mM; Lonza), and M-CSF (100 ng/ml; Miltenyi Biotec) for 7 days. Cells were then transduced with a multiplicity of infection (MOI) of 10 with pLV[shRNA]-EGFP:T2A:Puro-U6>mSPP1-shRNA (VectorBuilder) or pLV[shRNA]-EGFP:T2A:Puro-U6>scramble-shRNA (VectorBuilder). The transduction efficiency was ~65%, with a cell vitality ~98%. Increasing the MOI beyond 10, resulted in reduced cell viability. The virus-containing medium from infected cells was removed 12 h post-infection, TCM was added, and the cultures were placed in hypoxia (1% O2) for 16–18 h at 37°C, 5% CO_2, to obtain TAM$^{LV\ Spp1\text{-}KD}$ or TAM^{LVScramble}. Co-cultures were performed by adding 15 × 10^3 of mouse TAM$^{LV\ Spp1\text{-}KD}$ or TAM^{LVScramble} to 4 × 10^4 mNSCs on poly-lysine (Sigma-Aldrich)-coated coverslips on 24-well plates. After 2 days, cells were fixed in 4% PFA (Mondial), 4% sucrose, and left in PBS 1X at 4°C for subsequent immunostaining analysis.

SPP1 inhibition in mNSCs and mouse TAM co-culture (Parecoxib)

We used SPP1 inhibitor Parecoxib (TargetMol) at 163 μM,[123] a concentration that did not affect the TAM secretion of other neurotrophins (no changes in NGF and GDNF gene expression between TAM and TAM+Parecoxib; p=ns). Spp1 was added to 4 × 10^4 mNSC co-cultured with 15 × 10^3 mouse TAMs (+TAM+Parecoxib). The solvent of Parecoxib, DMSO, was added to 4 × 10^4 control mNSCs (CTRL) and mNSCs co-cultured with 15 × 10^3 mouse TAMs (+TAM). After 2 days, cells were fixed in 4% PFA (Mondial) and 4% sucrose, and then left in PBS 1X at 4°C for subsequent immunostaining analysis.

COX2 inhibition in mNSC and mouse TAM co-culture (Celecoxib)

COX-2 inhibitor Celecoxib (25 μl/ml, LKT Laboratories) was added to 4 × 10^4 control mNSCs (CTRL) and to mNSCs co-cultured with 15 × 10^3 mouse TAMs (+TAM+Celecoxib). After 2 days, cells were fixed in 4% PFA (Mondial), 4% sucrose, and left in PBS 1X at 4°C for subsequent immunostaining analysis.

Recombinant SPP1 in mNSCs

Recombinant SPP1 (0.06 ng/ml or 3 ng/ml or 0.1ug/ml, Thermo Fisher Scientific) was added to 4 x 10^4 control mNSCs (+rSPP1). After 2 days, cells were fixed in 4% PFA (Mondial) and 4% sucrose, and then left in PBS 1X at 4°C for subsequent immunostaining analysis. The concentration applied to the monocultures was determined according to the results of the ELISA assay (approximately 3 ng/ml by 5 × 10^4 TAM).

Recombinant SPP1 in iPSCs-MNs and SH-SY5Y-N

Recombinant SPP1 was added to 10 × 10^4 control in vitro iPSCs-MN (+rSPP1, 0.6 ng/ml, Thermo Fisher Scientific) or to 5 × 10^4 SH-SY5Y-N (+rSPP1, 0.3 ng/ml, Thermo Fisher Scientific). After 2 days, cells were fixed in 4% PFA (Mondial), 4% sucrose, and left in PBS 1X at 4°C for subsequent immunostaining analysis. The concentration applied to the mono cultures was determined according to the results of the ELISA assay (approximately 3ng/ml by 5 × 10^4 TAM).

Metalloproteinase inhibition in mNSC and mouse TAM co-culture (Batimastat)

Metalloproteinase inhibitor Batimastat (5 μM, Sellek Chemicals) was added to 4 × 10^4 to mNSC co-cultured with 1 × 10^4 mouse TAMs (+TAM+Batimastat). After 2 days, cells were fixed in 4% PFA (Mondial), 4% sucrose, and left in PBS 1X at 4°C for subsequent immunostaining analysis.

Metalloproteinase inhibition in iPSCs TAM co-culture (Batimastat)

Metalloproteinase inhibitor Batimastat (5 μM, SellekChemicals) was added to 10 × 10^4 control in vitro iPSCs-MN or to 5 × 10^4 SH-SY5Y-N. After 2 days, cells were fixed in 4% PFA (Mondial), 4% sucrose, and left in PBS 1X at 4°C for subsequent immunostaining analysis. Respectively, iPSCs-MN and SH-SY5Y-N cells cultured with 5 μM of Batimastat were used as an internal normalizing control.

NSC$^{LV\ Scramble}$ and NSC$^{LV\ Rictor\text{-}KD}$ generation and TAM co-culture

mNSCs were transduced with a (MOI) of 2.5 with pLV[shRNA]-EGFP:T2A:Puro- U6>mRictor (VectorBuilder) or pLV[shRNA]-EGFP:T2A:Puro- U6>mScram ble (VectorBuilder). The virus-containing medium from infected cells was removed 12 h post-infection. Co-culture was performed by adding to 4 x 10^4 NSC^{LVScramble} or NSC$^{LV\ Rictor\text{-}KD}$, 15 x 10^3 of mouse TAMs on poly-lysine (Sigma-Aldrich)-coated coverslips on 24-well plates. After 2 days, cells were fixed in 4% PFA (Mondial), 4% sucrose, and left in PBS 1X at 4°C for subsequent immunostaining analysis.

ELLA Mouse Immunoassay

TAMs were generated and polarized *in vitro* for 7 days as described above. Culturing supernatant was replaced with test media 24h prior to the experiment to avoid any confusion from exogenous proteins. The supernatant was then collected and processed for ELLA microfluidic immunoassay. 50 μl of supernatant was diluted 1:1 with sample diluent; the resulting solution was then added to the sample inlet of the ELLA cartridge, in accordance with the manufacturer's instructions. Wash buffer was added to the appropriate wells on

the ELLA cartridge. Sample results were reported using Simple Plex Runner v.3.7.2.0 (ProteinSimple) and were available approximately 90 min after initiation of the run. The experiment was conducted on 3 different supernatant collections.

Human monocyte-derived macrophage polarizations

The monocyte population was enriched by positive selection of CD14-labeled target cells using a human magnetic antibody cell sorting (MACS) system (Miltenyi Biotec), according to the manufacturer's procedure. Collected monocytes were centrifuged at 1250 RPM for 5min, supernatant discarded, and cells plated in a Petri dish in different conditions according to the polarization. M1-like macrophage polarization were incubated at 37°C, 5% CO_2 for 1 week in RPMI + FBS (10%) + M-CSF (100 ng/ml) and 100ng/ml of LPS (Sigma Aldrich) for 16 h. M2-like macrophages were incubated at 37°C, 5% CO_2 for 1 week in RPMI + FBS (10%) + M-CSF (100 ng/ml) and IL-4 (20 ng/ml, added on day 6) (Figures S7 and S7P). TAMs were incubated at 37°C, 5% CO_2 for 6 days in a medium composed of TCM (30%) and RPMI (70%) + FBS (10%) + M-CSF (100 ng/ml). Subsequently, TAMs were incubated in hypoxic conditions (1% O_2) for 16–18 h. All the polarized macrophages were detached using StemProAcutase 1X (Gibco) for 10 min at 37°C.

Cytokine array human

hTAMs were lysed by using Lysis Buffer 17 (R&D Systems) supplemented with 10 μg/mL protease inhibitor cocktail. Samples were incubated on ice for 30 min and then centrifuged at 14,000 x g for 5 min at 4°C. The supernatant was then transferred into a clean tube, and protein quantification was performed by using the BCA Protein Assay Kit (Thermo Fisher Scientific). Samples were then stored at -80°C upon subsequent analysis. The antibody array assay was performed using the Proteome Profiler Array Human XL Cytokine Array kit (R&D Systems), which is able to simultaneously detect 105 different analytes, according to the manufacturer's instructions. Briefly, a pool of 3 different hTAM samples was prepared by mixing 67μg of total protein/sample to a final concentration of 200 μg total protein. The pool was incubated with membranes containing immobilized capture antibodies. Following incubation and washing, a cocktail of biotinylated detection antibodies was added, followed by streptavidin-HRP. Chemiluminescent signals were detected using UVITEC and analyzed with ImageJ. The intensity of each spot on the array corresponding to a specific protein was quantified and normalized to internal positive controls on the membrane.

Co-cultures of iPSC-derived MNs and mouse or human M2-like macrophages and TAMs

iPSC-derived MNs were co-cultured adding 15 x 10^3 mouse/human *in vitro*-generated M2-like macrophages (+M2/+hM2), or mouse/human TAMs (+TAM/+hTAM) in each well. After 48 h of co-culture (at 37°C, 5% CO_2), cells were fixed in 4% PFA (Mondial), 4% sucrose, and left in PBS 1X at 4°C for subsequent immunostaining analysis.

Co-cultures of SH-SY5Y and human TAMs

SH-SY5Y neurons were co-cultured 1:1, adding 5 × 10^4 TAMs (+TAM) in each well. After 48 h of culture (37°C, 5% CO_2), cells were fixed in 4% PFA (Mondial), 4% sucrose, and left in PBS 1X at 4°C for subsequent immunostaining analysis.

SPP1 inhibition (Parecoxib) in SH-SY5Y and TAM co-culture

SPP1 inhibitor Parecoxib (163 μM; TargetMol)[123] was added to SH-SY5Y co-cultured with 5 x 10^4 TAM at the beginning of the co-culture (+TAM+Parecoxib). The solvent of Parecoxib, DMSO, was added to control SH-SY5Y (CTRL) and SH-SY5Y co-cultured with 5 x 10^4 TAMs (+TAM). After 2 days, cells were fixed in 4% PFA (Mondial) and 4% sucrose, and then left in PBS 1X at 4°C for subsequent immunostaining analysis.

COX2 inhibition (Celecoxib) in SH-SY5Y and TAM co-culture

COX-2 inhibitor Celecoxib (50 μM, LKT Laboratories) was added to control SH-SY5Y (CTRL) and SH-SY5Y co-cultured at a 1:1 ratio with 5 × 10^4 TAM at the beginning of the co-culture. After 2 days, cells were fixed in 4% PFA (Mondial) and 4% sucrose, and then left in PBS 1X at 4°C for subsequent immunostaining analysis.

SPP1 inhibition (siRNA) in human TAMs and co-culture with SH-SY5Y or iPSC-derived MNs

On polarization day 5, in vitro hTAMs were incubated for 6 h at 37°C with predesigned siRNA against human *SPP1* (Qiagen) or Scramble (Qiagen) and HiPerFect Transfection Reagent. Transfection reagents were washed away with culturing media, and cultures were allowed to recover for 24 h. On polarization day, 7.5 × 10^4 or 15 × 10^3 transduced hTAMs were added to SH-SY5Y or iPSC-derived MNs, respectively, prepared as described above. After 2 days, cells were fixed in 4% PFA (Mondial) and left in PBS 1X at 4°C for subsequent immunostaining analysis.

mTORC2 selective inhibition in iPSC-derived MNs or SH-SY5Y co-cultures

To analyze the involvement of the mTORC2 pathway, mTORC2 selective inhibitor JRAB2011 (10 μM; MedCheExpress)[124] was added to the culture medium of iPSC-derived MNs with DMSO (CTRL) culture, of SH-SY5Y with DMSO (CTRL) culture, of iPSC-derived MNs with DMSO co-cultured with 15 x 10^3 mouse TAMs (+TAM), and of SH-SY5Y with DMSO co-cultured with 5 x 10^4 human TAMs (+TAM), respectively at the beginning of the co-culture. After 2 days, cells were fixed in 4% PFA (Mondial) and 4% sucrose, and then left in PBS 1X at 4°C for subsequent immunostaining analysis.

Oxygen deprivation Caspase 3 activation by immunofluorescence

SH-SY5Y differentiated neurons culturing medium was replaced with DMEM Low glucose medium supplemented with penicillin/streptomycin (1%, Gibco), GlutaMAX Supplement (Gibco Life Technologies), and 1% BSA. 5 x 10^4 human TAMs or M2-like macrophages were seeded, and both monoculture and co-culture were left for 2 h in normoxic condition (baseline control) or transferred to hypoxic condition. After 2 h, the cultures were quickly fixed in 4% PFA, and immunocytochemistry using anti-human β3-tubulin and Caspase3 was performed, followed by DAPI staining. At least 10 of the 20x zoom fluorescence images were taken for each condition, and the numbers of β3-Tubulin-positive cells and Caspase3- and β3-Tubulin-double-positive cells were calculated.

Immunophenotyping

hTAMs (2 x 10^5 cells) were stained with the following antibodies: Anti-human CD14, VioBlue REAfinity (Miltenyi Biotec); Anti-human CD68, APC REAfinity (Miltenyi Biotec); Anti-human CD163, APC-Vio770 REAfinity (Miltenyi Biotec); Anti-human CXCR4, VioBright FITC REAfinity (Miltenyi Biotec); Anti-human HIF-1A, Alexa Fluor 647 (BD Biosciences); Anti-human VEGFA, PE (Abcam); Anti-hOsteopontin, APC (R&D). Mouse TAM (2 x 10^5 cells) were stained with the following antibodies: Anti-mouse CD14, APC (eBioscience); Anti-mouse CD206, Alexa Fluor 647 (BD Biosciences); Anti-HLA-DR, APC-Cy7 (BD Biosciences); Anti-mouse iNOS, FITC (Miltenyi Biotec) according to the manufacturer's instructions. Data were acquired using a MACSQuant10 (Miltenyi Biotec) and analyzed with FlowJo10 software. Mean Fluorescence Intensity (MFI) fold changes to negative controls were calculated for each marker.

Transwell migration assay

Transwell migration assays were performed in 24-well plates using Transwell inserts, as described by Wheeler et al.[125] Briefly, M2 and hTAM cells were seeded in RPMI-1640 medium with 25 ng/mL or 100 ng/mL CXCL12 and incubated at 37°C in 5% CO_2 for 16 h. Cells were fixed with 2% PFA and stained with DAPI (Thermo Fisher Scientific). Migrated cells were viewed with a fluorescence microscope (Nikon Eclipse Ni), imaged with a Nikon DS-2MBWc camera, and the number of DAPI nuclei counted using ImageJ software.

qPCR on human TAMs and monocytes

The probe signal was normalized to an internal reference, and a cycle threshold (Ct) was taken significantly above the background fluorescence ($p \leq 0.01$, Poisson distribution). The Ct value used for subsequent calculation was the average of 2 replicates. The relative expression was calculated using the amount of *Ptprc* transcript as an endogenous reference. Data analysis was performed using the comparative method, as outlined in User Bulletin No. 2 (Applied Biosystems).

In vitro immunofluorescence staining and quantification analysis

Immunofluorescent stainings on mNSCs, iPSC-derived MNs, and single neurons obtained from DRGs were performed as previously described.[47,126] For the immunostaining of hTAMs, 100,000 human monocytes were seeded on glass coverslips and polarized to obtain hTAMs. On day 7 after hypoxia, hTAMs were washed twice in cold PBS and fixed in 4% PFA at room temperature for 10min. Briefly, slides were first incubated in blocking solution and then with primary antibodies. After they were incubated with the appropriate secondary antibodies, washed with PBS 1X, and incubated with the nuclear dye. Slides were then mounted using DABCO. The quantitative analysis was done with the ImageJ software (National Institutes of Health, USA). The following primary antibodies were used for immunofluorescence analysis: anti-β3Tubulin (mouse, 1:400; Promega), anti-Caspase3 (rabbit, Cell Signaling, #9661), anti-CD14 (rabbit, Epigentek), anti-CD68 (rat, 1:200; Invitrogen), and SPP1/OPN APC-conjugated (mouse, R&D Systems). Appropriate secondary antibodies were used: goat anti-mouse AlexaFluor 488 (1:500; Thermo Fisher Scientific), donkey anti-rabbit AlexaFluor 568 (1:500; Thermo Fisher Scientific), donkey anti-rat Alexa-Cy3 (1:1000; Jackson). Immunofluorescent images were acquired with a fluorescence microscope (Nikon Eclipse Ni or Nikon Eclipse Ti), a FluoView FV4000 confocal microscope, or a LEICA SP confocal microscope equipped with 20x and 40x objectives. For each sample, at least 3 fields were analyzed for each glass coverslip, using at least 3 different glass coverslips. In each field, a threshold was selected, and the results were normalized to the number of nuclei in the field considered.

Neurite length analysis

The neurite length per cell was measured using a specific plugin in ImageJ on immunofluorescent images from mNSC, mNSC+TAM, and mNSC+M2 co-cultures stained with b3Tub and acquired with a fluorescence microscope (Nikon Eclipse Ti) equipped with 20x.

Zymography analysis

Briefly, supernatants were collected before and after macrophage conditioning, then centrifuged at 300g and ultracentrifuged at 13000g. The supernatants were stored at -20°C until analysis. The protein content was quantified using the Pierce BCA Protein Assay kit (Thermo Fisher Scientific) and diluted with 5X non-reducing sample buffer to a concentration of 40 μg of protein per sample. Gels were then prepared as follows: 7.5% acrylamide separating gel containing gelatin (4 mg/mL) and a stacking gel. After electrophoresis, the gels were stained with Coomassie Brilliant Blue R250 (Sigma Aldrich) and imaged using a Chemidoc MP Imaging System (Bio-Rad). The images were then quantified using Image Lab software (version 6.0.1; Bio-Rad).

Calcium imaging analysis

To test spontaneous calcium activity, 14-day organoids were assessed with the Fluo-4 Direct Calcium Assay Kit (Invitrogen), as previously described.[46] Briefly, after dye loading, time-lapse live imaging was performed at 1 frame/100 ms for 3 min using epifluorescence microscopy optics (Eclipse Ti, Nikon). The calcium indicator intensity in 15 cells/org/condition was measured using the "Plot Z-axis profile" plugin of ImageJ software (USA National Institutes of Health, USA)

Extracellular flux analysis

Oxygen Consumption Rate (OCR) and Extracellular Acidification Rate (ECAR) were measured in M2 and TAM using a Seahorse XF324 Extracellular Flux Analyzer (Agilent Technologies, Santa Clara, USA). On the day of the assay, cells were seeded at a density of 7×10^4 cells/well in a V7 XFe24-well cell culture microplate coated with poly-D-lysine and then centrifuged at 400g for 2 min to ensure attachment to the bottom of the plate. To measure mitochondrial OXPHOS, cells were incubated in Seahorse XF DMEM medium (Seahorse Bioscience) supplemented with 10 mM glucose, 1 mM sodium pyruvate, and 4 mM L-glutamine, pH 7.4, at 37°C in a non-CO_2 incubator for 1 h. OCR was measured at the baseline and after sequentially adding 1 μM oligomycin A, 1 μM carbonyl cyanide 4-(trifluoromethoxy) phenylhydrazone (FCCP), and 0.5 μM each of rotenone and antimycin A. To measure glycolysis, cells were incubated in Seahorse XF DMEM medium (Seahorse Bioscience) supplemented with 4 mM L-glutamine, pH 7.4, at 37°C in a non-CO_2 incubator for 1 h. ECAR was measured at the baseline and after sequentially adding 10 mM glucose, 1 μM oligomycin A, and 50 mM 2-deoxy-D-glucose. Data were normalized to the DNA content *per* well, which was quantified using the CyQUANT cell proliferation assay kit (Thermo Fisher Scientific), according to the manufacturer's instructions, and analyzed as previously described.[126]

Immune modulatory effect of TAM on M1-like polarized macrophage, and FACS analysis

To investigate the immune modulatory effect of TAMs on M1-like polarized macrophage, primary murine M1-like macrophages from WT animals and td-tomato TAMs from B6.Cg-Gt(ROSA)$^{26Sortm14(CAG-tdTomato)Hze}$/J mice were co-cultured. M1-like macrophages were plated alone or in co-culture with TAMs (1:10 TAM/M1 ratio) in RPMI, 10% FBS, 200 mM L-Glutamine, and P/S for 24 h. Thereafter, macrophages were detached with Accutase for 15 min at 37°C and analyzed by FACS analysis. Briefly, 2 x 10^5 cells were permeabilized for intracellular cell staining according to the Transcription Factor Staining kit (Miltenyi Biotec). Permeabilized cells were stained with 1:100 anti-mouse iNOS FITC (Miltenyi Biotec) for 1 h at RT. tdTomato negative M1-like macrophages were gated, and FITC Median Fluorescence Intensity (MFI) was quantified by MACSQuant10 (Miltenyi Biotec). Data from n=7 independent experiments were collected, and the MFI of M1 with or without TAM co-culture was compared.

Lung tumor metastasis evaluation

For the analysis of spontaneous lung metastasis, the tumor murine model was autopsied 23 days after tumor cells and TAM injection. Lungs were collected in cold PBS and formalin fixed for 24 h, dehydrated, and paraffin-embedded for histologic analysis. Tissue blocks were deparaffinized in xylene and rehydrated through a graded alcohol series. The tissue sections were stained with hematoxylin (Histo-Line) for 10 min and with eosin (Histo-Line) for 7min. Stained slides were dehydrated through a graded alcohol series before mounting with Eukitt (Sigma-Aldrich). Whole–slide digital scans were acquired using a ZEISS Axio Scan Z1 Slide Scanner at ×20 magnification. Histology was performed on longitudinal serial sections (100 μm apart, with a width of 4 μm) from each lung. The area of lung lesions was obtained by manually tracing the perimeter of the lesions using Qu-Path software, which enables the analysis of digitized H&E images.

Cell transplantation

Injured mice were anesthetized, and the injured spinal cord parenchyma was exposed. *In vitro* generated TAMs, M2-like macrophages, and TAM^{LVScramble}- or TAM$^{LV\ Spp1\text{-}KD}$ were transplanted in scSCI mice. Each animal received 4 injections (1 μl/injection) of cell suspension (TAM-, M2-, TAM^{LVScramble}- or TAM$^{LV\ Spp1\text{-}KD}$, 0.5 x 10^6 cells/μl), saline solution, or recombinant SPP1 (rSPP1) (3 ng/μl) in 4 points separated each other by 2 mm (0.5 mm depth) close to the lesion hematoma. Experimental animals treated with TAM+Batimastat received, with the same procedure, 4 injections (2 μl/injection) of a cell suspension composed of 0.5×10^6 cells/μl added to Batimastat (5 μM). For the preclinical long-term assessment healthy mice underwent a laminectomy at T11 vertebra level and received 4 injections (1 μl/injection) of cell suspension (TAM-, M2-, 0.5 x 10^6 cells/μl), or saline solution in 4 points separated each other by 2 mm (0.5 mm depth) centred on the spinal segment under the removed T11 vertebra. All the animals received single (4 days post injury, dpi) or multiple (3, 10, and 17 dpi, or 3, 10, 17, and 24 dpi, or 10, 17, and 24 dpi) transplantations of TAM, M2, TAM^{LVScramble}, or TAM$^{LV\ Spp1\text{-}KD}$, rSPP1, TAM+Batimastat, or vehicle. Subcutaneous injections of Baytril (10 mg/Kg) and Altadol (2 mg/Kg) were provided on the day of the surgery and for the first 2 days post-transplantation (dpt).

Locomotor evaluation and ankle joint flexibility analysis

The locomotor function of vehicle-, TAM-, M2-, Rictor^{KD} +TAM-, Rictor^{Scr} +TAM-, TAM^{LVScramble}-, TAM$^{LV\ Spp1\text{-}KD}$, rSPP1- and TAM+Batimastat-treated mice was evaluated by using the Basso Bettie and Bresnahan (BBB) score adapted to mice Basso Mause Scale (BMS)[71] using a modified open-field BBB scale (scoring from 0 to 21). The locomotor functionality of vehicle-, TAM-, M2-, Rictor^{KD} +TAM-, Rictor^{Scr} +TAM-, TAM^{LVScramble}-, TAM$^{LV\ Spp1\text{-}KD}$-, rSPP1- and TAM+Batimastat- treated mice was also evaluated with BMS, a 9-point scale.[70] All behavioral assessments, histological quantifications, and data analyses were performed by investigators blinded to the treatment groups. For functional analyses, the day after the scSCI (1 day post injury, 1 dpi), each animal

was assessed with BMS, BBB score by at least 2 observers. The criteria for enrolment were based on the BMS, BBB score measured at 1 dpi. Specifically, individuals with a BMS/BBB score of 0.5 (BMS) or 1 (BBB) or less at 1 dpi were included in the study. On the day of transplantation, before the surgery, animals eligible for the study were randomly allocated into experimental groups, ensuring a comparable distribution of BMS, BBB mean values between the groups. The locomotor performance was monitored from 4 min in an open field at 1, 3, 4, 5, 7, 10, 11, 14, 17, 18, 21, 23, 24, 25, 28, 31, 32, 35, 36, and 37 dpi. Animals included in VEH- and TAM- long-term groups were evaluated at 1, 3, 4, 5, 7, 10, 14, 17, 21, 24, 28, 31, 45, 49, and 56 dpi.

To evaluate the spasticity of the muscles involved in ankle dorsiflexion and plantar flexion, ankle joint flexibility analysis was performed from 14 dpi, as previously described.[64] The following scores were assigned: "0" to the lack of passive flexure (spastic condition) corresponding to an angle of 180° between the tibia and the foot, "0.25" to an angle of 135°, "0.5" to an angle of 90°, "0.75" to an angle of 45°, and "1" (complete passive flexure) corresponding to an angle of 0°. For statistical analysis of the BBB, the BMS, and the AJF score, the mean of the left and right hindlimb scores was taken to yield a single BBB, BMS, and AJF score per mouse at each time point.

In vivo electromyographic recording

In vivo electromyographic (EMG) recording of spontaneous muscle activity was performed in the *Tibialis Anterior* (TA) and *Lateral Gastrocnemius* (LG) muscles. The foot extensor and flexor muscles are antagonists to each other and are innervated by motor neurons whose cell bodies are caudal to the level of scSCI.[127] Severe injury to animals displayed a distinctive EMG pattern, characterized by a lower amplitude and longer periods of activity compared to healthy mice. In each muscle of anesthetized animals, we inserted thin stainless-steel wires with bare tips and connected them to the amplifier (CyberAmp 320, Axon Instruments). As a reference electrode, a cut-short 20G stainless steel needle was inserted under the skin in the back of the animals and connected to ground. The recording began 10 min after full recovery from anesthesia, and lasted 3 min for each muscle, during which time the animal was gently stimulated to move every 10–15s. We estimated the amount of muscle paralysis by averaging the root mean square (RMS) values of the 10 largest EMG signals. Spasticity was estimated by calculating the duration of muscle activity relative to the total recording duration. In total, we recorded 31 TA muscles from 17 mice and 29 LG muscles from 16 mice.

Corticospinal Tract Tracing in scSCI mouse model

3 days before the scSCI surgery, vehicle- and TAM-treated mice received tracer injections into the motor cortex areas. Mice were anesthetized and positioned in a digital stereotaxic apparatus (RWD Life Science) with the head held in place by ear bars. The scalp was retracted, and a hole was drilled above the motor cortex. After the brain parenchyma exposure, using the digital stereotactic apparatus 1 μl of 2 mg/ml biotinylated dextran amine (BDA; MW 10,000; Molecular Probes) in PBS was injected at 6 specific coordinates (3 sites/side) using a 10 μl Hamilton microsyringe. Mediolateral (ML) coordinates: ±1 mm lateral to Bregma; anteroposterior (AP) coordinates from Bregma: 0, ±0.5 mm; dorsoventral (DV) coordinates from the cortical surface: 0.7 mm. The microsyringe was left in place for 1 min after the injection to allow tracer diffusion. The scalp was then sutured, and mice were allowed to recover. Subcutaneous injections of Baytril (10 mg/Kg) and Altadol (2 mg/Kg) were provided on the day of the surgery and for the first 3 days post-injection.

mTORC2 selective inhibition in scSCI mouse model

The day of TAM transplantation (3, 10, and 17 dpi), with a 10 μl Hamilton microsyringe connected to a digital stereotaxic apparatus (RWB Life Science), 4.8 x 10^{10} genome copies of custom-made recombinant AAV9-GFP-U6-mRICTOR-shRNA ($Rictor^{KD}$ mice) (Biolabs, Malvern) or AAV9-GFP-U6-scramble-shRNA ($Rictor^{Scr}$ mice) (Biolabs, Malvern) were injected (0.5 μl/injection) in 6 points of the exposed spinal cord parenchyma of injured mice. Injections were separated from each other by 0.5 mm (0.5 mm depth), interspersed with the points of TAM transplantation.

Tissue fixation and processing

Animals were intracardially perfused with 4% paraformaldehyde (PFA) and 4% sucrose. Spinal cords were extracted, incubated overnight in 4% PFA, 4% sucrose, and stored in 30% sucrose at 4°C. For histochemical analysis, 1.5 cm of dissected spinal cords (0.75 cm rostral and 0.75 cm caudal from the site of the lesion) were cryosectioned (25 μm-thick sections, for BDA imaging 80 μm-thick longitudinal sections) and stored at −20°C before analysis.

Ex vivo immunofluorescence, histochemical staining, and quantification analysis

The staining for BDA was performed using the Alexa Fluor™ 488 Tyramide SuperBoost™ Kit (Invitrogen). Immunofluorescent and histochemical staining of TAM-, M2-, and vehicle- spinal cord transversal and longitudinal sections were performed as previously described.[64] The same protocol was used to perform immunofluorescent stainings on MN/MCA1, MN/MCA1+TAM, MN/MCA1+$TAM^{LVScramble,}$ and MN/MCA1+$TAM^{LVSpp1\text{-}KD}$ tumor samples. Briefly, for immunofluorescent stainings, slides were first incubated in blocking solution and then with primary antibodies. After they were incubated with the appropriate secondary antibodies, washed with PBS 1X, and incubated with the nuclear dye. Slides were then mounted using DABCO for fluorescent/confocal microscopy. The following primary antibodies were used for immunofluorescence analysis: anti-CD31 (platelet endothelial cell adhesion molecule, PECAM-1, rat, 1:200; BD Biosciences), anti-CD68 (rat, 1:200; Thermo Fisher Scientific), anti-CD163 (mouse; 1:100; Genetex), anti-CD206 (goat, 1:400; R&D Systems), anti-Choline acetyltransferase (ChAT, goat, 1:200; Millipore), anti-Collagen-I (Coll1,

rabbit, 1.200; Abcam), anti-Collagen-III (Coll3, mouse, 1.200), anti-Fibronectin (rabbit, 1:200; Dako), anti-GFP (rabbit, 1:400; Thermo Fisher Scientific), anti-Glial fibrillary acidic protein (GFAP, goat, 1:200; Abcam), anti-Ionized-calcium binding adapter molecule-1 (Iba1, rabbit, 1:200; WAKO), anti-NEUN (mouse, 1:200; Millipore), anti-Neurofilament-200 (rabbit, 1:200; Sigma), anti-Peripherin (rabbit, 1:200; Millipore), anti-RFP biotinylated antibody (rabbit, 1:200; Rockland), anti-VGLUT1 (rabbit, 1:400, Synaptic system), anti iNOS (1:200, FITC REAfinity Myltenyi Biotec). Appropriate secondary antibodies were used: donkey anti-goat AlexaFluor 488 (1:500; Jackson), donkey anti-goat AlexaFluor 647 (1:500; Thermo Fisher Scientific), donkey anti-mouse AlexaFluor 488 (1:500; Thermo Fisher Scientific), donkey anti-mouse AlexaFluor 647 (1:500; Thermo Fisher Scientific), donkey anti-rabbit AlexaFluor 488 (1:500; Thermo Fisher Scientific), donkey anti-rabbit AlexaFluor 647 (1:500; Thermo Fisher Scientific), donkey anti-rat AlexaFluor 488 (1:500; Thermo Fisher Scientific), TO-PRO-3 (1:3000; Thermo Fisher Scientific) or DAPI (1:2000; Thermo Fisher Scientific). For histochemical RFP and NF200 staining, sections were briefly incubated in blocking solution after endogenous peroxidase neutralization, followed by incubation with the anti-RFP or anti-NF200 antibody. After washing steps, slices were incubated with the appropriate secondary biotinylated antibody. Tissue sections were visualized using VectaStain ABC kit (Vector Laboratories, Rome, Italy) and developed in DAB (3,3-diaminobenzidine) peroxidase substrate (Sigma-Aldrich, Milan, Italy). Sections were then washed with H_2O and stained with hematoxilin, dehydrated and mounted with Entellan (Merck Millipore) for light microscopy. For LFB staining, sections were briefly hydrated in EtOH solutions, incubated with 0.1% LFB solution (Sigma Aldrich), differentiated in Li2CO3 solution (Sigma Aldrich), and then dehydrated in EtOH solutions, cleared in xylene (Carlo Erba), and mounted with Entellan (Merck Millipore) for light microscopy.

Luxol Fast Blue (LFB) staining

Myelin content was assessed via LFB staining as previously described by Dolci and colleagues.[128] Briefly, 25 μm-thick spinal cord transverse sections from VEH-, TAM-, M2-, $TAM^{LVScramble}$-, and $TAM^{LV\ Spp1\ KD}$-treated scSCI animals were rinsed in PBS 1X. 0.1% LFB solution was prepared by solubilizing LFB (Sigma–Aldrich) in 95% ethanol (EtOH, Carlo Erba) and 1.22% glacial acetic acid (Carlo Erba). Sections were hydrated in EtOH solutions (100%, 95%, 70%, and 50%) and then stained with a 0.1% LFB solution at 40°C for 40 min. Sections were then rinsed with tap water and differentiated in 0.05% Li2CO3 solution (Sigma–Aldrich). Sections were then dehydrated in EtOH solutions (50%, 70%, 95%, and 100%), cleared in xylene (Carlo Erba), and mounted with Entellan (Merck-Millipore) for light microscopy analysis of myelin content (Zeiss Axioscop 2).

Image analysis and quantification

The quantitative analysis was done with the ImageJ software (National Institutes of Health, USA). Immunofluorescent images were acquired with a fluorescence microscope (Nikon Eclipse Ni, Nikon Eclipse Ti), a FluoView FV4000 confocal microscope, or a LEICA SP confocal microscope equipped with 20x and 40x objectives. Image quantification: n is defined as number of biological independent samples, and is indicated in the figure legend for each experiment; for each biological replicate at least 2 technical replicates we analysed, yielding the following number of samples: *Tumor samples*: i) the absolute number of nerves was counted manually across entire tumor sections, in at least 8 section per sample, ii) NF200 content was assessed in at least 5 fields (2658.10 μm x 2292.43 μm) across a minimum of 8 sections (large image) for each tumor sample. In each field, a threshold was applied, and results were normalized to the field area. *Spinal cords*: i) The content of NEUN, IBA1, CD68, CD163, CD206, VGLUT1, CHAT and CD31 was evaluated in at least 8 transverse spinal cord sections per biological replicate; ii) NF200 content was assessed in at least 8 longitudinal spinal cord sections per biological replicate, within an area defined by 4500 μm-wide rectangle centered on the cyst; the occurance of tdTomato TAMs close to $NF200^+$ fibers was assessed in at least 20 images per biological replicate, within an area defined by 300 μm-wide square randomly cropped from longitudinal spinal cord slices stained with NF200, iv) Coll1, Coll3 and fibronectin content were evaluated in at least 3 spinal cord sections per biological replicate; v) Luxol Fast Blue (LFB) staining was quantified in at least 14 spinal cord per biological replicate, vi) BDA analysis was performed on at least 6 longitudinal spinal cord sections per biological replicate, within a 2200 μm-wide rectangle centered on the cyst. The number of positive pixels in the selected region containing BDA-labeled axons caudal to the injury was quantified to assess axonal regeneration. Specifically, axonal density (BDA^+ pixels) was calculated based on pixel intensity measurements taken at a fixed distance (2.5 mm) caudal to the lesion epicenter. This value was then normalized to the pixel intensity measured at the same distance rostral to the lesion epicenter (2.5 mm). The total number of positive cells, tdTomato TAM close to $NF200^+$ fibers, or puncta was quantified either *in silico* (NEUN, IBA1, CD68, CD206, VGLUT1) or manually ($CD68^+CD163^+$, CHAT, tdTomato TAM close to $NF200^+$ fibers), or by applying a threshold (CD31, NF200, Coll1, Coll3, Fibronectin, Luxol, and BDA). Results were normalized according to: - the total number of nuclei in the spinal cord slice (approximately 5414 ± 44 nuclei/slice) for NEUN, IBA1, CD68, CD206, CHAT, the total number of $CD68^+$ cells in the spinal cord slice ($CD68^+CD163^+$), - the total number of tdTomato TAM in the spinal cord area within a 300 μm-wide squares for tdTomato TAM close to $NF200^+$ fibers, - the total area of the spinal cord slice for VGLUT1, CD31, Coll1, Coll3 and Fibronectin, - the spinal cord area within a 4500 μm-wide rectangle centered at the cyst for NF200, - the dorsal columns region of the spinal cord slice for LFB staining, - 2200 μm-wide rectangle centered at the cyst, encompassing both rostral and caudal regions of the spinal cord slice for BDA. Cyst area was quantified on 735 transverse images obtained by X-ray tomography, spanning approximately +0.35 cm rostral to −0.35 cm caudal relative to the lesion epicenter. Cyst volume was estimated for each animal by analyzing all spinal cord sections containing a cyst, calculating the ratio of the cyst area to the total slice area, and multiplying by the section thickness. Quantitative analysis was performed: Tumor samples: i) on serial transverse histological sections spanning approximately +0.2 cm rostral to −0.2 cm caudal relative to tumor epicenter. Spinal cords: i) on serial transversal histological sections spanning approximately +0.35 cm rostral to −0.35 cm caudal

to the lesion epicenter for the analysis of NEUN, IBA1, CD68, CD163, CD206, VGLUT1, CHAT, CD31, NF200, Coll1, Coll3, Fibronectin and Luxol; ii) on serial longitudinal histological sections spanning the entire spinal cord for the analysis of NF200, tdTomato TAM close to NF200$^+$ fibers and BDA. Morphometric blood vessels analysis was performed using NIH ImageJ software on vehicle- and TAM-treated spinal cord fields (4 fields/animals) from transversal sections stained with the CD31 marker. 3 to 6 mice were considered for the analysis; the exact number of mice is reported in each graph.

Analysis of tissue oxygenation

Tissue oxygenation analysis was performed, evaluating the oxidized thiols accordingly to Lange and colleagues.[129] Briefly, mice were transcardially perfused with 1.85% Iodoacetamide (IAA) and 1.25% N-ethyl maleimide (NEM) and then fixed with a 4% PFA (Mondial, cat. #FM0622), additionally with 1.85% IAA and 1.25% NEM. Spinal cords were dissected, and, after transversal cryosectioning, disulfides were reduced with 4 mM Tris (2-carboxyethyl) phosphine hydrochloride (TCEP; Sigma Aldrich) in PBS for 1 h. Those reduced thiols were then labeled with 7-diethylamino-3-(4'-maleimidylphenyl)-4-methylcoumarin (CPM; Sigma Aldrich) for 30 min. Samples were then washed and mounted with DABCO. The slice area was delineated with a region of interest (ROI), and the hypoxic areas were quantified using ImageJ software (National Institutes of Health, USA) as a percentage of positive pixels within the ROI, normalized to the total pixels of the ROI. For each independent biological sample, at least 11 entire spinal cord sections were analyzed.

tdTomato M2-like macrophage, TAM distribution analysis

The tdTomato M2/TAM distribution analysis was performed on M2-, TAM-treated mice, which received multiple transplantations at 3, 10, and 17 days post injury (dpi). Slices were stained with the nuclear marker DAPI (1:2000; Thermo Fisher Scientific), and the number of tdTomato M2$^+$/DAPI$^+$ cells or TAM$^+$/DAPI$^+$ cells in the lesion section was manually counted with the CellCounter plugin in NIH ImageJ software (National Institutes of Health, USA). At least 5 transversal injured spinal cord sections of M2- or TAM-treated mice were analyzed in technical replicates (glass slides) on at least 4 animals.

Ex vivo optical imaging

Fluorescent images were acquired using an IVIS Spectrum optical imager (PerkinElmer), equipped with a cooled (-90°C) back-thinned and a back-illuminated CCD camera. Images calibrated in radiance units (p/s/cm2/sr) were corrected for dark measurements and cosmic rays. The total flux (p/s) was measured by drawing a region of interest (ROI) over the images. Image acquisition, processing, and analysis were performed with Living Image 4.5 (Perkin Elmer). Extracted organs (heart, lungs, pancreas, spleen, stomach, kidney, testes, bladder, skin, lymph nodes, brain, liver, gut, spinal cord) were imaged with the following image parameters: excitation filter = 535 nm, emission filter = 680 nm, automatic exposure time, aperture stop f = 2, binning B = 8 with a Field of View (FoV)=6.6 cm-13.0 cm. The line intensity profile (3-pixel width) of the fluorescent emission along the spinal cord was measured on the fluorescent images.

X-ray phase-contrast micro computed tomography

X-ray phase-contrast imaging was performed at the I13-2 beamline of the Diamond Light Source synchrotron radiation facility. 3D representations of unstained spinal cord samples were obtained through in-line phase-contrast projection imaging and by using a single defocused-image phase retrieval algorithm.[130] The volumetric reconstructions were performed using the dedicated micro computed tomography processing pipeline available at the beamline.[80–83] The cyst areas were manually segmented from the main volumes for subsequent analysis using a custom-designed plugin of ImageJ software (National Institutes of Health, USA).

Immunoblot analysis

Immunoblot analysis was performed as previously described.[64] Briefly, spinal cord samples were homogenized in radioimmunoprecipitation assay (RIPA) buffer containing protease and phosphatase inhibitors. After blocking, membranes were probed with the appropriate primary antibodies overnight and then incubated with the corresponding horseradish peroxidase-conjugated secondary antibodies. ECL-based signals (Clarity Western ECL Substrate; Bio-Rad Laboratories) were acquired with the Chemidoc MP imaging system (Bio-Rad Laboratories), normalized on total protein staining, and analyzed with the Image Lab Software (version 6.0.1; Bio-Rad).

Quantitative Real-Time PCR

Total RNA was extracted from a fresh cell pellet using the Genejet RNA purification kit (Thermo Fisher Scientific). cDNA was synthesized from 1 μg of total RNA using SuperScript reverse transcriptase (Thermo Fisher Scientific). Quantitative real-time PCR (RT-PCR) was carried out using TaqMan Universal PCR Master Mix on QuantStudio 5 RealTime instrument, and the relative amount of mRNA for *PTPRC*, *CD14*, *CD206*, *CXCR4*, *GLUT1*, *MT2A*, *MT1X*, *ANGPTL4* and *SPP1* genes (Hs04189704_m1, Hs02621496_s1, Hs07288635_g1, Hs00607978_s1, Hs00892681_m1, Hs02379661_g1, HS00745167_s1, HS01101123_g1; Hs04189704_m1, Hs00959010_m1, Applied Biosystem) was calculated as fold increase on *PTPRC* expression (internal control). Data were obtained using the $\Delta\Delta^{-Ct}$ method.

Proteomic analysis

Protein from spinal cord samples of 6 vehicle-, 7 TAM-, and 7 M2-treated mice were extracted in lysis buffer (150 mM NaCl, 1% Triton X-100, 50 mM Tris HCl pH 7.4, 0.5% sodium deoxycholate, and 0.1% sodium dodecyl sulfate in ddH2O supplemented with complete Roche protease inhibitor)[131] and their concentrations in the obtained supernatants, were determined using the DC Protein Assay (Bio-Rad Laboratories) according to the manufacturer's instructions. Briefly, a paramagnetic bead approach was applied,[132,133] during which proteins were reduced with TCEP and alkylated with IAA, followed by a protein clean-up. Afterward, proteins were enzymatically cleaved using trypsin (1:50), and a peptide clean-up was performed using ACN. Finally, the peptides were eluted in two steps: first with 87% ACN in 10 mM ammonium formate (pH 10) and then with 2% DMSO (dimethyl sulfoxide) in water. Thus, two fractions of peptides were obtained, which were subsequently analyzed using a Q Exactive HF mass spectrometer (MS; Thermo Fisher Scientific), which was coupled to a liquid chromatography (LC, UltiMate 3000 RSLC nano system; Dionex) via a chip-based electrospray ionization source (TriVersa NanoMate; Advion) as described before.[134]

Preclinical safety assessment (histopathology)

Twenty-two mice, 12 VEH-treated and 10 TAM-treated, subjected only to laminectomy, were examined 1 year after treatment. A complete necropsy was performed, and the following organs were collected for histopathological examination: spinal cord, brain, heart, lungs, liver with gallbladder, kidneys, spleen, pancreas, intestine, and bone marrow (including the vertebral bodies). Organs/tissues with grossly detectable lesions were also sampled. Samples were fixed in 10% neutral buffered formalin and routinely processed for paraffin embedding. 4μm-thick sections were stained with hematoxylin-eosin and evaluated under a light microscope. A pathologist blinded to treatment groups performed the assessments.

QUANTIFICATION AND STATISTICAL ANALYSIS

To calculate the number of animals needed for each experiment, we based our approach on the F-test of a repeated measures ANOVA with 1 between-subject factor (treatment, with 3 groups) and 1 within-subject factor (time, with 17 measurements). The primary objective of this experiment is to study the interaction between these two factors. The effect size was set at f = 0.25, the type I error rate at 5%, the power at 80%, and the correlation between measurements at 0.5. Under these conditions, the minimum required sample size is 5 animals per group.

The effect of TAM multiple transplantation on locomotor functionality (BBB, BMS) was estimated using a mixed-effects regression model. Fixed effects included time (dpi) and treatment, while mouse ID was treated as a random effect. The nonlinear relationship between BBB, BMS and time was modelled using a linear spline with one knot within each treatment group. A time-by-treatment interaction term was also included in the model. AJF was modelled by a linear mixed-effect model without splines. Fixed effects were time (dpi) and treatment; mice ID was the random effect. A time x treatment interaction term was also considered. In the two models, the significance of the interaction term was tested by comparing the models with and without the interaction term using a (one-tailed) F-test, with the F-statistic calculated based on the Kenward-Roger method. The only covariates considered in the analysis are treatment and time.

Each measurement was taken from at least 3 distinct biological samples; technical replicates for each distinct biological sample are indicated in the relevant STAR Methods section. The number of distinct biological samples used in each experiment is indicated in the figure or figure legends. Statistical tests were performed using GraphPad Prism software (GraphPad) or R software. These tests included the unpaired 2-sided Student's t-test and the F-test for both 1-way ANOVA and 2-way ANOVA with repeated measures, followed by the (two-tailed) Tukey's post-hoc test. We quantified the differences between the mean BBB values in the 3 groups by using the ratio of means as a measure of effect size.[135] Data are presented as mean ± SEM. Statistical p values are indicated as exact values whenever suitable, or it is indicated by asterisks: *$p < 0.05$; **$p < 0.01$; ***$p < 0.001$; ****$p < 0.0001$ in the figures.

ADDITIONAL RESOURCES

Reviewer access to Glioblastoma scRNA is available at https://www.ebi.ac.uk/biostudies/studies/S-BSST1498?key=fd621f15-1d80-4525-b401-2832ec34e8b6; Reviewer access to bulk RNA-Seq of mouse *in vitro*-generated M2 and TAM is available at https://www.ebi.ac.uk/biostudies/studies/S-BSST1497?key=48d73fa1-5d86-49a7-b4e5-f52e2df5c8d3; Reviewer access to bulk RNA-Seq of human *in vitro*-generated M2 and TAM is available at https://www.ebi.ac.uk/biostudies/studies/S-BSST1502. The proteomics raw data have been deposited to the ProteomeXchange Consortium via the PRIDE[107] partner repository https://www.ebi.ac.uk/pride/login with the dataset identifier ID: PXD038064, Username: reviewer_pxd038064@ebi.ac.uk, password: 8LrstclV.